# A NUMERICAL STUDY OF WATER ENTRY PROBLEMS BASED ON OVERSET MESHES

by

YANNI CHANG

Presented to the Faculty of the Graduate School of
The University of Texas at Arlington in Partial Fulfillment
of the Requirements
for the Degree of

DOCTOR OF PHILOSOPHY

THE UNIVERSITY OF TEXAS AT ARLINGTON

December 2021

To my family.

ACKNOWLEDGEMENTS

First and foremost I would like to thank my esteemed supervising professor Dr. Albert Y. Tong for constantly motivating and encouraging me, and also for his invaluable guidance in both academics and life during the course of my doctoral studies. He guided and inspired me to find and pursue my own ideas, which made the research life enjoyable and rewarding for me. I also thank him for his continuous support and countless help on discussing my research and writing research papers. I am very grateful to him for helping me overcome obstacles and improve myself in different aspects.

I would also like to thank my committee members Dr. Zhenxue Han, Dr. Chaoqun Liu, Dr. Dora E. Musielak, Dr. Liwei Zhang for their thoughtful comments and suggestions on my research work. I would also like to extend my appreciation to the high performance computing facilities at University of Texas at Arlington (UTA) and Texas Advanced Computing Center (TACC) where I have run most of my simulations.

I am also grateful to my teammates and my friends for their kind help and support that have made my study and life at UTA a wonderful time.

Finally, I would like to express my deep gratitude to my family for their encouragement, support, and care.

December 13, 2021

ABSTRACT

A NUMERICAL STUDY OF WATER ENTRY PROBLEMS BASED ON OVERSET MESHES

YANNI CHANG, Ph.D.

The University of Texas at Arlington, 2021

Supervising Professor: Dr. Albert Y. Tong

A series of numerical experiments carried out on the water entry of circular cylinders are presented in this study. A cylinder was entering into the water with a prescribed inclined angle and velocity. The interface between water and air is tracked by the Piecewise Linear Interface Calculation (PLIC) schemes in conjunction with the Volume of Fluid (VOF) method. PLIC schemes have been extensively employed in the VOF method for interface capturing in numerical simulations of multiphase flows. Dynamic overset meshes, which have been widely used for problems with relative motions and complex geometric shapes, are applied to handle the moving cylinder. The numerical model is built on the framework of OpenFOAM which is an open-source C++ toolbox. The results of the numerical model, such as the transient positions and inclined angles of the moving circular cylinder, have been validated with experimental data in the literature. The fluid physics of the oblique water entry problem has been examined. The formation and development of the air entrapment have been explored. Parametric studies on the hydrodynamics of the water entry problem have been performed. It has been revealed that the head geometry, entry impact velocity,

entry inclined angle, liquid density, and object density are of considerable significance for the penetration depth and inclination of the diving cylinder. Surface wetness which affects the detachment of the air channel has also been studied.

A difficulty of the overset mesh implantation in the PLIC-VOF method is the interpolation of the VOF field. Most of the overset interpolation schemes are designed for continuous flow variables. The acceptor value is evaluated by using a weighted average of the ones of its donors. The weighting factors are obtained by different algebraic methods, such as the `averageValue`, `injection`, and `inverseDistance` schemes. Unlike the continuous flow variables, the VOF field is a step function near the interfaces, which varies from zero to unity rapidly. Thus a specialized overset interpolation scheme is needed for the PLIC-VOF method to transfer the fraction field between the meshes precisely. A geometric interpolation scheme of the VOF field in overset meshes for the PLIC-VOF method has also been proposed in this thesis. The VOF value of an acceptor cell is evaluated geometrically with the reconstructed interfaces from the corresponding donor elements. Test cases of advecting liquid columns of different shapes inside a unit square/cube with a prescribed rotational velocity field have been performed to demonstrate the accuracy of the proposed overset interpolation scheme by comparing it with three algebraic ones. The proposed scheme has been shown to yield higher accuracy.

TABLE OF CONTENTS

LIST OF ILLUSTRATIONS

LIST OF TABLES

# CHAPTER 1

# INTRODUCTION

## 1.1 Motivation

The water entry scenario is widely observed at various fields, such as the ship manufacturing, ocean engineering and naval industry. It is the process that a solid rigid object enters a quiescent water surface and the subsequent trajectories of the moving object induced by the hydrodynamics during the diving process.

In an early study one century ago, Worthington and Cole [1] used high speed photography to capture the evolution of the flow after a solid sphere entered the liquid vertically. After their work, numerous experimental studies have been carried out to investigate the impact forces, pressure changes and cavity. An overview of the early work on water entry problems presented by Korobkin and Pukhnachov [2] includes several significant work on the physics of the hydrodynamics in various applications. May and Woodhull [3, 4] who used the position-time data obtained from high-speed images and force balance equations to obtain force components for steel spheres were among the first to study the symmetric water entry problem. Later, Garabedian [5] analyzed the phenomenon of water entry of self-similar wedges mathematically. Faltinsen [6] presented the slamming analysis by applying a 2D theoretical model on ship sections and symmetrical bodies. Besides spheres and self-similar wedges, experimental investigations on various geometries of water entry problems have been performed as well. Glaseen and McMahon [7] studied vertical water entry of disks at low Froude numbers. Bodily [8] investigated experimentally on the forces,

trajectories and acoustics of slender axisymmetric projectiles with cone, ogive and flat noses with different surface conditions.

Experimental studies of water entry with simple motions such as disks entering the water vertically have been performed [7, 9]. More complicated flow patterns and hydrodynamics may be induced by water entry objects with multi-degree-of-freedom motions (running basilisk lizards [10], skipping stones [11] and oblique water entry objects [12]). Truscott and Techet [13] investigated the effects of spin on the trajectory of a sphere entering the water. They obtained the velocity and acceleration through high-speed photos. They also evaluated hydrodynamic forces for spinning hydrophobic and hydrophilic spheres based on a force balance model. Dupeux *et al.* [14] later found that a sphere with sufficient spin can eject from the water surface.

Recently, Wei and Hu [15] studied the water entry phenomena of horizontal circular cylinders at low Froude numbers with the focus on the effects of inclined angle, density ratio and length-to-diameter ratio of cylinders. The lift and drag forces were estimated by using the cylinder motions data with a force model due to the difficulty of measuring forces exerted on the moving object directly from the experiment. Oblique water entry scenario is more practical since objects do not always penetrate into water vertically. Xia *et al.* [16] conducted experiments of cylinders with various inclinations for the water entry situation. Transient trajectories and angular inclinations of the cylinder at low speed have been obtained by a high-speed camera. Asymmetric impact cavities and double cavities were observed following the penetrating process which showed different flow characteristics with single-degree-of-freedom objects. Gilbarg and Anderson [17] studied impact cavities with speeds of spheres and cylinders at tens of m/s. Furthermore, Shi *et al.* [18] investigated the cavity and splashes with high speed objects (hundreds of m/s). Shock waves and opaque cavities were observed in the turbulent flows [19]. Moradi *et al.* [20]

applied a hydroelastic hybrid model to simulate the fluid-structure interaction in the water entry of a flat plate using the partitioned approach. An extended Wagner's model in conjunction with the hydroelastic model was employed to overcome the instability associated with the fluid added mass. Shams *et al.* [21] applied a semi-analytical model to investigate the entire hydroelastic slamming of the wedge from the entry to exit phase. The potential flow theory was employed to estimate the hydrodynamic loading and the Euler-Bernoulli beam theory was used to model the structural dynamics. The particle image velocimetry (PIV) was applied to estimate the velocity field, and the pressure field was obtained by solving the incompressible Naiver-Stokes equations from PIV data.

Direct measurements of impact forces, velocity fields, pressure distribution, lift and drag forces exerted on projectiles are difficult. With the development of the computational fluid dynamics (CFD), more numerical methods have been employed to simulate the water entry problem. The main difficulty in the numerical simulation is the presence of the free surface. The volume of fluid (VOF) method [22, 23, 24], the level set method [25] and the marker and cell method (MAC) [26] are commonly used to track the free surface. Shi *et al.* [27] applied a radial basis function based ghost cell method (RBFGCM) to deal with the arbitrary moving body on a fixed Cartesian grid. A gradient-augmented level set (GALS) method was employed to capture the interface. Yu *et al.* [28] studied the water entry process of curved wedges using an Arbitrary Lagrange-Euler (ALE) algorithm. Sun *et al.* [29] investigated the slamming load of the water entry process. The coupled Euler-Lagrange method was applied in the numerical model in which the flow boundary lay effect was not considered in their study. Oger *et al.* [30] applied smoothed particles hydrodynamics (SPH) method based on mesh-free numerical techniques to study the water entry problem of two-dimensional wedges. Yang and Qiu [31] applied Cubic interpolated pseudo-particle

method (CIP) method to compute slamming forces on both 2D and 3D bodies with constant entry velocities. A combined Lagrangian-Eulerian method was employed to model boundaries of the solid body, and CIP method was applied to capture the free surface.

The Volume of Fluid (VOF) method [22, 32] is widely used to capture the interface in multiphase flows. It introduces a scalar variable called the VOF function $F$ which is defined as the liquid volume fraction in a computational cell with the value of zero for gas phase, unity for liquid phase, and between zero and one for mixed (interface) cells, respectively. Both algebraic and geometric methods have been applied to solve the VOF equation. The algebraic method lacks accuracy on the normal and curvature calculations due to discontinuity of the VOF function at the interface, which leads to numerical diffusion resulting in convergence problem [33]. In the present study, the Piecewise Linear Interface Calculation (PLIC) schemes in conjunction with the VOF method have been employed to track the interface.

In the reconstruction step, the interface location within a mixed cell is determined by the predefined geometric shape of the interface and volume fraction value $F$. Several approaches have been proposed for the interface reconstruction both in structured [34, 35, 36, 37, 38, 39, 40] and unstructured meshes [41, 42, 43] and the most widely used one is the Piecewise Linear Interface Construction (PLIC) method [41]. In the PLIC method, the interface is approximated by an oriented plane $\vec{n}\cdot\vec{X}+D_0 = 0$, where $\vec{n}$ is the unit outward normal vector of the interface and $D_0$ the signed distance from the origin. In the present study, the orientation vector $\vec{n}$ and signed distance $D_0$ are evaluated by employing the normalized VOF function gradient and the analytical interface reconstruction methods presented in [44, 45], respectively.

The use of stationary meshes is confined to static parts in the computational domain. Also, a common difficulty in simulations is that some geometries cannot be

well-represented by using a single mesh [46]. Representing the distinct geometries by disconnected mesh parts is a better choice in many cases. It is also complicated and time-consuming to prepare a single stationary mesh with complex geometries. The dynamic overset mesh can be especially useful in applications involving components with relative motion [47]. The overset mesh can reduce the computation time compared with applying a deforming mesh method alone [48] and improve the simulation accuracy.

The present study is motivated by the work of Xia *et al.* [16]. In order to handle the relative motion of the free released cylinder, the overset mesh method have been used. The overset grid methodology [49], also called the Chimera grid embedding scheme, is widely used to solve problems with relative motions of solid bodies or moving boundaries. The strategy of this approach utilizes a set of overlapping grids to decompose the computational domain into subdomains in which the solution from one grid is linked to the solution on the overlapping cells [50]. The main innovation of the overset grid methodology is the use of "hole" points which are excluded from calculations such as the inner region of a solid body in the computational domain. Fringe or acceptor cells which are adjacent to hole points are new inter-grid boundary points where the boundary values are required to be obtained by interpolations from the donor cells in the overlapping region [51].

The entire water entry process obtained from the numerical results is in good agreement with the corresponding experiment. The main focus of the study is on the physics of the oblique water entry problem in which the goal is to provide valuable contribution to the research of oblique water entry problems which are widely used in ocean engineering, offshore structures and submarine vehicles. A parametric study has been performed in which the effects of several crucial parameters including head

geometry, entry impact velocity, entry inclined angle, liquid density, viscosity, surface wetness and surface tension on the diving process have been revealed.

A difficulty of the overset mesh implantation in the PLIC-VOF method is the interpolation of the VOF field. Most of the overset interpolation schemes are designed for continuous flow variables. The acceptor value is evaluated by using a weighted average of the ones of its donors. The weighting factors are obtained by using different algebraic methods [52], like `averageValue` method, `injection` method, and `inverseDistance` method. A detailed description of these methods is given in the numerical formulations section. The `inverseDistance` scheme has been applied to calculate the weighting factors in oblique water entry problem.

Unlike the continuous flow variables, the VOF field is a step function near the interfaces, which varies from zero to unity rapidly. In order to transfer the fraction field between the meshes more precisely, a specialized overset interpolation scheme is proposed. This geometric interpolation scheme of the VOF field in overset meshes for the PLIC-VOF method is proposed based on the PLIC-VOF scheme developed by Dai and Tong [44, 45] in the present study. Four testing cases on an unit square/cube are performed to demonstrate the accuracy of the proposed overset interpolation scheme by comparing it with three other algebraic ones. The proposed algorithm has been shown to yield higher accuracy in maintaining interface shape generally.

## 1.2 Organization of Thesis

This thesis is organized as follows. In Chapter 2, the numerical formulations of the oblique water entry model are presented in which the finite volume method (FVM), the governing equations, VOF formulation, overset mesh methodology, and the setup of the numerical model are reviewed in detail. The comparison studies between the numerical results of a free released cylinder entering the water and the

corresponding experimental data are reported. The numerical results are in good agreement with the experimental results, which validates the numerical model used in the present study. In Chapter 3, the physics of the entry process is fully discussed and the effects of several crucial parameters including head geometry, entry impact velocity, entry inclined angle, liquid density, viscosity, surface wetness, surface tension, and the object density during the diving process have been studied. In Chapter 4, the proposed geometric interpolation scheme is explained in detail. Numerical tests of designed 2D and 3D cases are reported in Chapter 5. In the end, conclusions and some potential future work are given in Chapter 6.

# CHAPTER 2

# NUMERICAL FORMULATIONS

In this chapter, the governing equations, VOF formulation, and overset meshes method have been introduced. Due to the low speed of the traveling cylinder, incompressible two-phase laminar flow model is applied. It should be noted that the present study is based on the open source C++ toolbox OpenFOAM. The governing equations are discretized by the finite volume method [53].

## 2.1 Finite Volume Method

The finite volume method (FVM) is a discretization method which is extensively applied in the fields of fluid mechanics, heat and mass transfer, and petroleum engineering [54]. The flow control equations are transformed into discrete algebraic ones by integrating the partial differential equations (PDE) over non-overlapping control volumes. The values of flow variables in each control volume will be evaluated using the discrete algebraic equations. One important feature of the FVM is the local conservativity of the numerical fluxes in which the numerical flux is conserved from one discretization cell to its neighbour. Furthermore, the FVM is known as a cheap method for the discretization of conservation law due to the neat and reliable computational coding for complicated industrial problems.

The FVM can be used on arbitrary geometries with structured or unstructured meshes. Structured meshes are meshes with an implicit connectivity of the points in the mesh. Orthogonal quadrilateral elements are usually used in 2D and hexahedral elements are commonly employed in 3D. It is easy to manage data since the

connectivity between the adjacent cells are straightforward [55]. This feature allows programmers to enumerate the nodes without knowing any connectivity information which results in an ease of programming. However, when handling problems with complex geometries, the increase in grid non-orthogonality or skewness in sensitive regions like boundary layers may affect the accuracy and the cost of numerical calculations.

For unstructured meshes, an elemental cell may have an arbitrary number of neighboring cells attaching to it. Thus, the connectivity information of elements are defined and stored in unstructured meshes. Adjacency lists and coordinate lists are commonly used to map the data to each node. Compared with structured and block unstructured meshes, unstructured meshes provide the necessary flexibility to control the size and orientation of the discretization [56]. It is extensively applied in the problems involved complex geometries since it is very difficult to design a custom-fit mesh to capture all key features of the geometries. Unstructured meshes offer a way to perform anisotropic mesh adaptation. Therefore, it leads to an optimized ratio between the level of accuracy and the computational time for running a simulation. Unstructured meshes are easy to be auto-generated in which the mesh generation process involves two main steps of point creation and definition of connectivity between the points. Unstructured meshes are commonly implemented in commercial softwares and open source platforms like OpenFOAM, STAR-CCM+, ANSYS, COMSOL, etc.

The flow variables can be stored in the cell center which is called cell-centered variable arrangement (see Fig. 2.1(a)) and the values of flow variables can also be stored in the node which is called vertex-centered variable arrangement (see Fig. 2.1(b)). The cell-centered variable arrangement is a widely used variable arrangement with the FVM in which the variables and their related values are stored at the centroids of grid cells. Thus, the method is second order accurate since all

quantities are calculated at element and face centroids, where the difference between the value of the variable and its average is $O(\triangle x^2)$ [53]. The cell-centered variable arrangement with unstructured meshes has been employed in the present study.

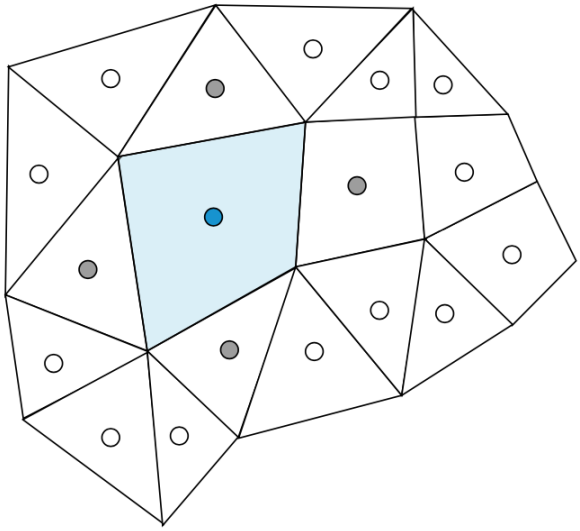

(a) Cell-centered variable arrangement

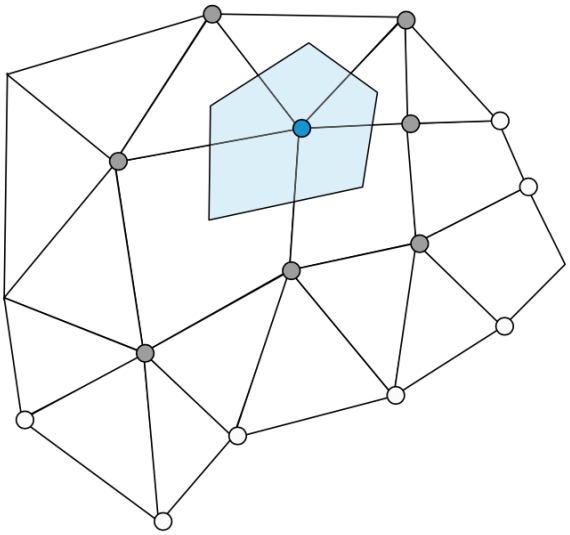

(b) Vertex-centered variable arrangement

Figure 2.1. Variable arrangement in unstructured meshes [53].

## 2.2 Governing Equations

### 2.2.1 Continuity Equation

For incompressible flows with constant properties, the continuity equation is given by:

$$\nabla \cdot \mathbf{U} = 0. \tag{2.1}$$

A polyhedral cell $P$ and its neighbour cell $N$ are shown in Fig. 2.2. The cells shared one face $f$ with an area vector $A_f$.

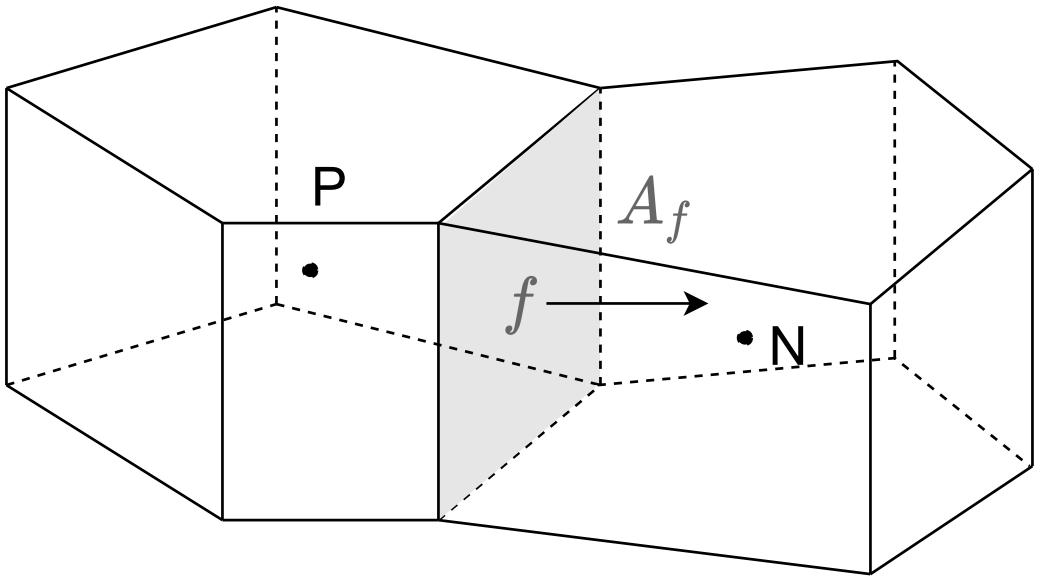


Figure 2.2. Illustration of polyhedral control volume $P$ and its neighbour cell $N$.

After integrating the continuity equation (Eq. 2.1) over the polyhedral control volume $P$ and applying the Gauss's theorem, it yields:

$$\int_{\Omega_P} \nabla \cdot \mathbf{U} d\Omega = \oint_{\partial\Omega_P} \mathbf{U} \cdot d\mathbf{A} = 0, \tag{2.2}$$

where $\Omega_P$ is the volume of control volume $P$, $\partial\Omega_P$ the closed surface bounding the control volume $P$, and $d\mathbf{A}$ surface element with outward-pointing normal vector. For

an unstructured mesh cell $P$ bounding by a set of flat surfaces, the Eq. 2.2 can be written as:

$$\oint_{\partial\Omega_P} \mathbf{U} \cdot d\mathbf{A} = \sum_f \int_f \mathbf{U} \cdot d\mathbf{A} = \sum_f \mathbf{U}_f \cdot \mathbf{A}_f = \sum_f \phi_f = 0, \tag{2.3}$$

where $\phi_f$ is the flux volume across $f$. For time-variant simulations, the time step $\triangle t$ is controlled by the Courant number $C_o$. Considering a computational cell $i$, the Courant number $C_o$ is given by:

$$C_o = \frac{\triangle t \sum_{faces} |\phi_i|}{2\Omega_i}, \tag{2.4}$$

where $\Omega_i$ is the cell volume, $\phi_i$ the face volumetric flux, and $\sum_{faces}$ summation is over all cell faces. The time step is dynamic adjusted during the calculation steps in the program [53].

### 2.2.2 Momentum Equation

For incompressible flows with constant properties, the momentum equation is given by:

$$\frac{\partial}{\partial t}(\rho\mathbf{U}) + \nabla \cdot (\rho\mathbf{U} \otimes \mathbf{U}) = -\nabla p + \nabla \cdot \tau + \rho\mathbf{g} + \mathbf{F}_b, \tag{2.5}$$

where $\rho$ is the density, $p$ the pressure, $\tau$ the stress tensor, $\mathbf{g}$ the gravitational acceleration, and $\mathbf{F}_b$ the body force. Integrating the momentum equation (Eq. 2.5) over the polyhedral control volume $P$ from time $t$ to $t + \triangle t$ yields:

$$\begin{aligned}
&\int_t^{t+\triangle t} \left( \frac{\partial}{\partial t} \int_{\Omega_P} (\rho\mathbf{U})\, d\Omega \right) dt + \int_t^{t+\triangle t} \left( \int_{\Omega_P} \nabla \cdot (\rho\mathbf{U} \otimes \mathbf{U})\, d\Omega \right) dt \\
&= \int_t^{t+\triangle t} \left( \int_{\Omega_P} -\nabla p d\Omega \right) dt + \int_t^{t+\triangle t} \left( \int_{\Omega_P} \nabla \cdot \left( \mu_e \left( \nabla\mathbf{U} + (\nabla\mathbf{U})^T \right) \right) d\Omega \right) dt \\
&+ \int_t^{t+\triangle t} \left( \int_{\Omega_P} (\rho\mathbf{g} + \mathbf{F}_b)\, d\Omega \right) dt,
\end{aligned} \tag{2.6}$$

where $\triangle t$ is the time step. More details about the discretization of the momentum equation can be found in the reference book [53]. The discretized forms of different terms are introduced as follows. For the unsteady term, it can be rewritten as:

$$\int_t^{t+\triangle t} \left( \frac{\partial}{\partial t} \int_{\Omega_P} (\rho \mathbf{U})\, d\Omega \right) dt = \frac{\partial}{\partial t} (\rho \mathbf{U} \Omega)_P \triangle t. \tag{2.7}$$

The first-order Backward Euler method is used to discretize the time derivative term $\frac{\partial}{\partial t}(\rho \mathbf{U}\Omega)$ for the present study, more discussion about the temporal discretization implemented in OpenFOAM can be found in the following session (Temporal Discretization). The temporal discretization of the time derivative term $\frac{\partial}{\partial t}(\rho \mathbf{U}\Omega)$ is given by:

$$\frac{\partial}{\partial t} (\rho \mathbf{U} \Omega)_P = \frac{(\rho \mathbf{U} \Omega)_P^{n+1} - (\rho \mathbf{U} \Omega)_P^n}{\triangle t}, \tag{2.8}$$

where $n$ is the current time level and $n+1$ is the next time level. After applying the Gauss's theorem to the convection term, it yields:

$$\int_t^{t+\triangle t} \left( \int_{\Omega_P} \nabla \cdot (\rho \mathbf{U} \otimes \mathbf{U})\, d\Omega \right) dt = \int_t^{t+\triangle t} \left( \oint_{\partial \Omega_P} (\rho \mathbf{U} \otimes \mathbf{U}) \cdot d\mathbf{A} \right) dt. \tag{2.9}$$

Considering an unstructured mesh bounded by a set of flat faces, it provides:

$$\int_t^{t+\triangle t} \left( \oint_{\partial \Omega_P} (\rho \mathbf{U} \otimes \mathbf{U}) \cdot d\mathbf{A} \right) dt = \int_t^{t+\triangle t} \left( \sum_f (\rho \mathbf{U} \otimes \mathbf{U})_f \cdot \mathbf{A}_f \right) dt. \tag{2.10}$$

Then applying implicit time integration to the non-linear term, the discretized form of the convection term is given by:

$$\begin{aligned} &\int_t^{t+\triangle t} \left( \sum_f (\rho \mathbf{U} \otimes \mathbf{U})_f \cdot \mathbf{A}_f \right) dt = \int_t^{t+\triangle t} \left( \sum_f \rho_f \mathbf{U}_f \phi_f \right) dt \\ &= \left( \sum_f \rho_f^n \phi_f^n \mathbf{U}_f^{n+1} \right) \triangle t. \end{aligned} \tag{2.11}$$

The upwind scheme is applied to evaluate the face velocity $\mathbf{U}_f^{n+1}$. Details about the numerical scheme will be discussed in the following section (Numerical Schemes).

For the pressure term, it can be written as:

$$\int_t^{t+\triangle t}\left(\int_{\Omega_P} -\nabla p d\Omega\right) dt = \left(-\Omega_P^n \left(\nabla p\right)_P^n\right) \triangle t. \tag{2.12}$$

The pressure gradient term is evaluated by the Green-Gauss theorem [57] and it is expressed as follows:

$$\left(\nabla p\right)_P^n = \frac{1}{\Omega_P}\sum_f p_f^n \mathbf{A}_f, \tag{2.13}$$

where $p_f^n$ is the value of the face pressure at current time level $n$. Both cell-averaged-based Gauss gradient (CAG) and node-averaged-based Gauss gradient (NAG) can be employed to evaluate the face pressure value $p_f$. More details about the Green-Gauss theorem applied on unstructured meshes can be found in the following session of Numerical Schemes.

Applying the Gauss's theorm to the diffusion term, it yields:

$$\begin{aligned}
&\int_t^{t+\triangle t}\left(\int_{\Omega_P} \nabla\cdot\left(\mu_e\left(\nabla\mathbf{U}+\left(\nabla\mathbf{U}\right)^T\right)\right) d\Omega\right) dt \\
&= \int_t^{t+\triangle t}\left(\oint_{\partial\Omega_P} \left(\mu_e\left(\nabla\mathbf{U}+\left(\nabla\mathbf{U}\right)^T\right)\right)\cdot d\mathbf{A}\right) dt \\
&= \int_t^{t+\triangle t}\left(\sum_f \left(\mu_e\left(\nabla\mathbf{U}+\left(\nabla\mathbf{U}\right)^T\right)\right)_f \cdot d\mathbf{A}\right) dt \\
&= \int_t^{t+\triangle t}\left(\mu_{e,f}\left(\nabla\mathbf{U}\right)_f\cdot\mathbf{A}_f\right) dt + \int_t^{t+\triangle t}\left(\mu_{e,f}\left(\left(\nabla\mathbf{U}\right)^T\right)_f\cdot\mathbf{A}_f\right) dt \\
&= \int_t^{t+\triangle t}\left(\mu_{e,f}\left(\nabla\mathbf{U}\right)_f\cdot\mathbf{A}_f\right) dt + \left(\sum_f \mu_{e,f}^n\left(\left(\nabla\mathbf{U}\right)^T\right)_f^n\cdot\mathbf{A}_f\right)\triangle t.
\end{aligned} \tag{2.14}$$

$\mathbf{D}$ is the vector between cell $P$ and cell $N$. The face vector $\mathbf{A}_f$ and the vector $\mathbf{D}$ may not be on the same line (shown in Fig. 2.3) since unstructured meshes are non-orthogonal. Thus, the surface vector $\mathbf{A}_f$ can be decomposed into two vectors $\mathbf{E}_f$ and $\mathbf{T}_f$ in which $\mathbf{E}_f$ is on the same direction of vector $\mathbf{D}$ and $\mathbf{T}_f$ is normal to $\mathbf{D}$.

$$\mathbf{A}_f = \mathbf{E}_f + \mathbf{T}_f. \tag{2.15}$$

$\mathbf{E}_f$ is given by [53]:

$$\mathbf{E}_f = \frac{\mathbf{A}_f \cdot \mathbf{A}_f}{\mathbf{D} \cdot \mathbf{A}_f}\mathbf{D}. \tag{2.16}$$

For the body force term, it can be written as:

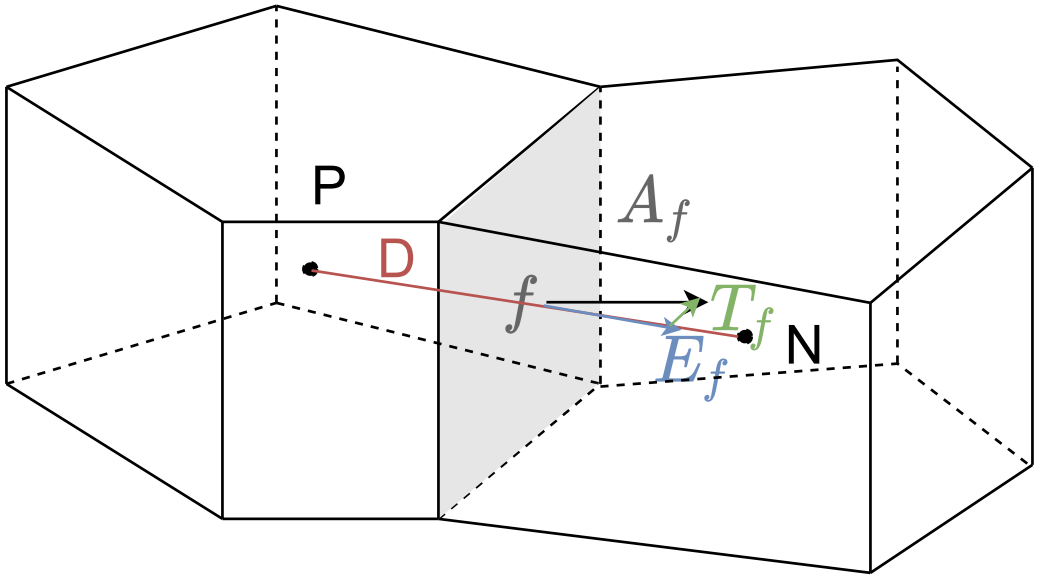


Figure 2.3. Illustration of vectors $\mathbf{D}$, $\mathbf{E}_f$, and $\mathbf{T}_f$.

$$\int_t^{t+\triangle t} \left( \int_{\Omega_P} (\rho \mathbf{g} + \mathbf{F}_b)\, d\Omega \right) dt = \left( \left( \rho_P^n \mathbf{g} + \mathbf{F}_{b,P}^n \right) \Omega_P \right) \triangle t. \tag{2.17}$$

## 2.3 VOF Formulation

The Volume of Fluid (VOF) method [22] which is an Eulerian-based method is widely used to capture the interface in multiphase flows. Both algebraic and geometric approaches have been applied to advect the interface via the VOF equation. The algebraic method lacks accuracy on the normal and curvature calculations due to the discontinuity of the VOF function at the interface which leads to numerical diffusion and results in convergence problems. Considering a computational cell $i$ with the cell

volume of $\Omega_i$, it is composed of a liquid-phase and a gas-phase region. The indicator function G is given by:

$$G(\mathbf{x},t) = \begin{cases} 1 & \text{for } \mathbf{x} \text{ in the liquid phase at time t,} \\ 0 & \text{for } \mathbf{x} \text{ in the gas phase at time t.} \end{cases} \tag{2.18}$$

The liquid fraction of a computational cell ($\Omega_i$) represented by a scalar variable $F$ is given by:

$$F(\mathbf{x}_i,t) = \frac{1}{\mid \Omega_i \mid} \int_{\Omega_i} G(\mathbf{x},t)dV, \tag{2.19}$$

with zero for the gas phase, unity for the liquid phase, and value between zero and unity for interface cells as shown in the equation below.

$$F = \begin{cases} 1 & \text{in the fluid,} \\ 0 < F < 1 & \text{at the interface,} \\ 0 & \text{external to fluid.} \end{cases} \tag{2.20}$$

The governing equation of mass conservation and the VOF equation without phase-change are given by:

$$\frac{\partial \rho}{\partial t} + \nabla \cdot (\mathbf{U}\rho) = 0, \tag{2.21}$$

and

$$\frac{\partial F}{\partial t} + \nabla \cdot (F\mathbf{U}) = 0, \tag{2.22}$$

respectively. Both algebraic and geometric methods have been used to solve the VOF equation. It should be noted that the algebraic family suffers from numerical diffusion at the interface due to the discontinuity property indicated by Eq. 2.20. As for the geometric scheme, the interface can be kept sharp while maintaining the mass conservation at the expense of an extra reconstruction step [58]. The piecewise

linear interface calculation (PLIC) method is one of the most widely used geometric approaches for interface reconstructions [41]. In the PLIC method, the interface is approximated by an oriented plane $\vec{n} \cdot \vec{X} + D_0 = 0$, where $\vec{n}$ is the unit outward normal vector of the interface and $D_0$ the signed distance from the origin. The PLIC-VOF method is used to reconstruct the interface and offers improved accuracy of the interface location while maintaining mass conservation.

In the present study, the cell-centered flow variables and their face interpolated values are used in the solution procedure. Considering a computational cell $i$ with the cell volume of $\Omega_i$, Eq. 2.22 can be rewritten in integral form as:

$$\int_{\Omega_i} \frac{\partial F}{\partial t} d\Omega + \int_{\partial\Omega_i} \nabla \cdot (F\mathbf{U}) d\Omega = 0. \tag{2.23}$$

Integrating the VOF equation over the control volume of cell $i$ from $t$ to $t + \triangle t$ yields [59]:

$$\begin{aligned} &\int_t^{t+\triangle t} \left( \int_{\Omega_i} \frac{\partial F}{\partial t} d\Omega \right) dt \\ &+ \int_t^{t+\triangle t} \left( \int_{\Omega_i} \nabla \cdot (F\mathbf{U}) d\Omega \right) dt = 0. \end{aligned} \tag{2.24}$$

In OpenFOAM, the advection term has been rewritten as:

$$\int_{\Omega_i} \frac{\partial F}{\partial t} d\Omega + \int_{\partial\Omega_i} \nabla \cdot (F\mathbf{U}) \cdot \boldsymbol{n} dS = 0. \tag{2.25}$$

By applying the first order discretization schemes, explicit time integration method, and divergence theorem [45], Eq. 2.24 is rewritten as:

$$\frac{F_i^{n+1} - F_i^n}{\triangle t} = -\frac{1}{\mid \Omega_i \mid} \sum_f \left( F_f^n \phi_f^n \triangle t \right), \tag{2.26}$$

where $\phi_f^n$ is the volume flux and $F_f^n \phi_f^n \triangle t$ represents the liquid volume transported across face $f$ from $t$ to $t + \triangle t$.

## 2.4 Overset Meshes Method

The overset grid method, also known as Chimera grid embedding scheme, utilizes a set of overlapping grids to discretize a complex computational domain into a number of simpler grids [60]. The strategy of overset meshes is to transfer flow variables between multi-block grid systems by interpolations in which the solution from one grid is linked to the solution on the overlapping grids. The overlapping grid system requires identification of "hole" points which are excluded from the flow solving process. In the Chimera grid embedding terminology, hole points (grey region in Fig. 2.4) are the points usually inside of a solid body or behind a symmetry plane [61]. The interpolation process is illustrated in Fig. 2.4, which depicts a portion of the overlapping region between background mesh and body mesh. The entire computational domain is represented by the background cells (blue) and the body cells (red) contain the moving object. The boundary cells of the background and body meshes are acceptors where the required values of flow variables are obtained by interpolations from donor cells. As shown in Fig. 2.4, the first layer of cells with blue squares in the background mesh which are next to hole points are acceptor cells where flow variables are transferred from the overlapping body mesh cells by interpolations. Correspondingly, grids of the body mesh that contain red circles (shown in Fig. 2.4) are also acceptor cells, which can receive interpolated values of the flow field from the background mesh cells. For example, the acceptor cell $a$ is overlapped with six donor cells from the background mesh ($d_1, ..., d_6$ with blue squares).

In the algebraic interpolation scheme, the VOF value $F$ of an acceptor cell is given by:

$$F_a = \sum_{i=1}^{N_d} \omega_i F_{d,i}, \tag{2.27}$$

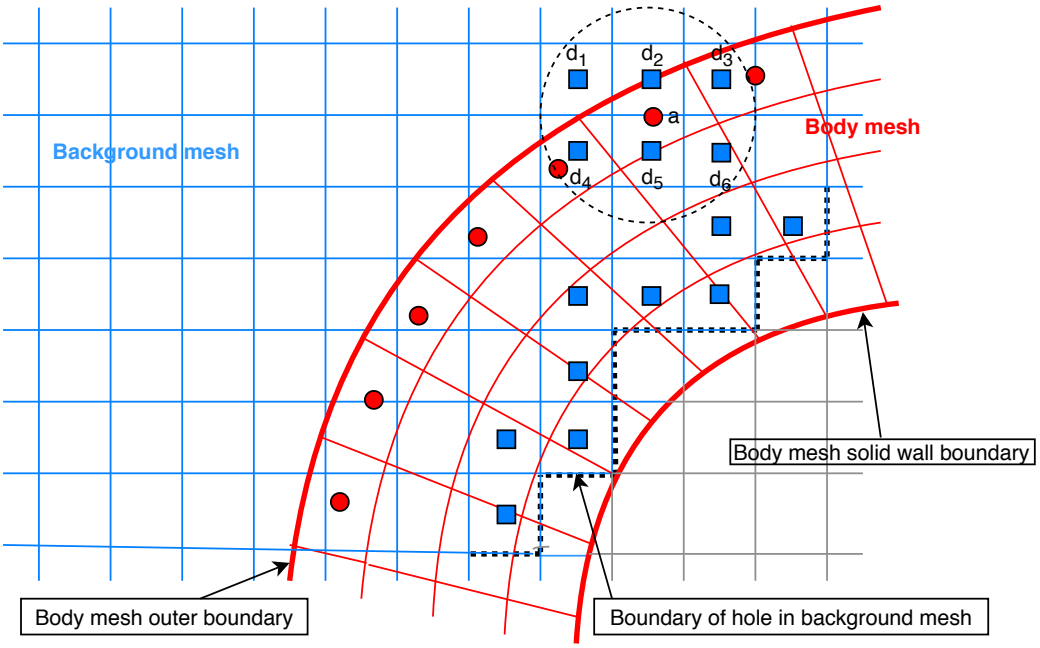


Figure 2.4. Detailed view of overlapping region.

where $F_a$ is the VOF value of the acceptor cell, $N_d$ the total number of the donor cells which overlap with the acceptor cell, $F_{d,i}$ the VOF value of the $i$th donor cell and $\omega_i$ the weighting factors. There are a few ways to calculate weighting factors [62]. The inverse-distance method which is based on the distance between the centroid of the acceptor cell and the centroid of the donor cells is employed in the present study and weighting factors are given by:

$$\omega_i = \frac{\frac{1}{\|X_a - X_{d,i}\|}}{\sum_{i=1}^{N_d} \frac{1}{\|X_a - X_{d,i}\|}}, \tag{2.28}$$

where $X$ is the coordinate of the centroid. A practical application of the Chimera grid embedding scheme is to solve problems involving relative movements since each body grid is independent of the other grids. Correspondingly, governing equations of body and background cells are solved independently. In the present study, unstructured hexahedron meshes and tetrahedron meshes are applied in the background meshes and body meshes, respectively.

## 2.5 Numerical Model Setup

### 2.5.1 Numerical Schemes

#### 2.5.1.1 Temporal Discretization

For the time derivative terms, OpenFOAM core library provides three different schemes named `Euler`, `backward`, and `CrankNicolson` [63]. The `Euler` scheme (Eq. 2.29) in OpenFOAM is implemented as a first-order backward Euler algorithm which is implicit and very stable. The scheme is given by:

$$\frac{\partial}{\partial t}(\phi) = \frac{\phi^{n+1} - \phi^{n}}{\triangle t}, \tag{2.29}$$

where $\phi$ is the volume flux, $n$ the current time level, and $n+1$ the next time level. `backward` (Eq. 2.30) is an implementation of the second-order three-time-steps backward Euler scheme. The scheme is given by:

$$\frac{\partial}{\partial t}(\phi) = \frac{1}{\triangle t}\left(\frac{3}{2}\phi^{n+1} - 2\phi^{n} + \frac{1}{2}\phi^{n-1}\right), \tag{2.30}$$

where $n-1$ is the previous time level. `CrankNicolson` is a modified Crank-Nicolson scheme where an off-center parameter with a value in the range of 0 and 1 is employed to control the weight toward either standard Crank-Nicolson scheme or the implicit Euler scheme. When using uniform time steps, the scheme is given by:

$$\frac{\partial}{\partial t}(\phi) = \frac{\phi^{n+1} - \phi^{n-1}}{2\triangle t}. \tag{2.31}$$

Both `backward` and `CrankNicolson` are second-order in which `CrankNicolson` is bounded but `backward` is not bounded. Therefore, the `backward` scheme can not be applied to the transport equation for the liquid field since it will lead to extreme difficulty to control a bounded solution of the VOF values within 0 and 1. `Euler` scheme is stable and bounded which is applied in the present study.

#### 2.5.1.2 Gradient Schemes

The Green-Gauss method, which is also called divergence theorem, is widely applied for calculating divergence in FVM. The pressure gradient term is evaluated by the second-order accurate Green-Gauss theorem. In OpenFOAM, the built-in gradient schemes are listed in Table 2.1.

Table 2.1. Available gradient schemes in OpenFOAM [64]

| **Gradient Scheme** | **Description** |
|---|---|
| Gauss | Second order, Gaussian integration |
| leastSquares | Second order, least squares |
| fourth | Fourth order, least squares |
| cellLimited | Cell limited version of one of the above schemes |
| faceLimited | Face limited version of one of the above schemes |

The Green-Gauss theorem is based on a derivative of the divergence theorem which is given by:

$$\int_{\Omega_P} \nabla\phi d\Omega = \int_{S_P} \phi \mathbf{n} ds, \tag{2.32}$$

where $\Omega_P$ is the volume of cell $P$, $S_P$ its bounding surface, $\mathbf{n}$ the outwards unit vector perpendicular to $S_P$ at each point, $d\Omega$ and $ds$ the infinitesimal elements of the volume and surface, respectively [57]. The bounding surface $S_P$ can be decomposed into a set of flat faces ($N$ faces) which are denoted by $S_f$, $f = 1, ..., N$. The normal unit vector $\mathbf{n}$ has a constant value $\mathbf{n}_f$ along each face $f$. The Eq. 2.32 can be rewritten as:

$$\int_{\Omega_P} \nabla\phi d\Omega = \sum_{f=1}^{N} \left( \mathbf{n}_f \int_{S_f} \phi ds \right). \tag{2.33}$$

According to the midpoint integration rule [65], the mean value of a quantity over cell $P$ (face $f$) is equal to the summation of its value at the centroid $\boldsymbol{P}$ of the cell

(center of the face $\boldsymbol{c}_f$) and a second-order correction term. Applying this to mean values of $\nabla\phi$ and $\phi$ over $\Omega_P$ and $S_f$, it yields:

$$\frac{1}{\Omega_P}\int_{\Omega_P}\nabla\phi d\Omega = \nabla\phi\left(\boldsymbol{P}\right) + \boldsymbol{O}\left(h^2\right) \Rightarrow \int_{\Omega_P}\nabla\phi d\Omega = \nabla\phi\left(\boldsymbol{P}\right)\Omega_P + \boldsymbol{O}\left(h^4\right), \quad (2.34)$$

$$\frac{1}{S_f}\int_{S_f}\phi ds = \phi\left(\boldsymbol{c}_f\right) + \boldsymbol{O}\left(h^2\right) \Rightarrow \int_{S_f}\phi ds = \phi\left(\boldsymbol{c}_f\right)S_f + \boldsymbol{O}\left(h^3\right), \quad (2.35)$$

where $h$ is a characteristic grid spacing. Applying the Green-Gauss theorem to the above equations, it yields:

$$\nabla\phi\left(\boldsymbol{P}\right) = \frac{1}{\Omega_P}\sum_{f=1}^{N}\phi\left(\boldsymbol{c}_f\right)S_f\mathbf{n}_f + \boldsymbol{O}\left(h\right). \quad (2.36)$$

If the unknown term $\boldsymbol{O}\left(h\right)$ is dropped, it leads to a first-order accurate approximation. For the pressure gradient term at time level $n$, after replacing $\phi$ with $p$, the equation is given by:

$$\left(\nabla p\right)_P^n = \frac{1}{\Omega_P}\sum_{f=1}^{N}p\left(\boldsymbol{c}_f\right)S_f\mathbf{n}_f + \boldsymbol{O}\left(h\right). \quad (2.37)$$

Rewriting $S_f\mathbf{n}_f$ to the area vector $\mathbf{A}_f$ and $p(\boldsymbol{c}_f)$ to $p_f$, the above equation can be simplified as:

$$\left(\nabla p\right)_P^n = \frac{1}{\Omega_P}\sum_{f=1}^{N}p_f^n\mathbf{A}_f. \quad (2.38)$$

This is the deriving process for Eq. 2.13.

Cell-averaged-based Gauss gradient (CAG) and node-averaged-based Gauss gradient (NAG) methods are commonly used to evaluate the face pressure value $p_f$.

In CAG scheme, the value of $p_f$ is approximated by linear interpolation between $p_P$ and $p_N$. A weighting factor $\alpha$ is introduced and given by:

$$p_f = \alpha p_P + (1-\alpha)p_N, \quad (2.39)$$

where the weight factor $\alpha$ is evaluated by the vectors between the face center and cell centroids.

$$\alpha = \frac{|\mathbf{r}_N\cdot\mathbf{A}_f|}{|\mathbf{r}_P\cdot\mathbf{A}_f| + |\mathbf{r}_N\cdot\mathbf{A}_f|}, \quad (2.40)$$

where $\mathbf{r}_P$ is the vector between the centroid of cell $P$ and the face center, $\mathbf{r}_N$ the vector between the centroid of cell $N$ and the face center (shown in Fig. 2.5).

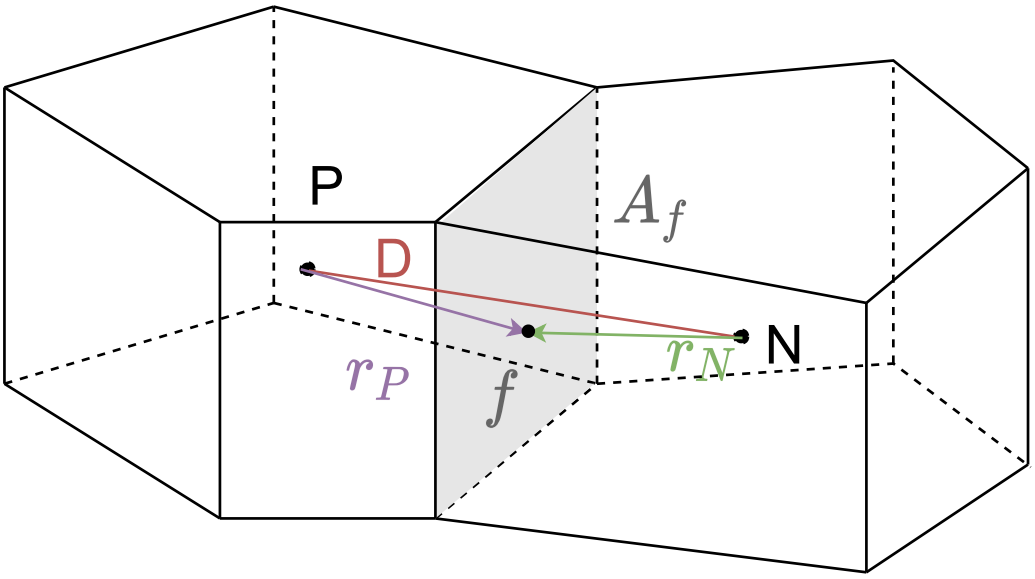


Figure 2.5. Illustration of the vectors $\mathbf{r}_P$ and $\mathbf{r}_N$.

The CAG method is face-based and the result is second order accurate when the intersection point $f'$ of the vector $\mathbf{D}$ coincides with the face center $\boldsymbol{c}_f$. However, in unstructured meshes, the intersection point $f'$ may not coincide with the face center $\boldsymbol{c}_f$ (see Fig. 2.6). The face pressure value $p_f$ needs to be corrected considering the skewness of the mesh. A iterative way to calculate $p_f$ is proposed by Maric *et al* [66].

For the NAG method, the node pressure $p_{n_i}$ is applied to calculate the face pressure $p_f$ (see Fig. 2.7). The equation is given by:

$$p_f = \frac{\sum_{i=1}^{N_n} \frac{p_{n_i}}{\|\mathbf{X}_{n_i} - \mathbf{X}_f\|}}{\sum_{i=1}^{N_n} \frac{1}{\|\mathbf{X}_{n_i} - \mathbf{X}_f\|}}, \tag{2.41}$$

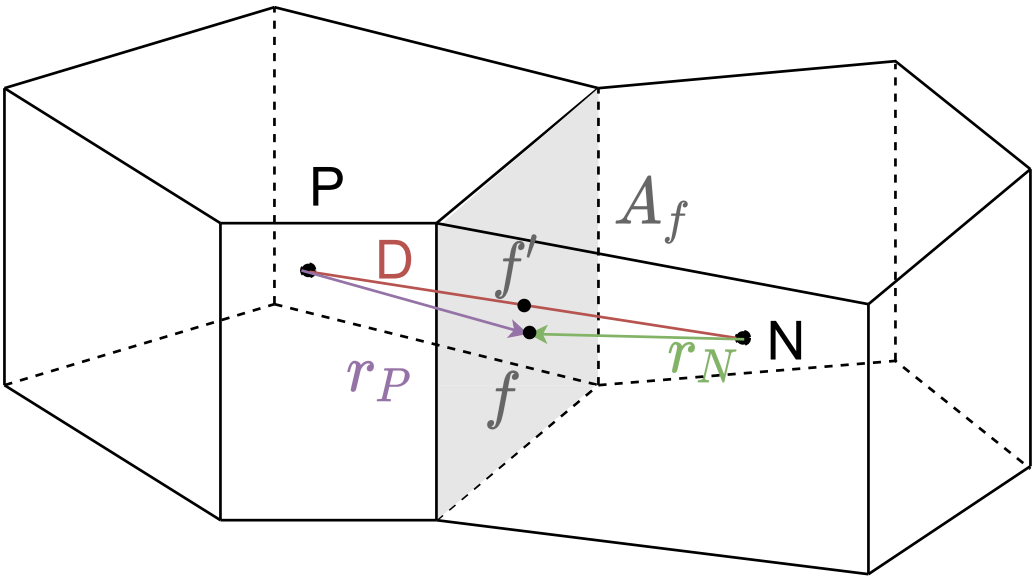


Figure 2.6. Illustration of the intersection point $f'$ and the face centroid.

where $N_n$ is the number of the vertices for face $f$. The node pressure $p_{n_i}$ is evaluated by the surrounding control volumes of the mesh node with inverse-distance weighting factors. The equation of calculating $p_{n_i}$ is given by:

$$p_{n_i} = \frac{\sum_{i=1}^{N_c} \frac{p_{c_i}}{\|\mathbf{X}_{n_i} - \mathbf{X}_{c_i}\|}}{\sum_{i=1}^{N_n} \frac{1}{\|\mathbf{X}_{n_i} - \mathbf{X}_{c_i}\|}}, \tag{2.42}$$

where $N_c$ is the number of the surrounding cells of the node $n_i$, $c_i$ the $i$-th adjacent control volume of this node [66].

#### 2.5.1.3 Convection Discretization

Applying for the Green-Gauss theorem to the convection term (see Eq. 2.9 to Eq. 2.11), the face fluxes are evaluated. In Eq. 2.11, the face velocity $\mathbf{U}_f^{n+1}$ is calculated by convection scheme. Many of the convection schemes available in OpenFOAM are based on Total Variation Diminishing (TVD) [67] and Normalised Variable Diagram (NVD) schemes [68]. The commonly used convection schemes are listed in Table 2.2. It should be noted that the boundedness of TVD/NVD schemes is only

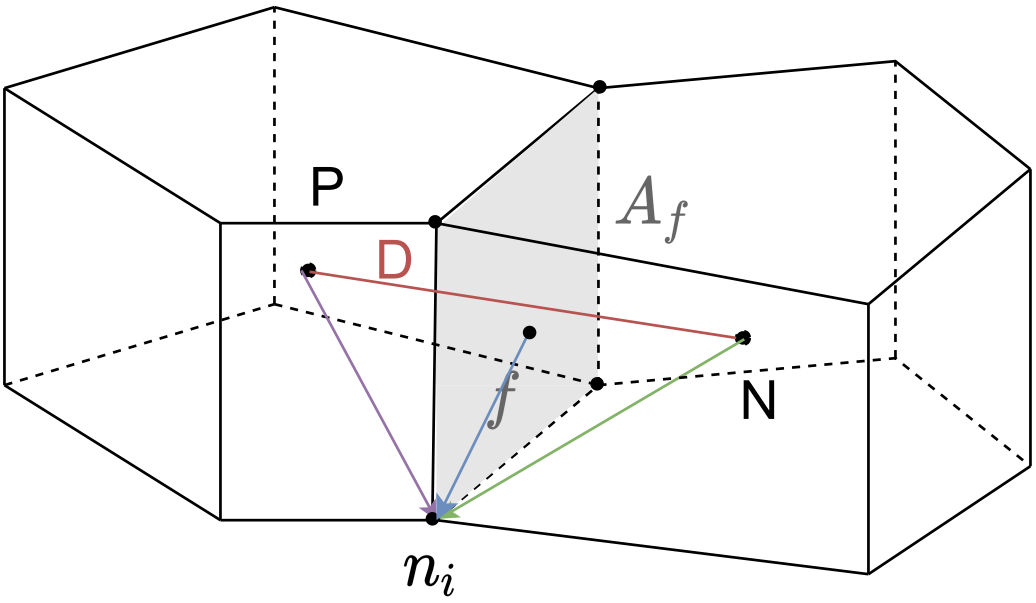


Figure 2.7. Illustration of the node $n_i$.

guaranteed for 1-D cases. The boundedness can be improved in 2D and 3D cases by limiting the gradient.

Table 2.2. Available convection schemes in OpenFOAM [64]

| **Convection Scheme** | **Description** |
|---|---|
| upwind | First order, bounded |
| linearUpwind | Second order, bounded |
| linear | Second order, unbounded |
| vanLeer | Second order, bounded |

The upwind scheme is employed in the present study. Therefore, for the face velocity $\mathbf{U}_f^{n+1}$ in Eq. 2.11 can be rewritten as:

$$\mathbf{U}_f^{n+1} = sgn(\phi_f^n)\mathbf{U}_P^{n+1} - sgn(\phi_f^n)\mathbf{U}_N^{n+1}. \tag{2.43}$$

In OpenFOAM, there are also some non-TVD/NVD convection schemes. More details can be found in the OpenFOAM user guide [64].

#### 2.5.1.4 PIMPLE Scheme

OpenFOAM provides three different pressure-velocity coupling methods for solving Eq. 2.1 and Eq. 2.5: Pressure Implicit with Splitting of Operator (PISO), Semi-Implicit Method for Pressure-Linked Equations (SIMPLE), and PIMPLE. The PIMPLE pressure-velocity coupling algorithm is a combination of PISO and SIMPLE schemes. PIMPLE and PISO are applied for transient cases and SIMPLE is used for steady-state cases. The PIMPLE algorithm offers an outer correction loop which loops through all variables of Navier–Stokes equations. If no outer corrector loops are applied, the PIMPLE method is equivalent to the PISO algorithm. The PIMPLE algorithm combines an implicit momentum predictor and several pressure-velocity correctors. Initially, the velocity equations are solved explicitly by using the velocity and pressure fields of the previous time step which is called momentum predictor. Then velocity matrix is split into diagonal and off diagonal components. The semi-discretized form of the momentum equation can be written as:

$$a_P \mathbf{U}_P = \mathbf{H}(\mathbf{U}) - \nabla p, \tag{2.44}$$

where $a_P$ is the diagonal coefficients of the matrix resulting from the discretization of the momentum equation, $\mathbf{H}(\mathbf{U})$ the non-diagonal coefficients and source terms apart from the pressure gradient. The non-diagonal coefficent is mostly composed by convective and diffusive terms and the source terms are composed by the source part of the transient term and source from `UEqn`. In the momentum predictor step,

the velocity is solved implicitly which leads to an dissatisfaction of the continuity equation. From Eq. 2.44, we can get:

$$\mathbf{U}_P = \frac{\mathbf{H}(\mathbf{U})}{a_P} - \frac{1}{a_P}\nabla p. \tag{2.45}$$

Then, the velocity and pressure are corrected by iterations to satisfy the mass conservation (see Eq. 2.46) [69].

$$\nabla \cdot \mathbf{U}_P = \nabla \cdot \left(\frac{\mathbf{H}(\mathbf{U})}{a_P}\right) - \nabla \cdot \left(\frac{1}{a_P}\nabla p\right) = 0. \tag{2.46}$$

A flowchart of PIMPLE solution procedure in OpenFOAM is shown in Fig 2.8. The `nOuterCorr` is the number of outer corrector loops which represents the number of times that loops for the entire PIMPLE loop. It loops through all Navier-Stokes variables. `outerCorr` represents how many times out corrector has looped till current time. The `nNonOrthoCorr` is the number of the non-orthogonal pressure corrector loops and the `nCorr` is the number of loops for pressure correction to obtain mass conservative fluxes in which it loops only through `pEqn`. A summary of numerical schemes of the present study in shown in Table 2.3.

Table 2.3. Summary of numerical schemes applied in the model

| **Discretization** | **Schemes** | **Description** |
|---|---|---|
| time scheme | Euler | first-order backward Euler<br>bounded<br>implicit |
| gradient | Gauss | second order |
| laplacian surface normal gradient | uncorrected | first order<br>bounded |
| pressure-velocity coupling | PIMPLE | Combine PISO and SIMPLE schemes |

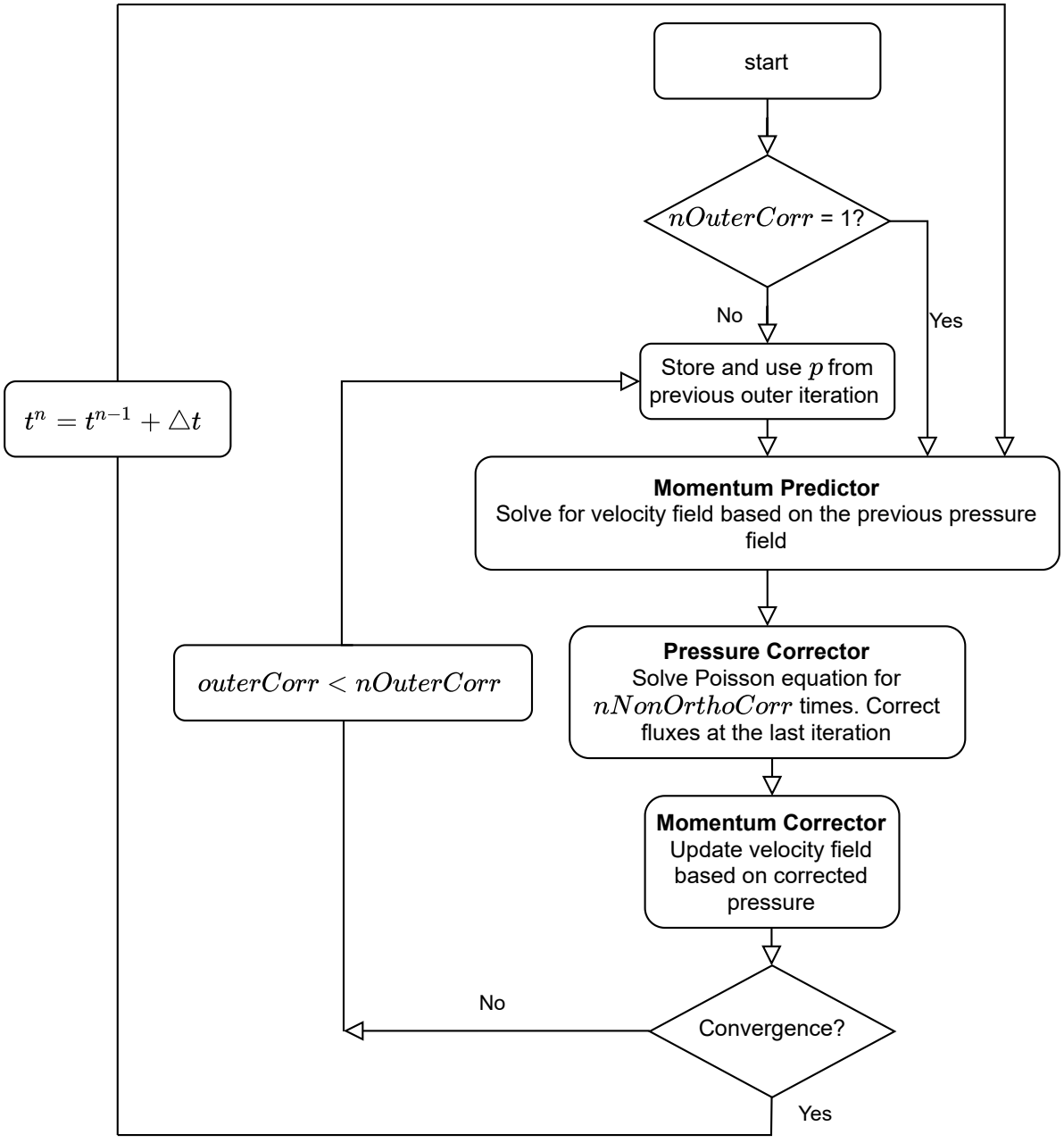


Figure 2.8. Flowchart of PIMPLE scheme in OpenFOAM.

### 2.5.2 OpenFOAM Setup

An overview of the OpenFOAM case structure is shown in Fig 2.9. A case setup is composed of three directories: `0`, `constant`, and `system`. The initial states are stored in the directory of `0`. The information of mesh, properties of the model and phases, and the setting of the moving cylinder is stored in the directory of `constant`. The mesh numerical schemes and solver are specified in the directory of `system` in which the `overInterPlicDyMFoam` solver is applied in the current study. It should be noted that all numerical tests are run in 64 threads on Texas Advanced Computing Center (TACC) and the settings of the parallel calculations are stored in `decomposeParDict`. More details about OpenFOAM settings can be found in the user guide [64].

## 2.6 Comparisons with Experiments

The present study is motivated by the previously mentioned experimental work of Xia *et al* [16]. A hollow aluminium cylinder with a density ratio $\rho_s/\rho_w = 1.28$ is employed in the experiment in which the $\rho_w$ is 998 $kg/m^3$. The length of cylinder is 180 $mm$, and the diameter is 29 $mm$. Details of the cylinder structure and the settings of the experimental devices can be found in the corresponding experiment [16]. To validate the numerical model, comparisons of the numerical results with the experimental data have been conducted.

The setup and physical properties are same as the experiment [16] (see Table 2.4) in which a cylinder was freely released above the stagnant water surface at a certain inclined angle and axial speed.

In the numerical model, the densities of water and air are 998.2 $kg/m^3$ and 1 $kg/m^3$, respectively. The kinematic viscosity of water is $1 \times 10^{-6}$, and the kinematic

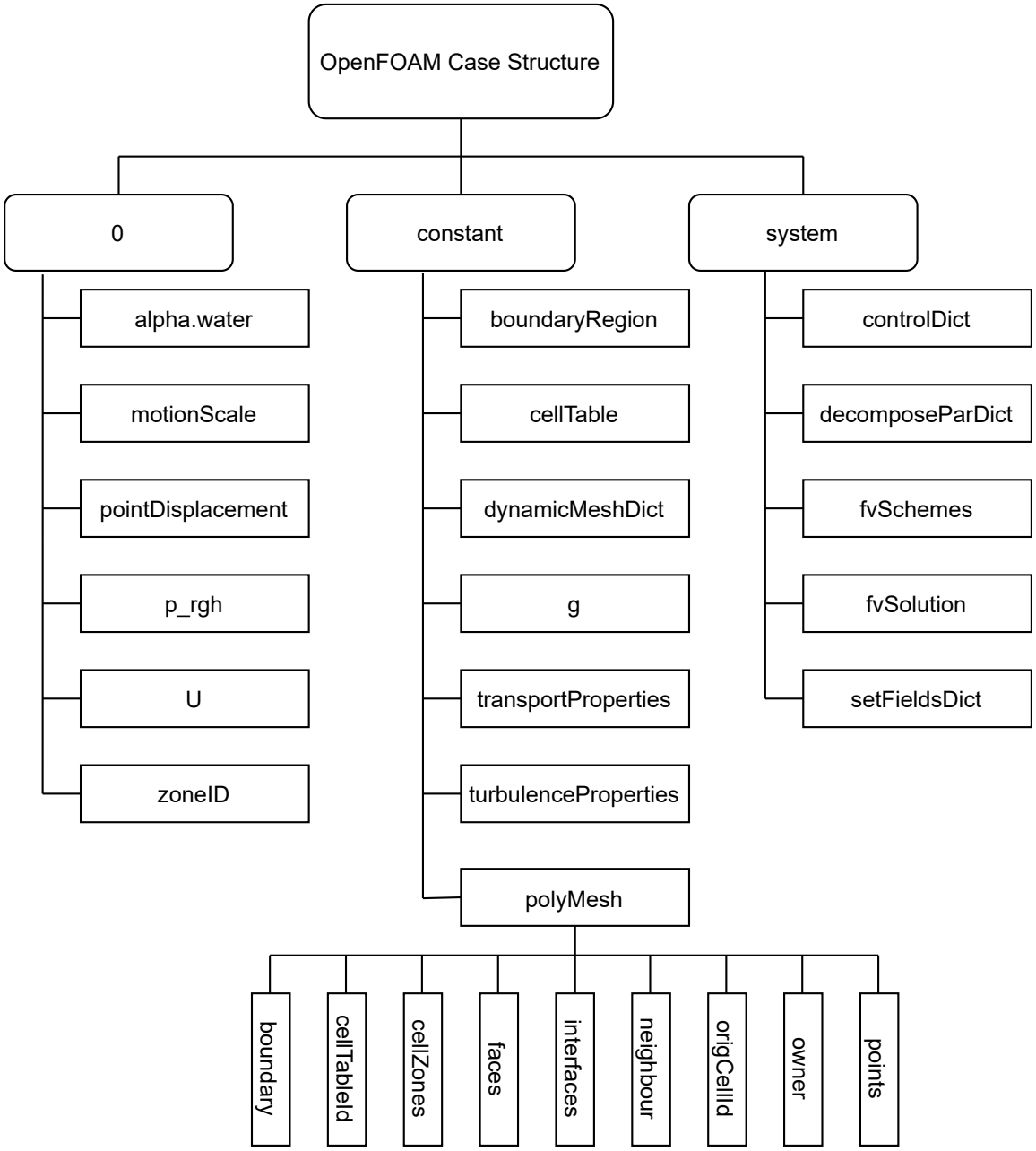


Figure 2.9. An overview of the OpenFOAM case structure.

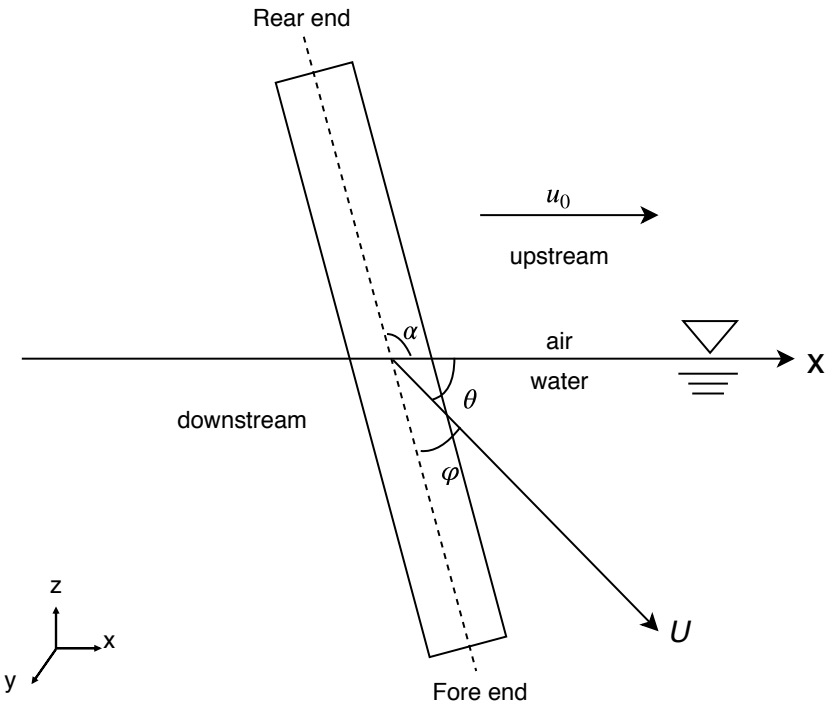


Figure 2.10. Schematic illustration of cylinder in Cartesian coordinate in the experiment.

viscosity of air is $1.48 \times 10^{-5}$. The surface tension is 0.072 $N/m$. A schematic illustration of the experimental setup is shown in Fig. 2.10 with the cylinder advancing side defined as upstream and opposite side downstream. The cylinder end which touches the water surface first is the fore end, while the other end is the rear end. A high-speed camera was used to capture cylinder trajectories after entry. For the ease of describing the initial condition of the cylinder, the inclined angle, entry angle and angle of attack are marked as $\alpha$, $\theta$ and $\varphi$, respectively. Tetrahedron meshes employed on the body mesh and hexahedron meshes applied on the background mesh with grid spacing of 0.005 $m$ are used based on the results of a mesh convergence study which are reported in the Appendix. Phase change is not considered in the numerical model due to the low speed of the moving cylinder. A schematic illustration of the overall

Table 2.4. Setup and physical properties in the numerical model [16]

| **Property** | **Value** | **Unit** |
|---|---|---|
| cylinder length | 180 | $mm$ |
| cylinder diameter | 29 | $mm$ |
| density of cylinder | 1279 | $kg/m^3$ |
| denstiy of water | 998.2 | $kg/m^3$ |
| initial horizontal velocity | 1.34 | $m/s$ |
| initial vertical velocity | 2.35 | $m/s$ |

mesh layout is shown in Fig. 2.11. The body mesh contains the moving cylinder and the background mesh represents the entire computational domain which includes air and water. The cylinder diving process with snapshots at various time instants alongside the corresponding experiment is shown in Fig. 2.12.

It should be noted that time is measured from the instant when the cylinder bottom first touches the water surface. As soon as the cylinder touches the water surface, energy starts to be transferred from cylinder to water which pushes water downstream while forming a thin water film along the cylinder surface at the upstream side and some air trapped on the downstream side in which an air channel starts forming right from the start (Fig. 2.12a). Note that the splash dome is difficult to simulate in the numerical result with limited computational resources. It can be observed that the air channel is open to the atmosphere since the cylinder fore end touches the water surface. As time passes, the air channel continues to expand as the cylinder further penetrates due to the forward movement of the cylinder. The deeper the cylinder, the more the splashes generated above the water.

Projected views of the numerical results are applied to compare with the experimental results in which various views of the air channel at $t = 70ms$ are as shown in Fig. 2.13. A 50% opacity of the interface is applied to better illustrate the air entrap-

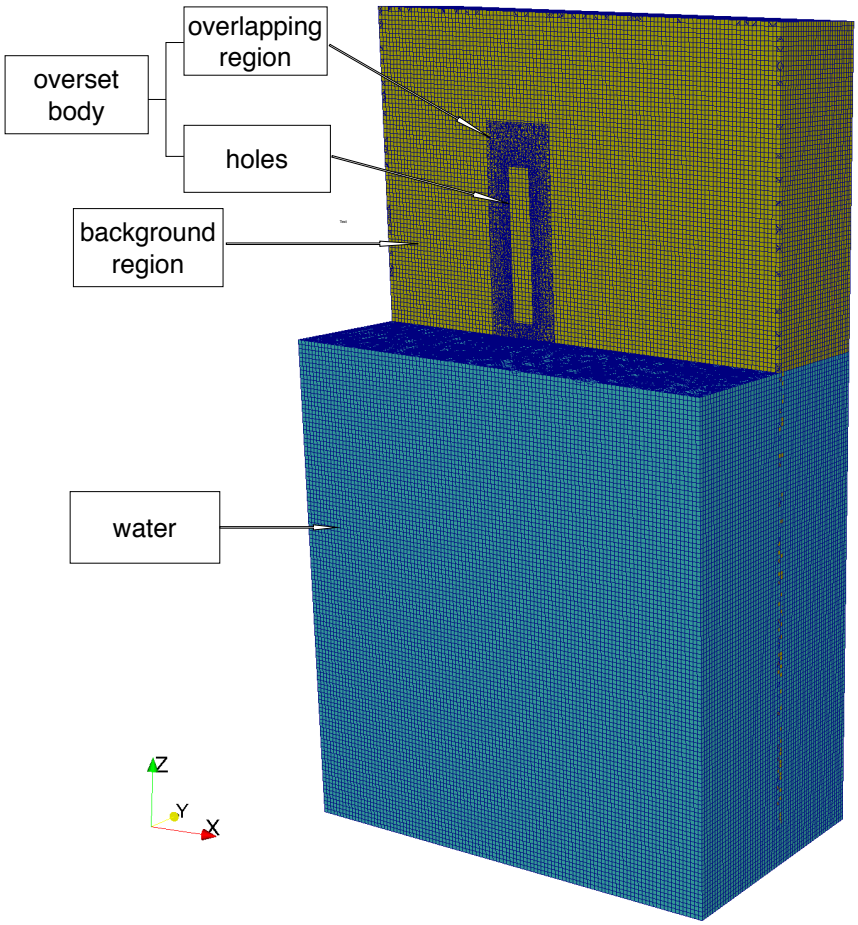


Figure 2.11. Mesh layout in standard testing cases.

ment. A side view of the air channel is shown in Fig. 2.13a with the stagnant water surface presented as a horizontal line. With a small rotation (out-of-plane direction) applied, a perspective view of the cone shape of the air channel is shown in Fig. 2.13b. It can be observed that the air channel is open to the atmosphere and the water is in light blue. Another perspective view with a further rotation is shown in Fig. 2.13c. The top view of the air channel is shown in Fig. 2.13d after further rotation.

The horizontal pressure variation is not obvious due to the low entry speed and the pressure field is dominated by hydrostatic pressure. It is of great importance to

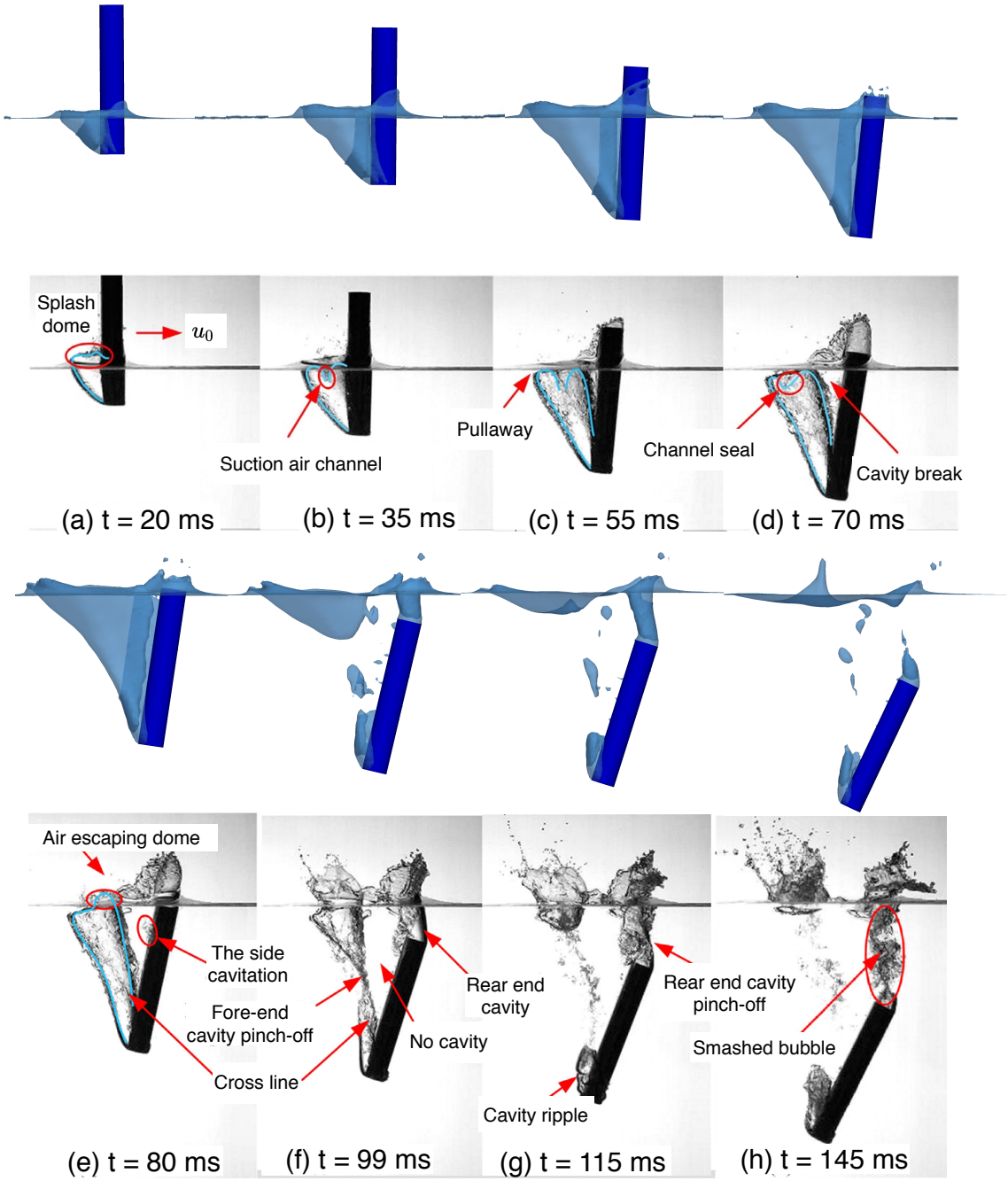


Figure 2.12. Numerical and experimental results [16] of the oblique water entry problem at various time instants:(a) $t = 20ms$, (b) $t = 35ms$, (c) $t = 55ms$, (d) $t = 70ms$, (e) $t = 80ms$, (f) $t = 99ms$, (g) $t = 115ms$, and (h) $t = 145ms$.

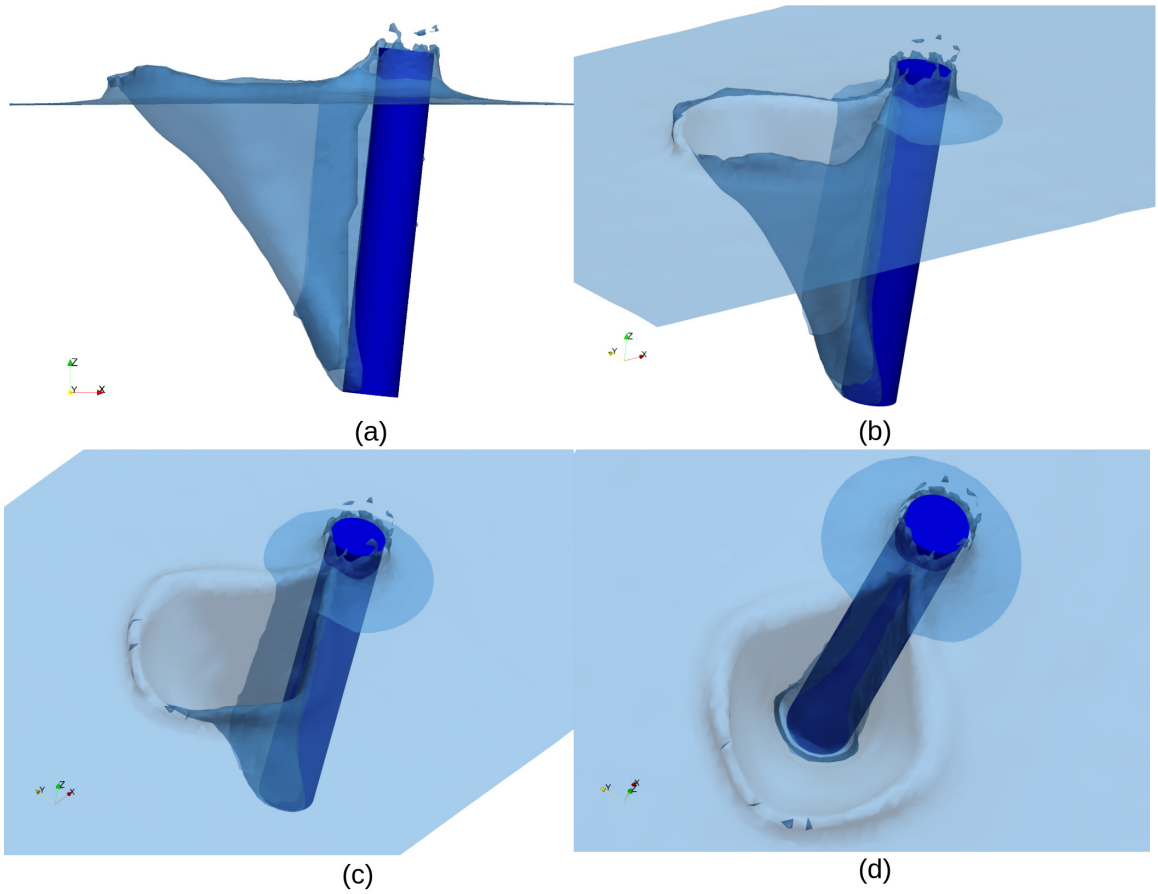


Figure 2.13. Various views of the trapped air channel at $t = 70ms$.

note that the air channel still appears attached to the cylinder surface at $t = 55ms$, $t = 70ms$ and $t = 80ms$ in the numerical result, while the air channel starts detaching from the cylinder at $t = 55ms$ in the experimental result (Fig. 2.12).

As discussed in the work of Zhao *et al.* [70], the water entry phenomenon is significantly influenced by the surface condition of the solid object. Hydrophobic surface (such as coated with soot) typically forms cavities while hydrophilic surface (wetted surface) does not. Duez *et al.* [71] presented a theoretical model, arguing that the entry velocity to form the cavity must be above a threshold velocity, which is dependent on the surface wetness of the solid object. It was found that a huge air cavity was

generated by the hydrophobic sphere, while no such behaviour was observed for the hydrophilic sphere with the two spheres only differed by a nanometric coating that modified the surface wetness. In the present study, a machined aluminium cylinder is employed in the experiment in which aluminium is naturally hydrophilic [16]. Inspired by their work, simulations with hydrophobic and hydrophilic surfaces of the diving cylinder are made to examine the influence of surface wetting on the air entrapment. The detachment of the air channel is not only dominated by the forward movement of the cylinder, but also influenced by the surface condition of the solid object. Details are reported in a later section.

As the diving process continues, it can be observed that the splashes captured in the experiment are larger than those obtained from numerical simulations due to the limited resolution as mentioned previously. The air channel is gradually stretched and eventually breaks into two main parts adjacent to the two ends of the cylinder at around $t = 99ms$. When pinch-off of the air channel occurs, there is a violent collapse generated which drives the side air foam to the cylinder ends. At $t = 115ms$, it can be observed that some air foam still appears adjacent to the fore end while the side foam moves to the rear end and ultimately joins the water surface at around $t = 145ms$. Smashed bubbles and splashes above the water surface are not as significant as captured in the experiment due to the resolution limitation as mentioned previously. Comparisons of penetrating depths and inclinations between numerical simulations and the experiment during the diving process at various time instants are shown in Fig. 2.14 and Fig. 2.15, respectively.

It can be observed that the numerical results of the penetration depths are very close to the experimental data. As the cylinder dives, differences between the numerical results and experimental values are getting slightly larger due to the accumulation of the numerical dissipation, but still less than 0.19%. The inclination is more sen-

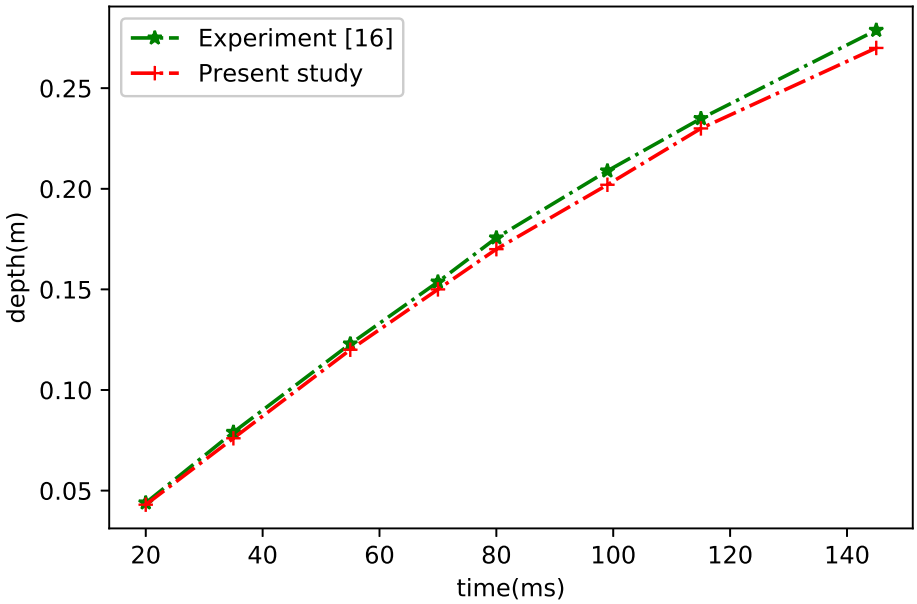


Figure 2.14. Penetration depth of cylinder at various time instants.

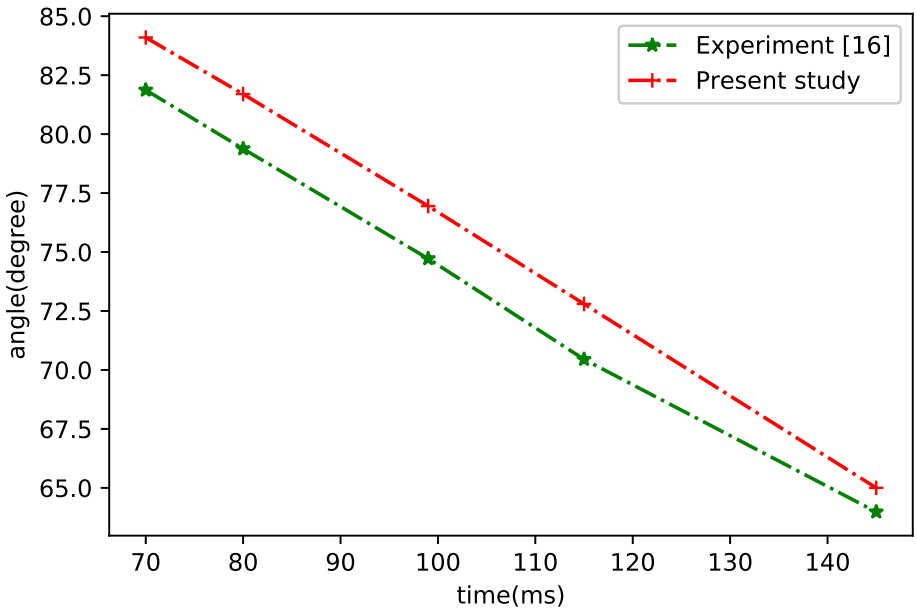


Figure 2.15. Inclined angle of cylinder at various time instants.

sitive to the grid size in which the mesh convergence study has been employed in Appendix. The grid size of $0.005m$ has been applied due to the limitation of computational resources. Details will be discussed in following sections. The numerical results are in good agreement with the corresponding experiment which validates the numerical model used in the present study.

## 2.7 Dimensional Analysis

A dimensional analysis has been performed to assist the study of the fluid physics during the water entry process. Certain dimensionless values have been evaluated. The dimensionless numbers associated with the oblique water entry problem include the liquid density $\rho_w$, dynamic viscosity $\mu$, kinematic viscosity $\nu$, surface tension $\sigma$, the gravity acceleration $g$, and cylinder dimensions. The air entrapment of the diving process may be characterized by the following dimensionless groups: Reynolds number, Weber number, and Bond number. The Reynolds number is the ratio of inertial forces to viscous forces within a fluid and it is given by:

$$Re = \frac{\rho_w u L}{\mu} = \frac{uL}{\nu}, \tag{2.47}$$

where $\rho_w$ is the liquid density, $u$ the flow velocity, $L$ the characteristic length of the object, $\mu$ the dynamic and $\nu$ the kinematic viscosity of the fluid. The Reynolds number indicates the flow regimes of laminar, transient, and turbulent. For the reference case, a projected view of $x-z$ plane of the velocity field at time instant of 99 $ms$ is shown in Fig. 2.16. It can be seen that the fluid velocity is very small due to the small impact velocity of the cylinder ($u_0 = 1.34\ m/s$, $v_0 = 2.35\ m/s$. Thus, the Reynolds number is smaller than 2000 at 99 $ms$ which indicates a laminar flow. The

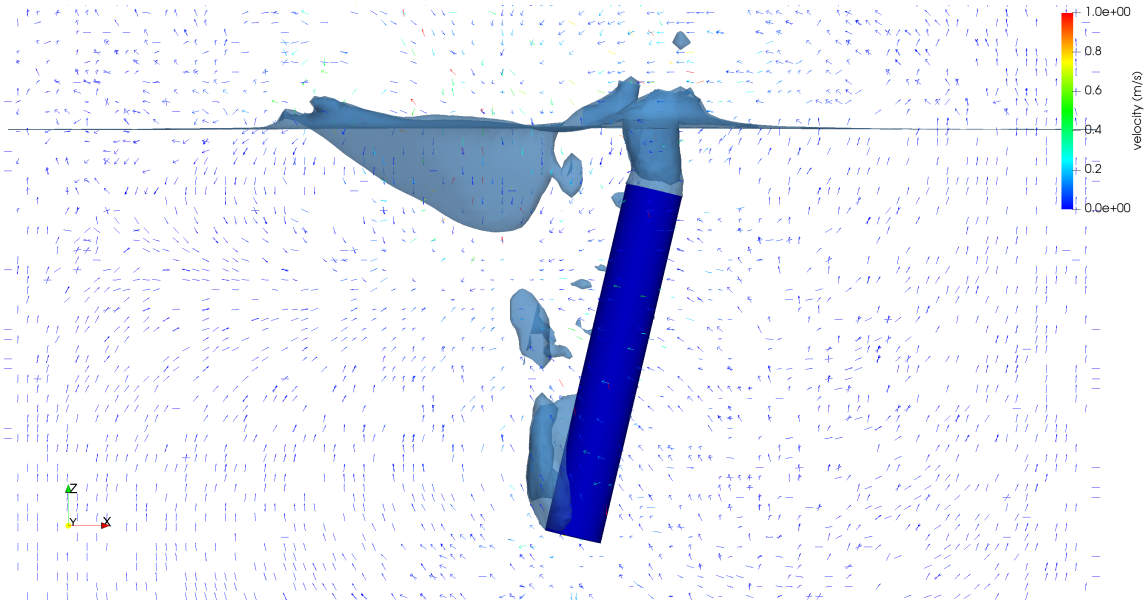


Figure 2.16. The velocity field for the reference case at 99 $ms$.

Weber number is a measure of the relative importance of the fluid's inertia compared to its surface tension. The Weber number is given by:

$$We = \frac{\rho_w u^2 L}{\sigma}, \tag{2.48}$$

where $\sigma$ is the surface tension. Low Weber numbers have been obtained at different time instants due to the small velocities of the fluid. Duez *et al.* [71] found that larger impact velocities are required for hydrophilic spheres to produce a similar cavity compared with the hydrophobic ones when $We$ is larger than $10^3$. The Bond number describes the relative magnitude of gravitational to capillary forces in which the equation is given by:

$$Bo = \frac{\triangle \rho g L^2}{\sigma}, \tag{2.49}$$

where $\triangle \rho$ is the difference in density of the two phases. Based on the parameters applied in the numerical study, the Bond number is larger than 4000 which indicates

the gravity is dominant compared with the surface tension. This conclusion is also proven in the parametric study of surface tension in Chapter 3.

# CHAPTER 3

# NUMERICAL RESULTS AND DISCUSSIONS OF OBLIQUE WATER ENTRY PROBLEMS

In this chapter, a parametric study has been conducted in which the effects of head geometry, entry impact velocity, entry inclined angle, liquid density, viscosity, surface wetness and surface tension on the penetrating process of the oblique water entry problem have been investigated. A summary of parametric studies can be found in Table 3.1 at the end of this chapter.

## 3.1 Head Geometry

The design of naval structures is significantly affected by the hydrodynamics induced by the water entry process of solid projectiles in which previous investigators have considered the solid bodies of various shapes: wedges, spheres, cones, cylinders, flat plates and a number of other shapes [72]. The trapped air during the water entry process plays in an important role in the load characteristics and diving trajectories. In recent years, a number of papers have discussed applications of the shape optimization of marine vehicles [73, 74, 75]. In this framework, three head geometries (flat, cone, dome) have been applied and investigated at given inlet conditions for the water entry process. Air channels trapped by three head configurations with same impacting velocities (horizontal velocity $u_0 = 1.34\ m/s$ and vertical velocity $v_0 = 2.35\ m/s$) at various time instants are shown in Fig. 3.1. This change in head geometry creates different flow patterns as soon as the diving process takes place. It can be observed that almost no air is trapped by the dome head cylinder right

from the start since there is no sharp edges for the dome configuration and the flow passes the cylinder smoothly. As soon as the cylinder touches the water surface, the velocity of the fore end decreases due to the water resistance in which a torque is generated by the velocity difference between the fore end and rear end. Before the cylinder fully submerges, the deeper the cylinder travels, the larger torque generated. Streamlines around cylinders and pressure distributions at $t = 70ms$ are shown in Figs. 3.2 and 3.3, respectively.

It can be seen that more curved streamlines around cylinder heads are created by the dome and cone configurations. As shown in Fig. 3.4, the net rotation of the dome head cylinder is larger than the other two cases. When the cylinder first touches the water surface, the fore end of the cylinder slows down due to the water resistance exerted on it in which the velocity difference between the fore end and rear end increases before the cylinder fully submerges. The velocity difference results in a torque which leads to a larger rotation of the cylinder. After the cylinder fully submerges, the inclination still increases due to the velocity difference at the two ends in which the vertical projected area decreases alongside the rotation. Therefore, a smaller horizontal resistance is exerted on the cylinder which results in a larger inclination. Meanwhile, the horizontal projected area increases due to the larger rotation which leads to a larger vertical resistance to slow down the penetration.

On the other hand, the pressure difference between the upstream and downstream sides of the flat head cylinder is larger since more air is trapped on the downstream side, which leads to a larger resistance in the horizontal direction. Due to the horizontal resistance, inclination of the flat head cylinder is less than the other two cases. Additionally, it has been found that the cone head cylinder rotates less than the dome head one since a larger pressure difference occurs as a result of more air trapped on the downstream side of the cone head cylinder as explained previously.

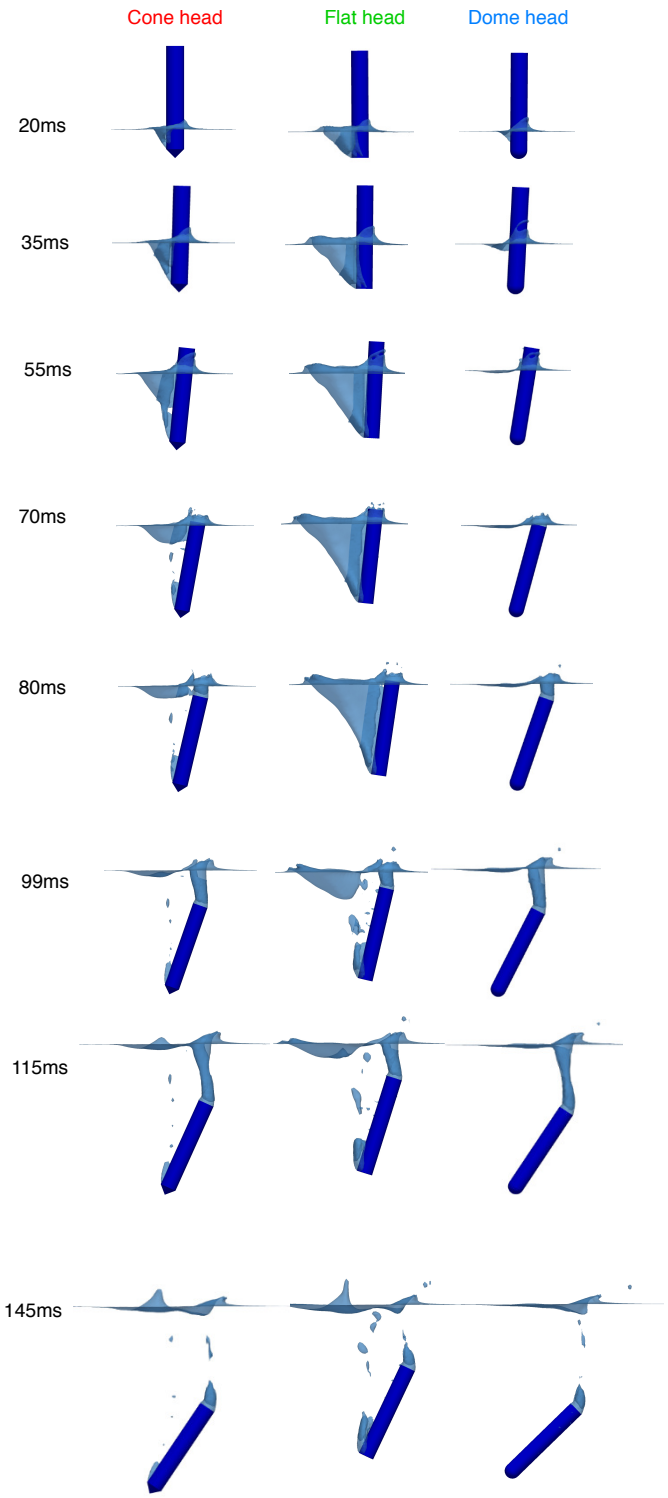


Figure 3.1. Trajectories and air entrapment of cylinders with cone, flat and dome heads.

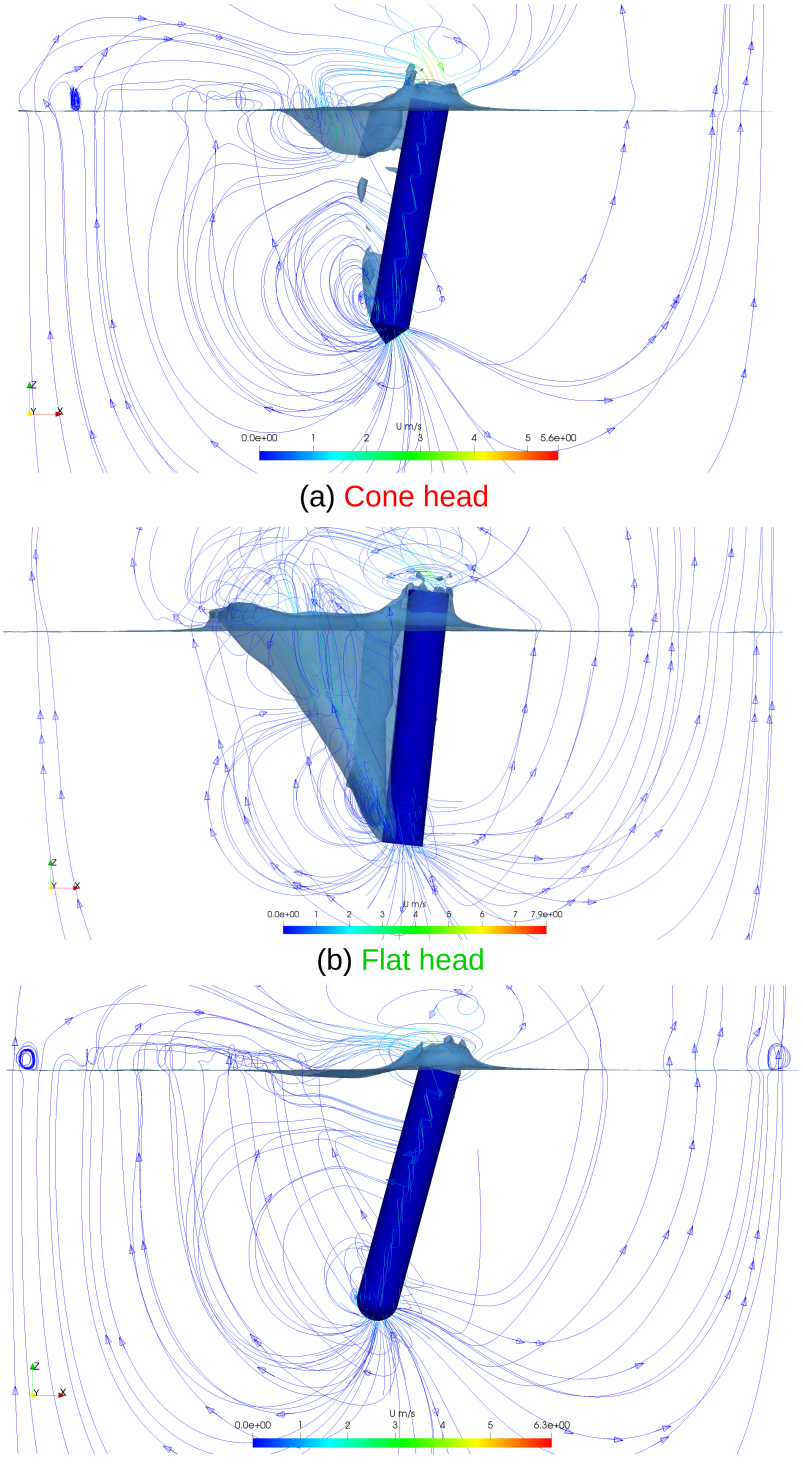


Figure 3.2. Streamlines of cylinders with various head geometries at 70 $ms$.

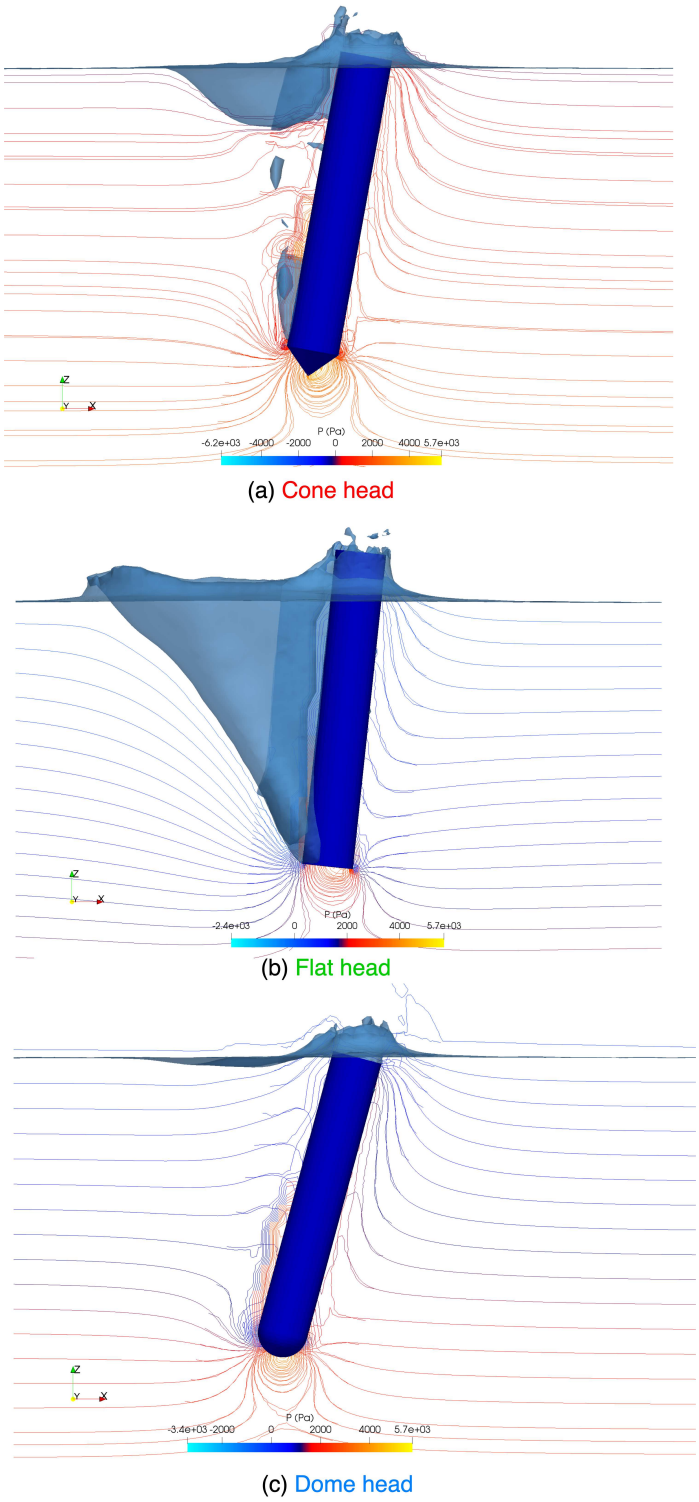


Figure 3.3. Pressure fields of cylinders with various head geometries at $70ms$: (a) Cone head, (b) Flat head, and (c) Dome head.

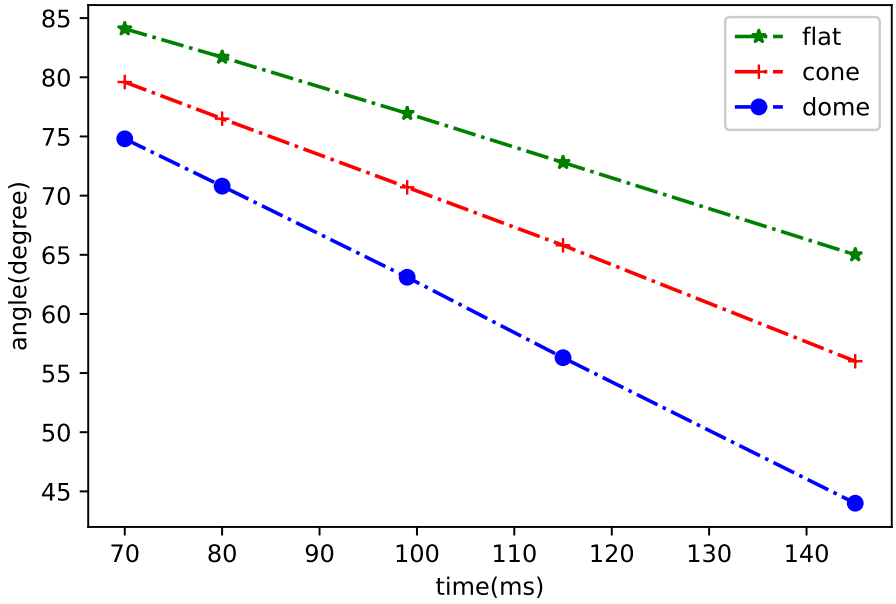


Figure 3.4. Cylinder inclination angle with various head geometries.

As shown in Fig. 3.5, the dome head cylinder penetrates slightly deeper than the cone head one initially. As the diving process continues, the penetration depth of the cone head cylinder catches up with the dome head one, especially after the cylinder has fully submerged (around $t = 80\ ms$). The larger rotation of the dome head cylinder results in a larger horizontal projected area. As a consequence, a larger vertical resistance exerted on the dome head cylinder slows down the penetration of the dome head cylinder and the cone head cylinder gradually catches up.

## 3.2 Entry Impact Velocity

Undoubtedly, the entry velocity greatly affects the penetration and inclination of the cylinder during the water entry process. The effect of the entry velocity on the transport process has been studied by altering the horizontal velocities to 0.67,

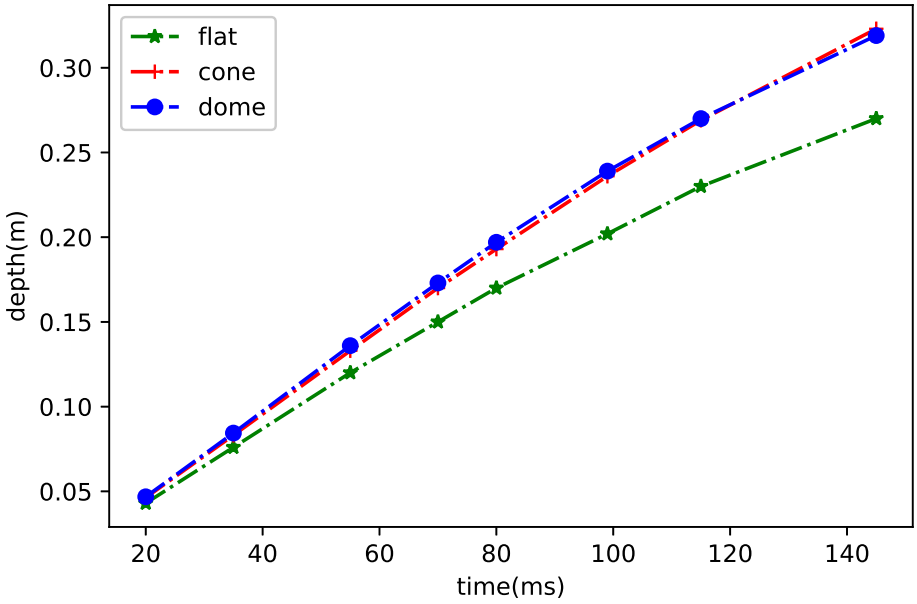


Figure 3.5. Penetration depths of cylinders with various head geometries.

1.34 and 2.68 $m/s$, while keeping all other parameters unchanged. As the horizontal velocity increases, more energy is transferred to the water upon impact at the fore end, which results in more air trapped on the downstream side. The air entrapment processes with snapshots at various time instants are shown in Fig. 3.6. It can be observed that more air is trapped with a larger horizontal velocity, which results in a larger air channel while generating more splashes above the water surface.

As the diving process continues, the air channel is gradually stretched and eventually detached from the cylinder surface. The separation of the air channel from the cylinder side occurs sooner for cylinder with higher horizontal velocity. Before the cylinder fully submerges, the rear end of the cylinder with the larger horizontal velocity travels a longer horizontal distance. With a larger horizontal velocity, a greater torque is generated by the velocity difference of the two ends, which results in a larger inclination angle while stretching the air channel even more. As shown in

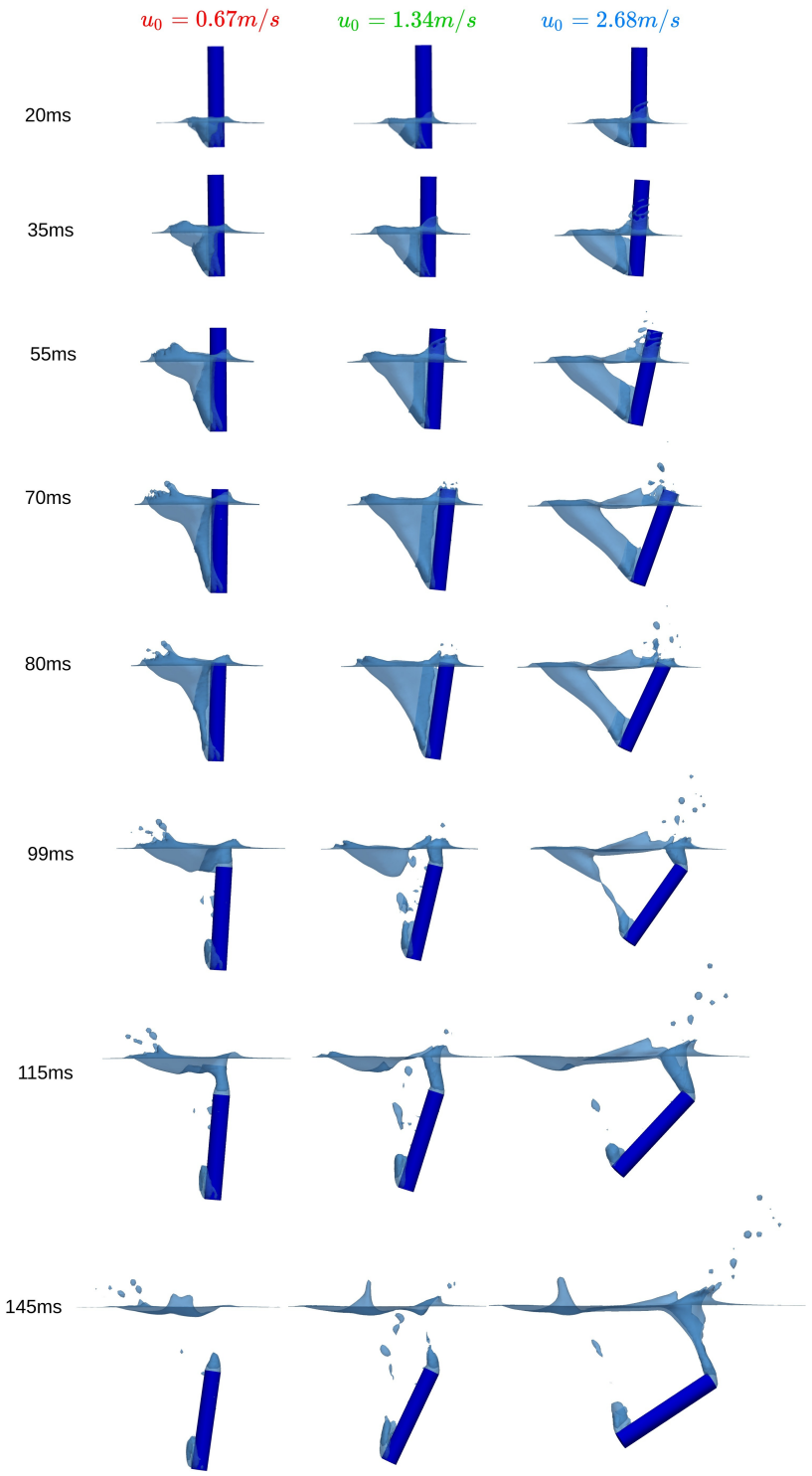


Figure 3.6. Trajectories and air entrapment of cylinders with various entry velocities.

Figs. 3.6 and 3.7, the larger horizontal velocity results in the larger rotation. As the entry process continues, the vertical projected area decreases alongside the rotation, which leads to a smaller horizontal resistance and results in a larger inclination. Also, cylinder with smaller horizontal velocity penetrates faster during the diving

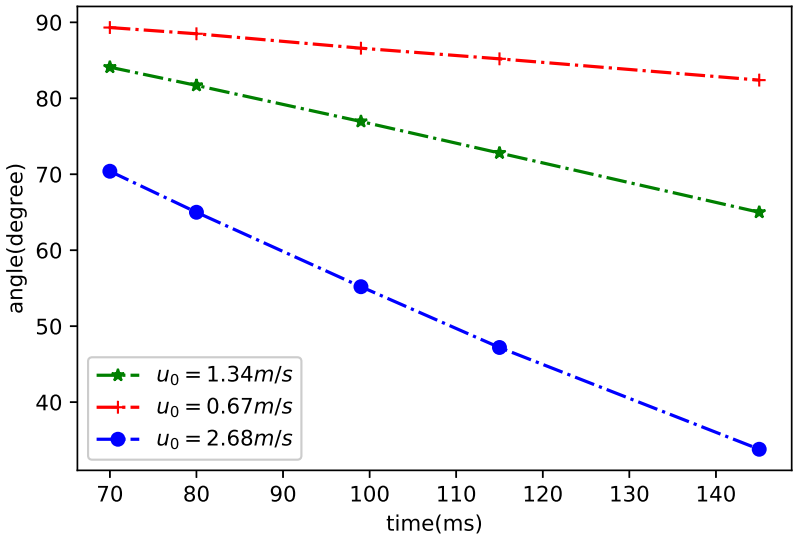


Figure 3.7. Cylinder inclination angles with various horizontal velocities.

process. The smaller horizontal velocity, the smaller the rotation. Thus, the vertical resistance decreases as the horizontal projected area gets smaller for cylinder with a smaller horizontal velocity. As a consequence, the penetration of cylinder with a larger horizontal velocity suffers a larger water resistance which results in a flatter curve shown in Fig. 3.8. It should be noted that the penetration depth depends on the combination of the traveling velocity and the inclination during the whole diving process.

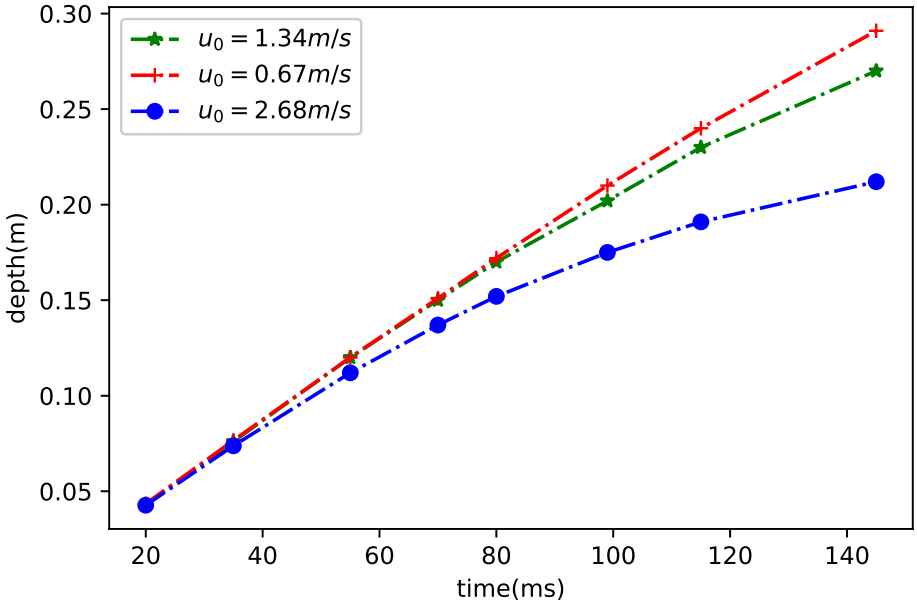


Figure 3.8. Penetration depths of cylinders with various horizontal velocities.

## 3.3 Entry Inclined Angle

In general, solid objects do not enter the water vertically all the time. It is of great interest to study the entry problem with an initial inclination. The effect of the entry inclination during the water entry process has been investigated by changing the inclined angle at inlet while keeping all other parameters unchanged. The water entry processes with $\alpha = 90.5^o$ (reference case), $\alpha = 80^o$ and $\alpha = 100^o$ are shown in Fig. 3.9. It shows that less air has been trapped by the cylinder with $\alpha = 100^o$ and the air channel formed by the cylinder with $\alpha = 80^o$ breaks sooner than the other two cases.

The results of penetration depths versus transport time are shown in Fig. 3.10 and it has been found that cylinder with a smaller entry inclined angle does not travel as deep as the other two cases. When the entry inclined angle is smaller than $90^o$

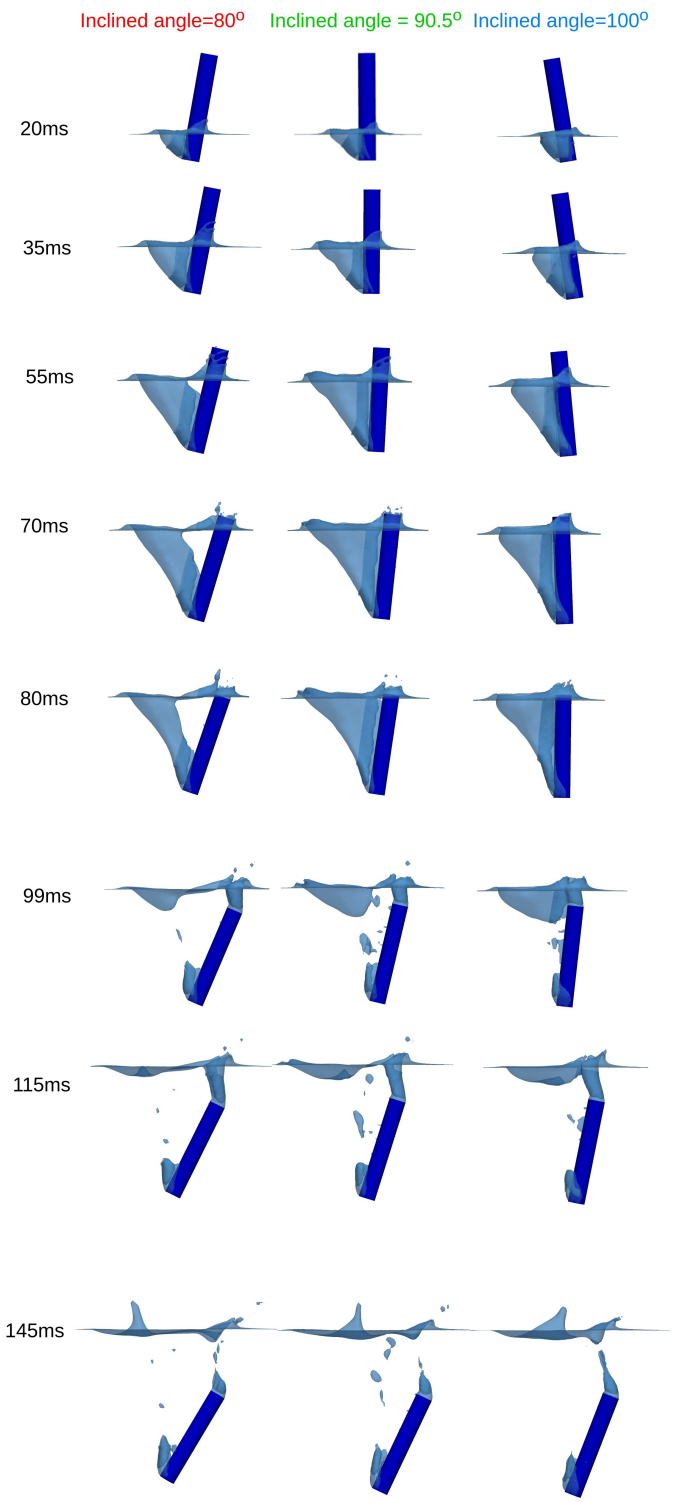


Figure 3.9. Trajectories and air entrapment of cylinders with various initial inclination.

(rear end tilts towards the traveling direction), the horizontal projected area increases as cylinder penetrates deeper which results in a larger vertical resistance (Fig. 3.10). Meanwhile, with the larger vertical resistance exerted on the cylinder, the velocity difference between the cylinder two ends increases which leads to a greater torque and a larger inclination. Therefore, the penetration depth is not only related to the initial impact velocity, but also depends on the vertical projected area during the entry process. It can be observed that cylinder with $\alpha = 100^o$ penetrates slighter faster than cylinder with $\alpha = 90.5^o$. When the entry inclined angle is larger than $90^o$ (cylinder rear end towards the downstream side), the horizontal projected area decreases which results in a smaller vertical resistance. As the cylinder penetrates deeper, the horizontal projected area decreases to zero. After the inclined angle gets smaller than $90^o$ alongside with the forward movement of the cylinder, the horizontal projected area increases which results in a larger vertical resistance. It can be seen that the horizontal projected area is affected by both the initial inclination and the traveling speed in which the inclination and traveling velocities are influenced by each other due to the projected area and corresponding resistance.

As shown in Fig. 3.11, the net rotation of cylinder with $\alpha = 100^o$ is larger than the other two cases. The larger vertical projected area, the larger the horizontal resistance. Before the cylinder fully submerges, the vertical projected area of cylinder with $\alpha = 100^o$ increases as the cylinder penetrates deeper in which a larger horizontal resistance is exerted on the cylinder. Thus, the velocity difference between the two ends increases and leads to a larger rotation.

As a consequence, it has been discovered that cylinder with a smaller entry inclined angle ($\alpha < 90^o$) does not travel as fast as the ones with larger initial inclinations.

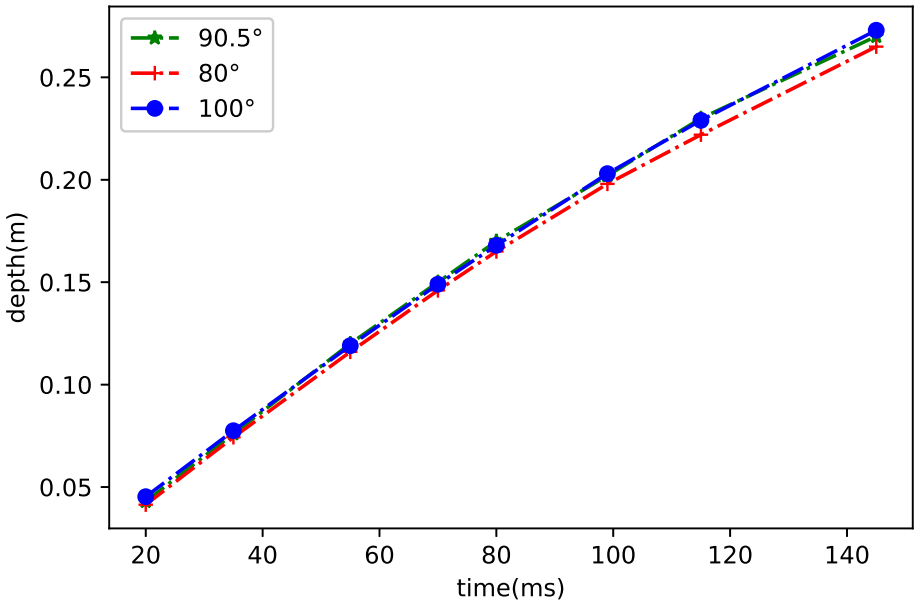


Figure 3.10. Penetration depths of cylinders with various entry inclined angles.

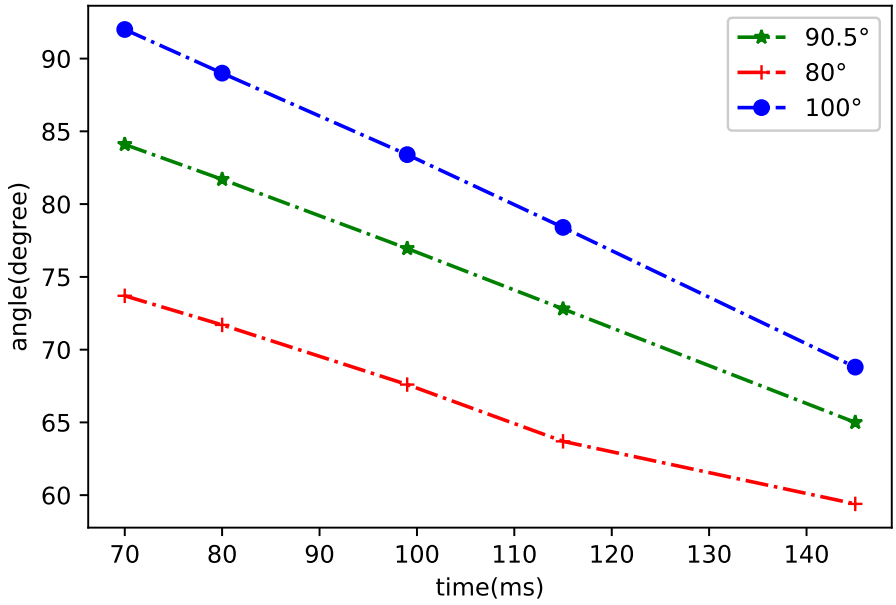


Figure 3.11. Cylinder inclined angle with various initial entry inclinations.

## 3.4 Liquid Density

The liquid density is expected to affect the apparent mass and the buoyancy force. As indicated in the experiment, the water tank is large enough thus the resistance from the tank wall can be ignored. The diving processes carried out with three liquids ($\rho = 499.1\ kg/m^3$, $\rho = 998.2\ kg/m^3$ and $\rho = 1996.4\ kg/m^3$) have been investigated in the present study. The air entrapment and trajectories at various time instants are shown in Fig. 3.12. It can be observed that less air is trapped in the heavier fluid and the air channel also breaks sooner in the heavier fluid. The larger density, the larger the apparent mass [76]. As shown in Figs. 3.12 and 3.13, the cylinder in the heavier fluid rotates more. Before the cylinder fully submerges, the fore end of the cylinder is being held on by the liquid and the rear end goes further which results in a larger rotation. The larger horizontal projected area leads to the larger vertical resistance resulting in a slower penetration. Additionally, the heavier liquid offers the larger buoyancy force which slows down the penetration. In Figs. 3.13 and 3.14, it can be seen that the penetration depth and the net rotation depend on the combination of the traveling velocity and the inclination during the diving process. The larger horizontal inclination leads to a larger vertical resistance which slows down the penetration. The greater inertia of the heavier liquid, the larger the net rotation of the cylinder. In conclusion, the larger apparent mass and buoyancy force result in more horizontal inclined orientation which leads to larger vertical resistance and slower penetration. Thus, the cylinder in a heavier fluid does not travel as fast as the other cases do as shown in Fig. 3.14.

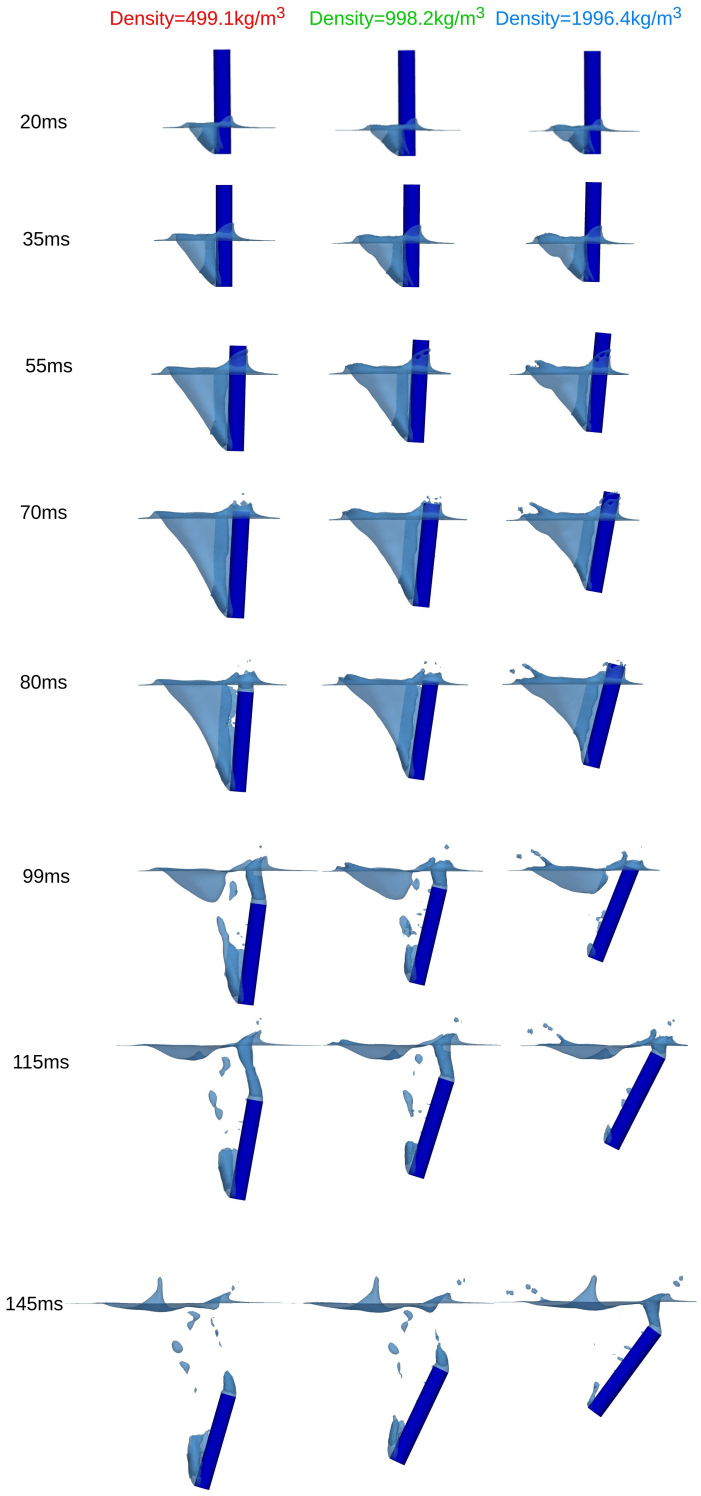


Figure 3.12. Trajectories and air entrapment of cylinders penetrating in liquids with various densities.

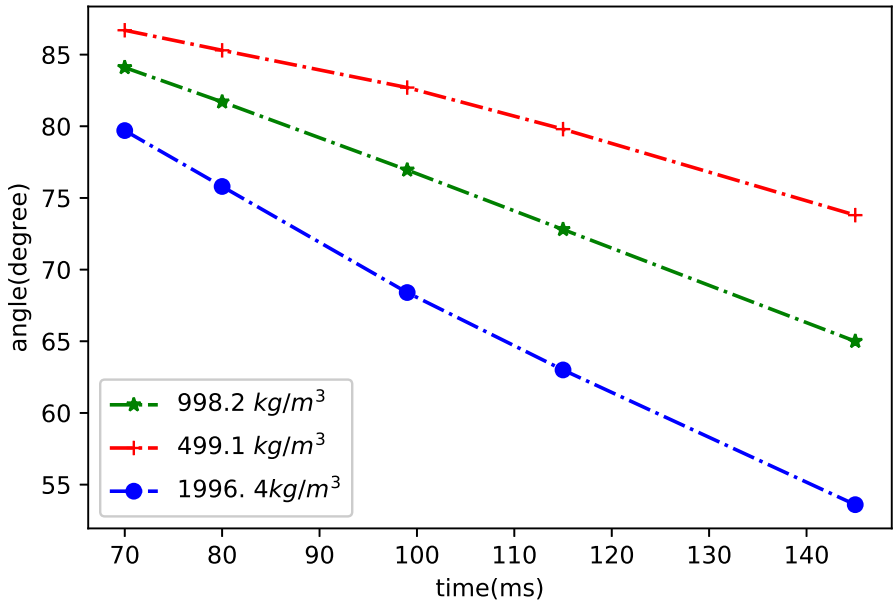


Figure 3.13. Cylinder inclination angle in liquids with various densities.

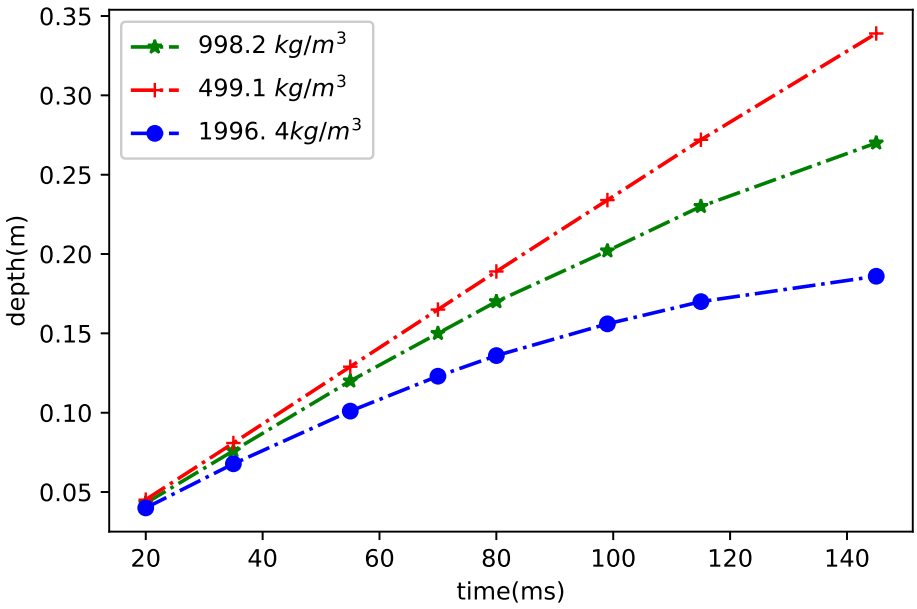


Figure 3.14. Penetration depths of cylinders in liquids with various densities.

## 3.5 Liquid Viscosity

Three liquids that only differ in kinematic viscosity ($\nu = 2 \times 10^{-6}$, $1 \times 10^{-6}$ and $5 \times 10^{-7} m^2/s$) while keeping all other parameters unchanged have been conducted to evaluate the effect of liquid viscosity. It should be noted that liquid with $\nu = 1 \times 10^{-6} m^2/s$ is the reference case. The water entry process at various time instants are shown in Fig. 3.15, which shows that the air entrapment and trajectories are minimally affected by the variation of viscosity. The cylinder inclinations and penetration depths at various time instants are shown in Figs. 3.16 and 3.17, which provides some information and validates the discussion above.

## 3.6 Surface Wetness

As mentioned previously, the water entry phenomenon is significantly influenced by the surface condition of the solid object. The wetting characteristics of a solid material is often modeled by the Young's equation [77] in which the relation between the equilibrium contact angle $\theta_c$ and the surface tension at the three-phase contact line is given by:

$$\sigma_{SG} = \sigma_{SL} + \sigma_{LG} cos\theta_c, \tag{3.1}$$

where subscripts SG, SL and LG denote solid-gas, solid-liquid and liquid-gas interfaces, respectively (see Fig. 3.18).

In general, surface with contact angle smaller than $90^o$ is considered as hydrophilic, while larger than $90^o$ is considered as hydrophobic. The wettablitity of the cylinder surface is expected to affect the detachment of air channel as well as the formation of cavity [71]. In the work of Duez *et al* [71], it has been discovered that an air cavity is formed by a sphere during the entry process that only occurs when the impact velocity is above a threshold velocity. Details of the calculation for the

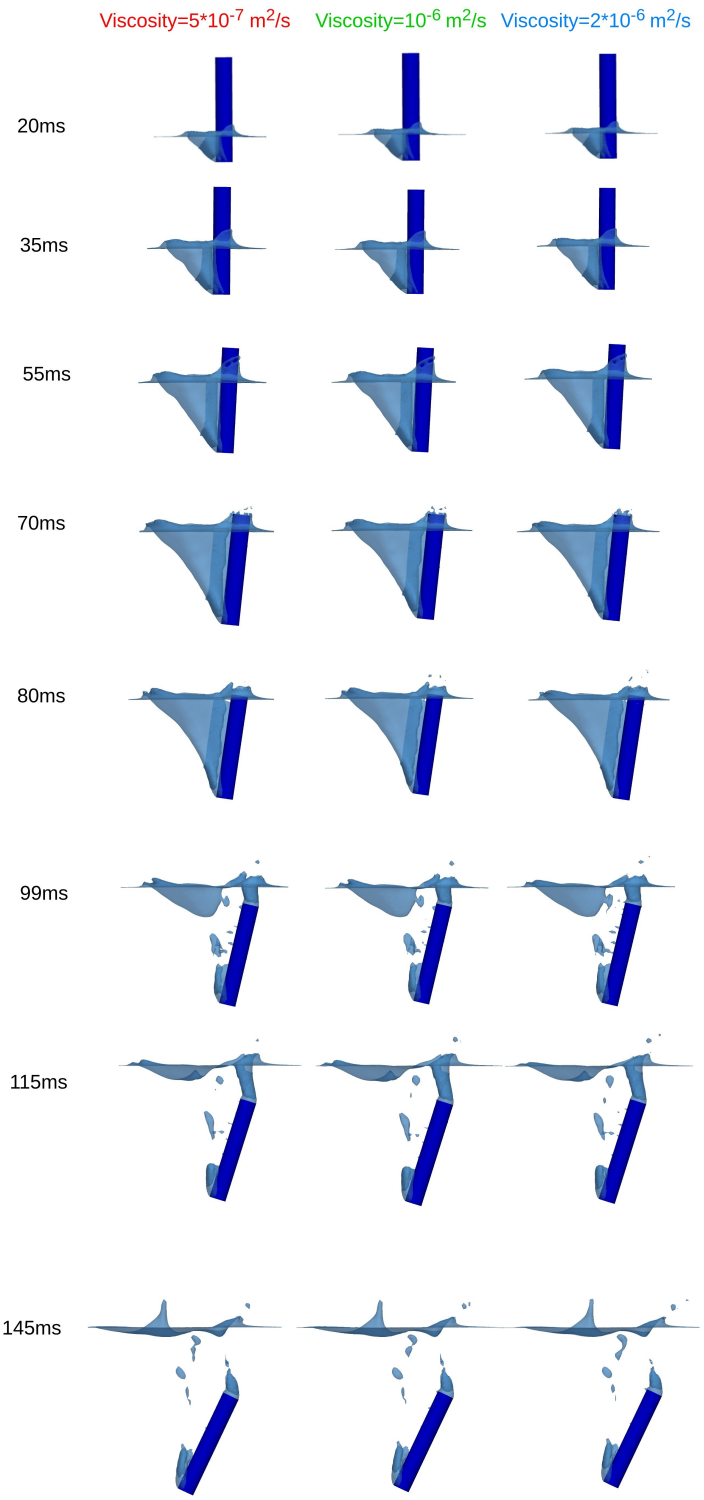


Figure 3.15. Trajectories and air entrapment of cylinders with various liquid viscosities.

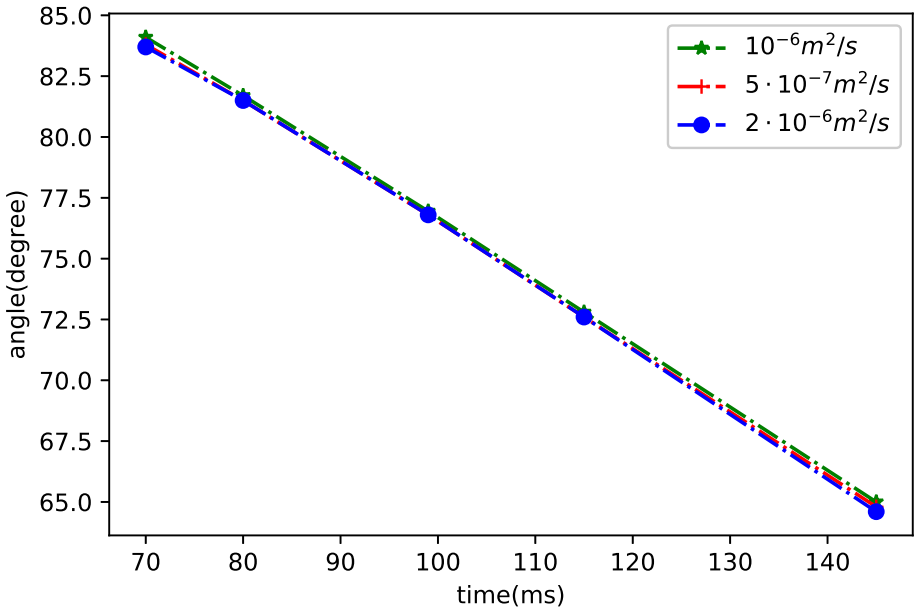


Figure 3.16. Cylinder inclination angle with various liquid viscosity.

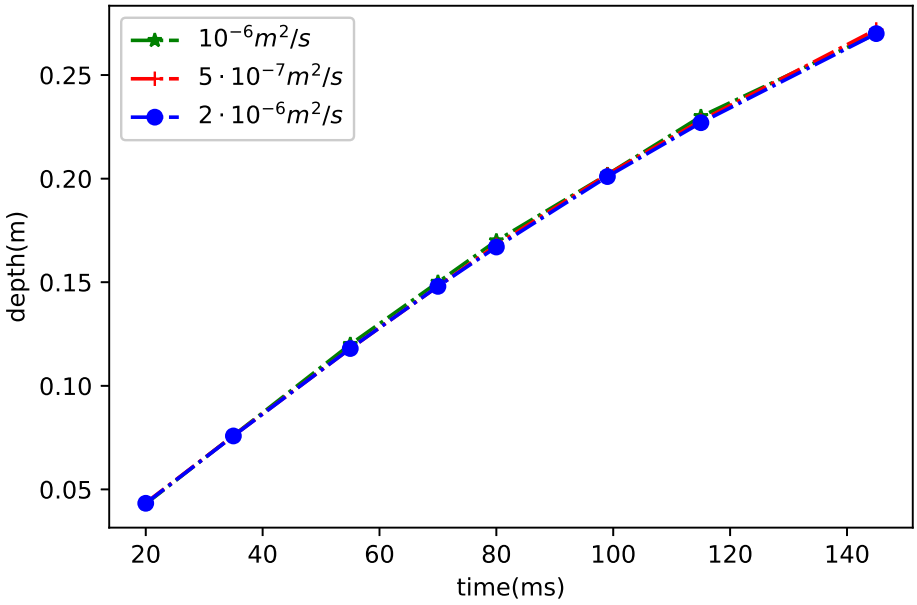


Figure 3.17. Penetration depths of cylinders with various liquid viscosity.

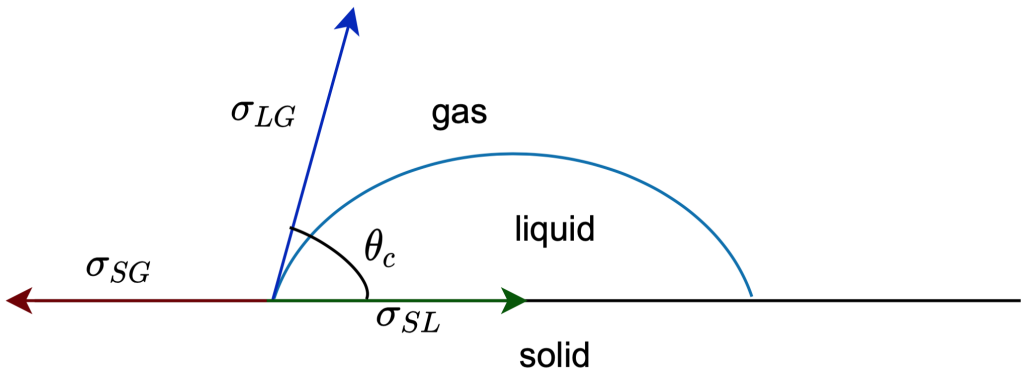


Figure 3.18. Illustration of contact angle.

threshold velocity can be found in their paper in which the impact velocity in the present study is not as large as the threshold velocity and thus an air cavity is not expected to appear. Surface wetness can be described by the contact angle between liquid and solid. The static contact angle is formed at the contact line, the dynamic contact angle provides information about contact angle hysteresis with advancing and receding angles describing the movement. Due to lack of values of the advancing and receding angles, surface wetness has been modified varying the static contact angle at the cylinder surface without considering the hysteresis in which contact angles are set as $90^o$, $20^o$, and $150^o$ for reference, hydrophilic and hydrophobic surfaces, respectively. As shown in Fig. 3.19, the air entrapment and trajectories of cylinder with various wettabilities at key time instants are presented, which shows that the detachment of the air channel occurs sooner with a hydrophilic surface but with less smashed bubbles generated at the same time. Since the surface is hydrophilic, trapped air is easier to leave the cylinder side which results in an earlier detachment. On the other hand, more air bubbles are generated during the entire diving process with a hydrophobic surface since the low wettability of the cylinder leads to more water films to capture

the trapped air. A machined aluminium cylinder is employed in the experiment in which aluminium is naturally hydrophilic.

It can be observed in Fig. 3.19 that the air entrapment is in better agreement with the experimental result for the hydrophilic case than the reference case which supports the discussion. The cylinder inclinations and penetration depths of cylinder with various surface wettness are shown in Figs. 3.20 and 3.21. The surface condition plays an insignificant role in the overall diving trajectories and it only affects the air entrapment slightly during the entry process.

## 3.7 Surface Tension

The surface tension results from unbalanced molecular cohesive forces between two phases at the interface and it is an important factor in the phenomenon of capillarity [78]. Therefore, the surface tension effect always plays an important role in small-scale liquid simulations. The surface tension $F_s$ is modelled as continuum surface force (CSF) [79]. It is calculated as follows:

$$\boldsymbol{F_s} = \sigma\kappa\nabla F, \tag{3.2}$$

where $\sigma$ is the surface tension constant, $\kappa$ the curvature, and $F$ the volume fraction of liquid. The curvature can be approximated by [80]:

$$\kappa = -\nabla \cdot \boldsymbol{n}. \tag{3.3}$$

A large-scale fluid model has been applied in the present study and the surface tension is expected to have minimal effects on the water entry process. As shown in Fig. 3.22, the diving process has been carried out with various liquid surface tensions (0.036 $N/m$, 0.072 $N/m$ and 0.144 $N/m$) and the surface tension plays a minor role in the air entrapment and trajectories as expected. The cylinder inclinations and

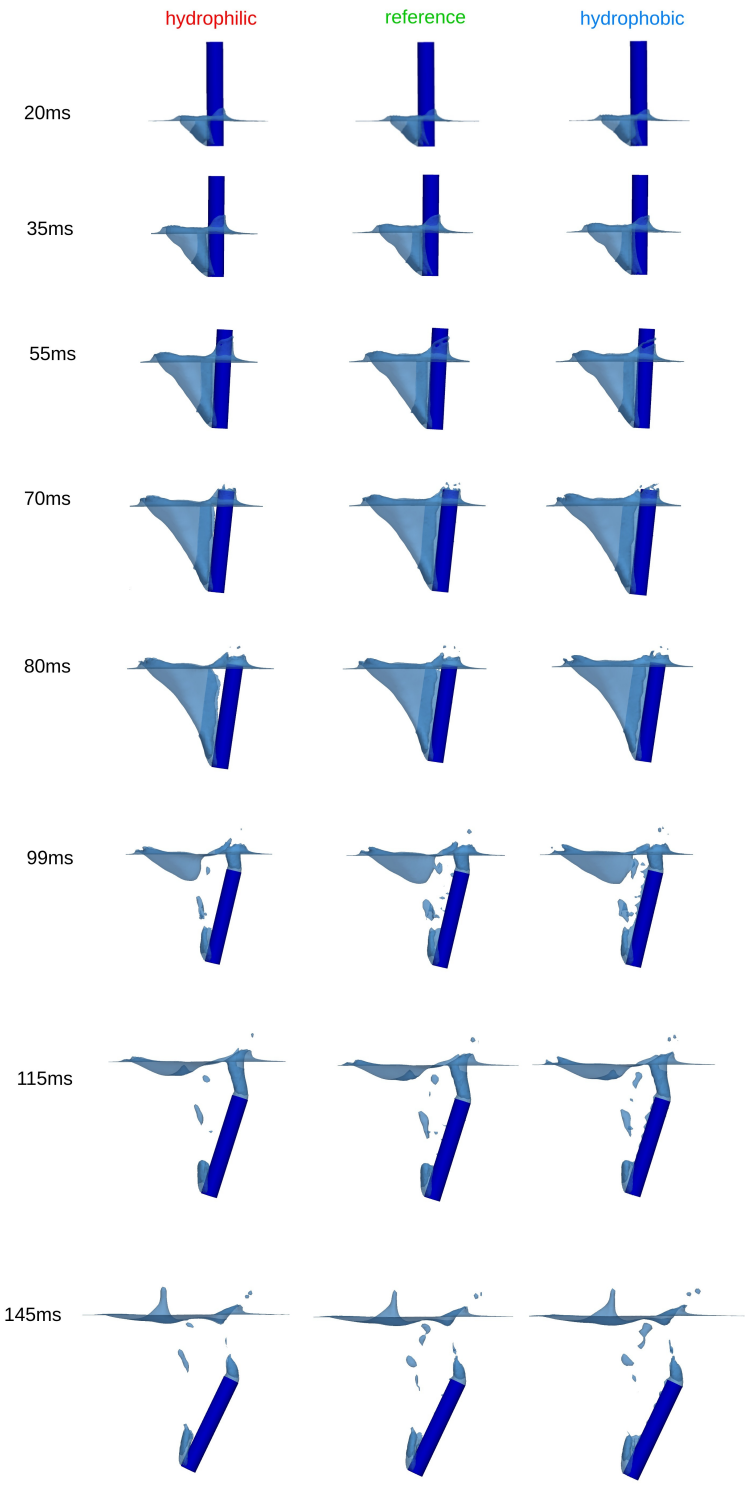


Figure 3.19. Trajectories and air entrapment of cylinders with various surface wettabilities.

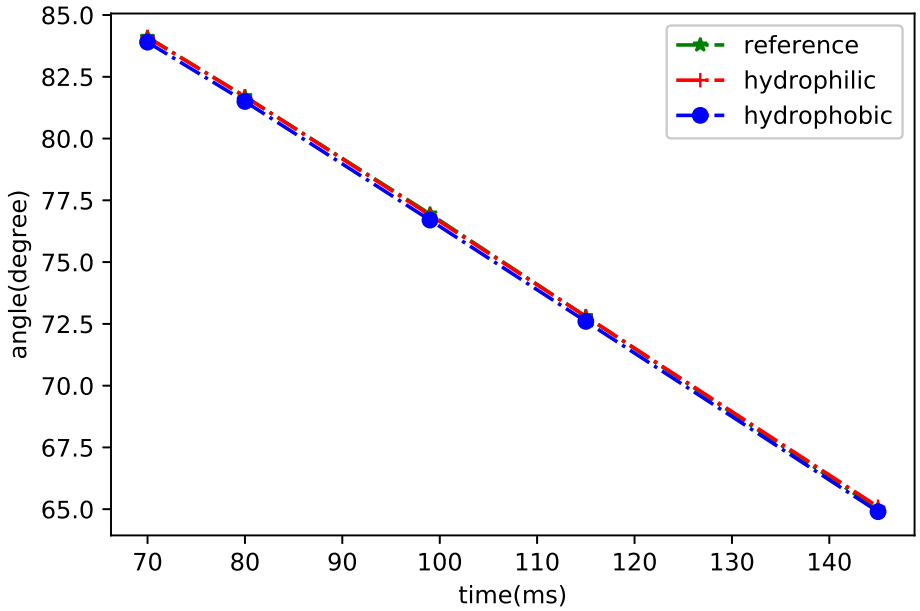


Figure 3.20. Cylinder inclination angle with various surface wettabilities.

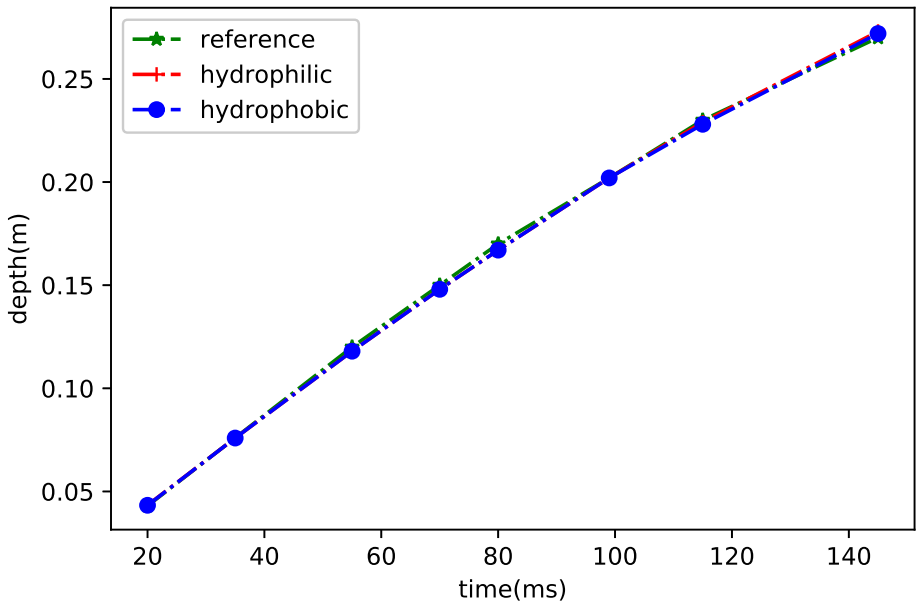


Figure 3.21. Penetration depths of cylinder with various surface wettabilities.

penetration depths at various time instants are shown in Figs. 3.23 and 3.24, which provides vital information of the entry process and validates the discussion above.

## 3.8 Cylinder Density

The density of the cylinder is expected to affect the air entrapment and trajectories during the water entry process. The effect of the cylinder density on the transport process has been studied. The captured air entrapment with cylinder densities of 639.5 $kg/m^3$, 1279 $kg/m^3$ (reference case) and 2558 $kg/m^3$ is shown in Fig. 3.25. It can be observed that the air channel breaks sooner for the cylinder with a smaller density. The smaller the cylinder density, the larger the resultant lift force.

Before the cylinder fully submerges in the water, the fore end of the cylinder slows down due to the vertical resistance. For cylinder with a smaller density, the velocity at the fore end decreases faster which results in a larger velocity difference between the fore end and the rear end. Therefore, a greater torque is generated which leads to a larger rotation. The larger rotation also results in a greater horizontal projected area which further slows down the penetration. As shown in Fig. 3.26, the cylinder with a smaller density rotates more. The results of penetration depths versus transport time are shown in Fig. 3.27 and it has been found that the cylinder with a larger density travels further due to the larger gravitational force. The velocity of the fore end of the cylinder does not decrease as fast as the one with a smaller density. Thus, a heavier cylinder penetrates faster.

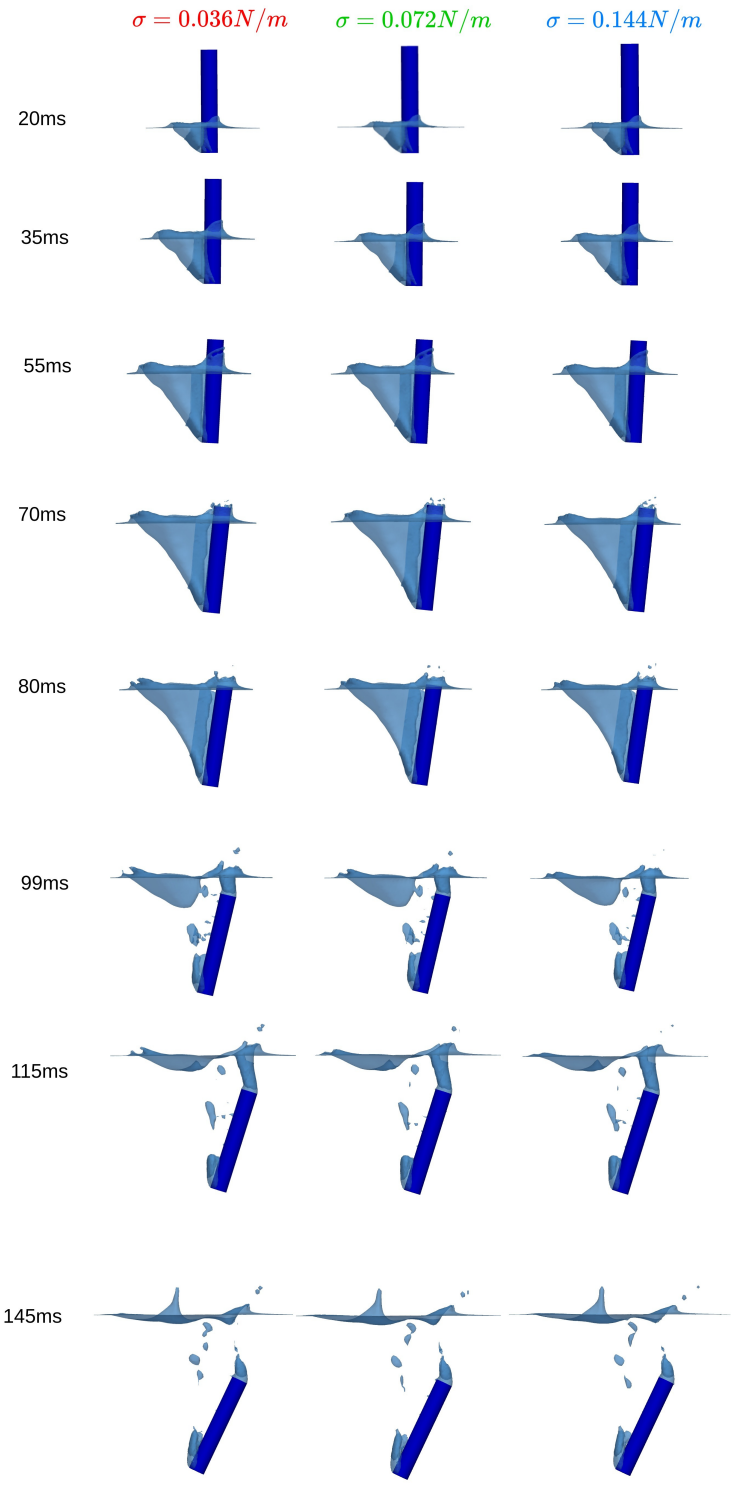


Figure 3.22. Trajectories and air entrapment of cylinders with various surface tensions.

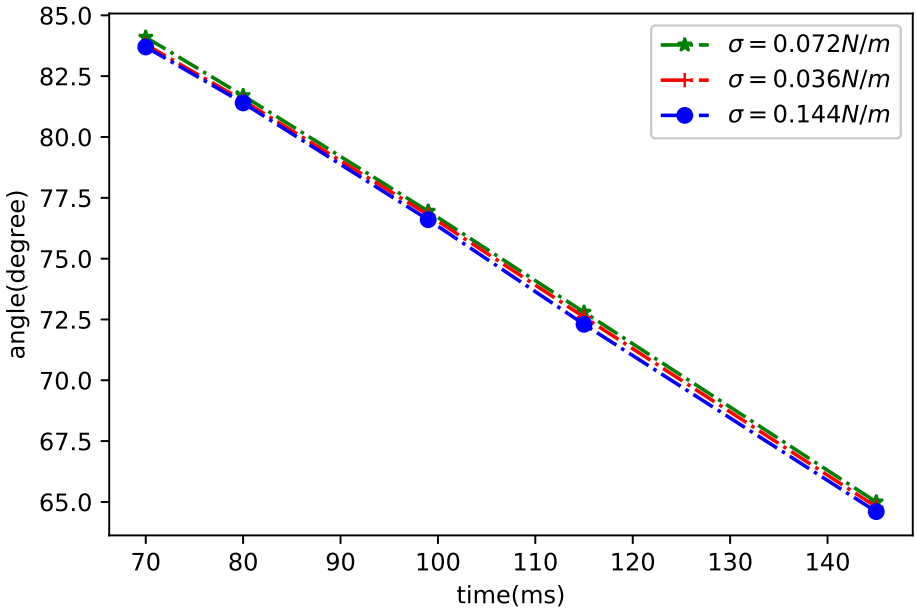


Figure 3.23. Cylinder inclination angle with various surface tensions.

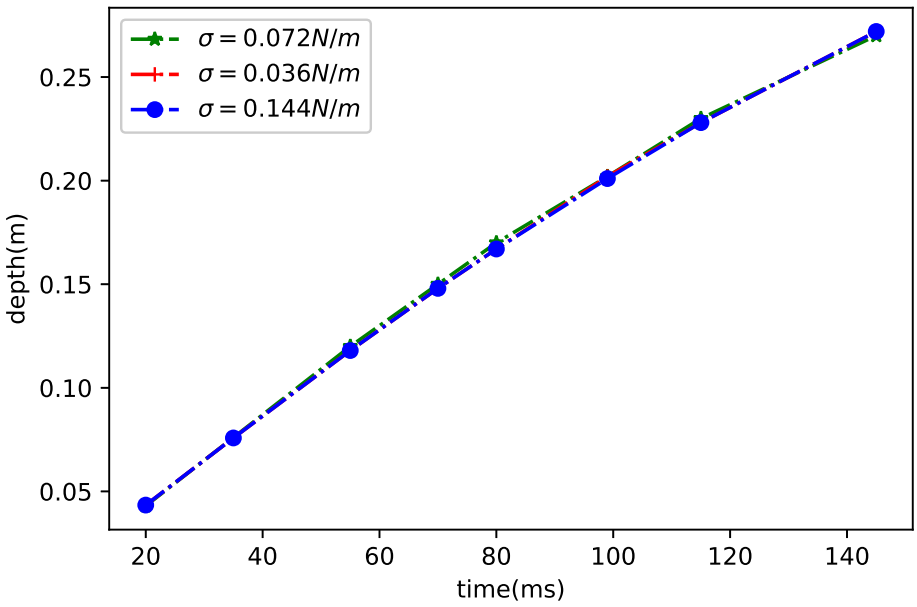


Figure 3.24. Penetration depths of cylinder with various surface tensions.

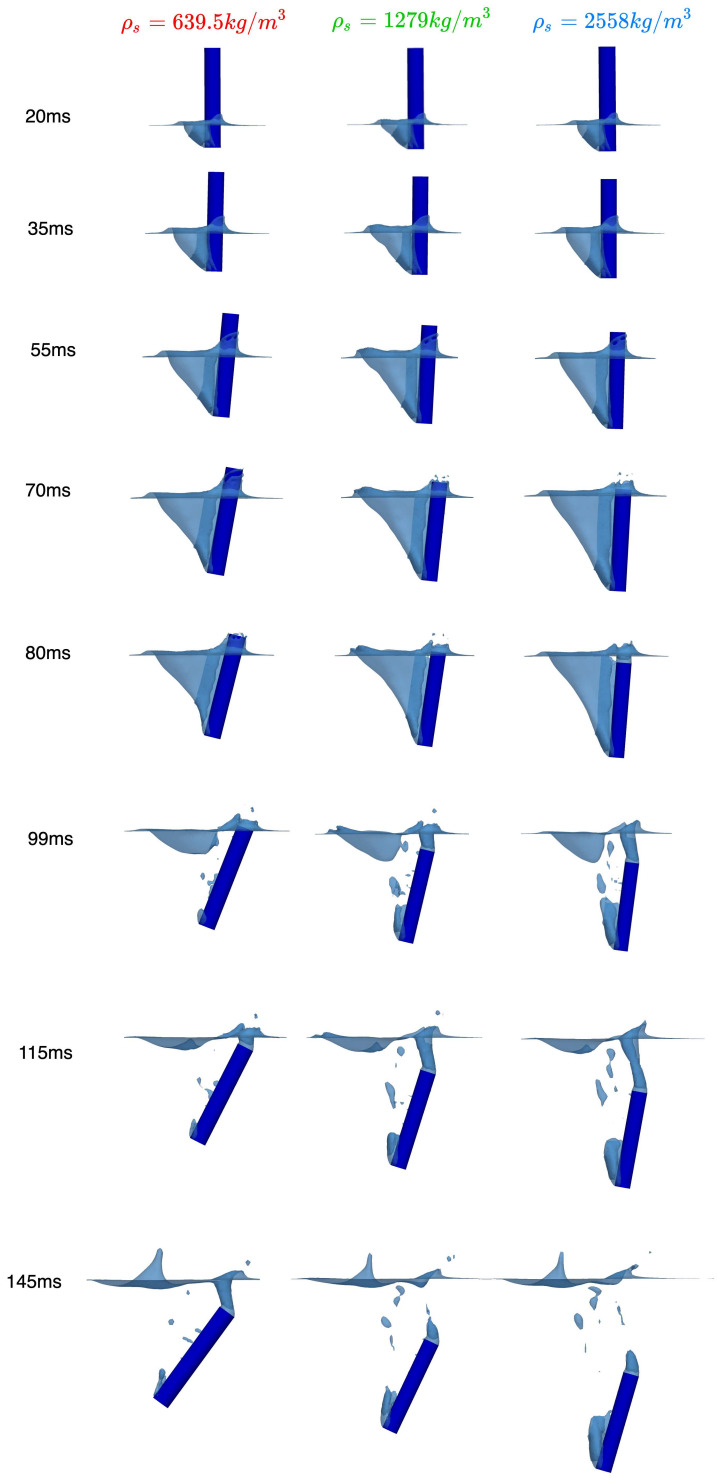


Figure 3.25. Trajectories and air entrapment in the diving process with various cylinder densities.

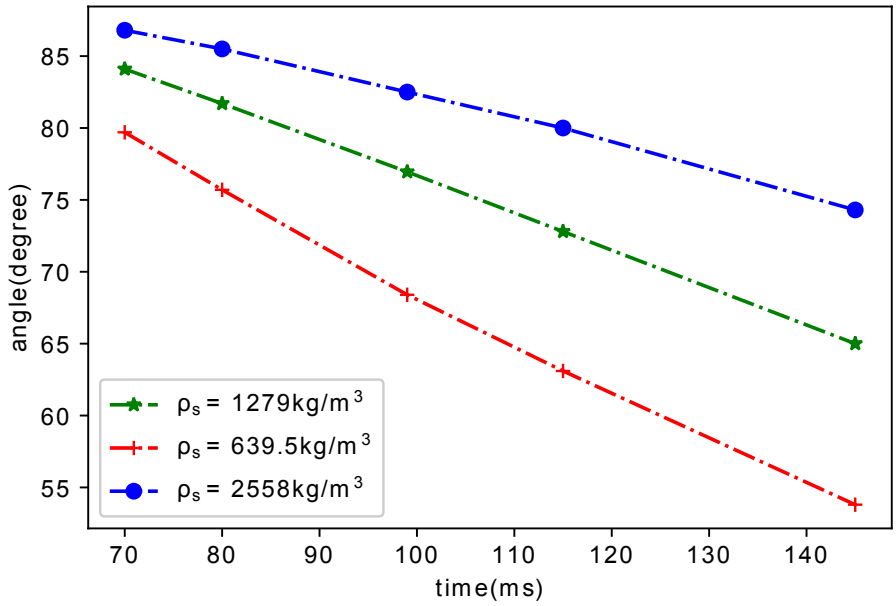


Figure 3.26. Cylinder inclination angle with various cylinder densities.

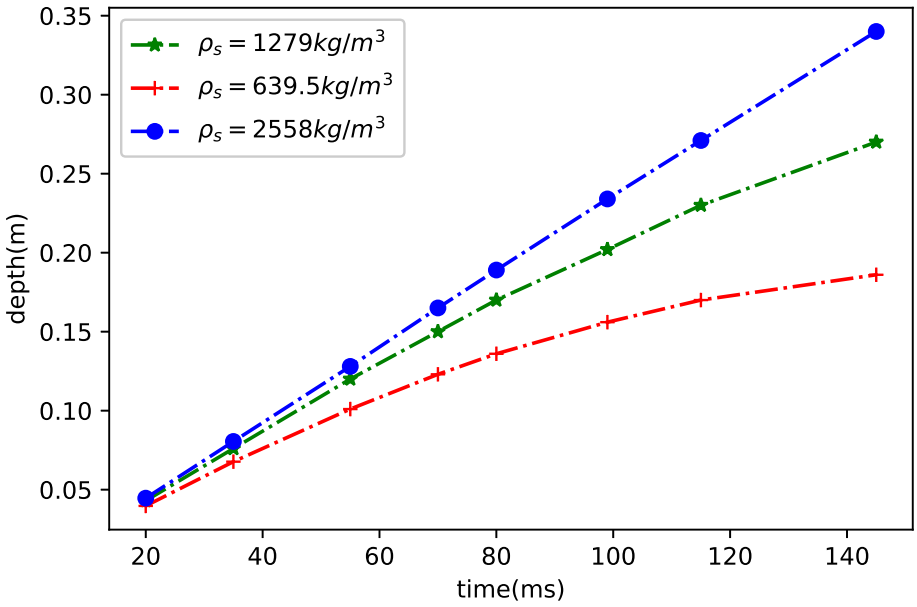


Figure 3.27. Penetration depths in the diving process with various cylinder densities.

Table 3.1. Parameters used in the current study

| **Parameter** | **Value** | | | **Unit** |
|---|---|---|---|---|
| head geometry | cone | flat | dome | |
| entry impact velocity | 0.67 | 1.34 | 2.68 | $m/s$ |
| entry inclined angle | 80 | 90.5 | 100 | degree |
| liquid density | 449.1 | 998.2 | 1996.4 | $kg/m^3$ |
| liquid kinematic viscosity | $5 \times 10^{-}7$ | $1 \times 10^{-}6$ | $2 \times 10^{-}6$ | $m^2/s$ |
| surface wetness | hydrophilic | reference (neutral) | hydrophobic | |
| surface tension | 0.036 | 0.072 | 0.144 | $N/m$ |
| cylinder density | 639.5 | 1279 | 2558 | $kg/m^3$ |

# CHAPTER 4

# GEOMETRIC INTERPOLATION SCHEME ON OVERSET MESHES

PLIC schemes have been extensively employed in the VOF method for interface capturing in numerical simulations of multiphase flows. Dynamic overset meshes have been widely used for problems with relative motions and complex geometric shapes. The strategy of overset meshes is to transfer flow variables within the overlapped region between the background and body meshes. The acceptor cell value is evaluated by a weighted average of its donors. The weighting factors are calculated by different algebraic methods, such as the averageValue, injection and inverseDistance schemes, which are implanted in the foam-extend library.

As discussed in Chapter 2, the dynamic overset mesh can be especially useful in applications involving components with relative motion [47]. The overset mesh can reduce the computation time compared with applying a deforming mesh method alone [48] and improve the simulation accuracy. The overset grid method, also known as Chimera grid embedding scheme, utilizes a set of overlapping grids to discretize a complex computational domain into a number of simpler grids [60]. The basic idea of the overset mesh is interpolating the flow fields over the overlap region of the meshes which represents the entire computational domain (background mesh) and the moving object (body mesh), respectively. The overset boundary cells of these two meshes are marked as acceptors where the flow variable values are interpolated from their donor cells. The governing equations will then be solved in the respective meshes. However, a difficulty of the overset mesh implantation in the PLIC-VOF method is the interpolation of the VOF field. Most of the overset interpolation schemes are

designed for continuous flow variables. The acceptor value is evaluated by using a weighted average of the ones of its donors. The weighting factors are obtained by using different algebraic methods [52]. Unlike the continuous flow variables, the VOF field is a step function near the interfaces, which varies from zero to unity rapidly. Thus a specialized overset interpolation scheme is needed for the PLIC-VOF method to transfer the fraction field between the meshes precisely.

In this chapter, a geometric interpolation scheme of the VOF field in overset meshes for the PLIC-VOF method is proposed based on the PLIC-VOF scheme developed by Dai and Tong [44, 45]. The VOF value of an acceptor cell is evaluated geometrically with the reconstructed interfaces from the corresponding donor elements.

## 4.1 Algebraic Interpolation Schemes

In the algebraic interpolation schemes, the volume fraction value $F$ in an acceptor cell is given by:

$$F_a = \sum_{i=1}^{N_d} w_i F_{d,i}, \tag{4.1}$$

where $F_a$ is the VOF value of the acceptor cell, $N_d$ the total number of the donor cells which overlap with the acceptor cell, $F_{d,i}$ the VOF value of the $i$th donor cell and $\omega_i$ the weighting factors. There are a few ways to calculate weighting factors [62].

### 4.1.1 Injection Method

In the `injection` scheme, the weighting factors are given by:

$$w_i = \begin{cases} 1, & \text{for the master donor,} \\ 0, & \text{otherwise,} \end{cases} \tag{4.2}$$

where the master donor is the donor the acceptor centroid falls in. The `injection` scheme is first order and bounded.

### 4.1.2 AverageValue Method

The acceptor volume fraction $F_a$ in the `averageValue` method is the arithmetic mean value of all the donor values. The weighting factors are uniform and given by:

$$w_i = \frac{1}{N_d}. \tag{4.3}$$

The `averageValue` scheme is also first order and bounded.

### 4.1.3 InverseDistance Method

In terms of the spatial locations of the acceptor and donors, the weighting factors in the `inverseDistance` method are evaluated as

$$w_i = \frac{\frac{1}{\|\vec{X}_a - \vec{X}_{d,i}\|}}{\sum_{i=1}^{N_d} \frac{1}{\|\vec{X}_a - \vec{X}_{d,i}\|}}, \tag{4.4}$$

where $\vec{X}$ is the cell center coordinates. The `inverseDistance` scheme is second order and bounded.

## 4.2 Geometric Interpolation Scheme

For the ease of explanation of the geometric interpolation scheme for the PLIC interface reconstruction method, a 2D polygonal overset mesh is used. As shown in Fig. 4.1, the body mesh (red) overlaps with the background mesh (blue). The acceptor cells (shaded elements) provide information in the overset boundaries when solving the governing equations in these two meshes.

The overset interpolation schemes are used to evaluate the values in the acceptor cells from the donor ones (see Fig. 4.2). It should be noted that the present study is based on the overset library in foam-extend 4.1 [52]. The acceptors/donors are

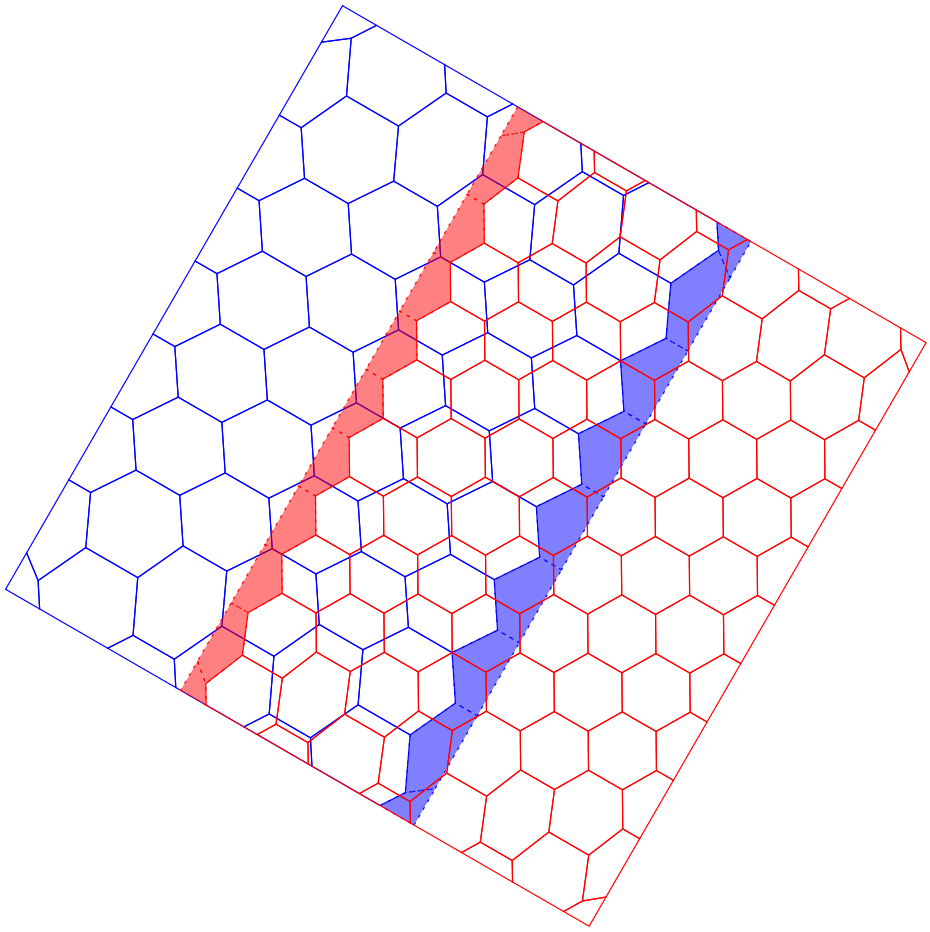

Figure 4.1. A 2D polygonal overset mesh.

found by using the `faceCells` algorithm which defines the acceptors to be the face cells of a given overset patch. The present study only focuses on the explicit fringe interpolation strategy that performs overset interpolation only once before solving the VOF equation. Three other built-in algebraic interpolation schemes are considered for accuracy comparisons.

As shown in Fig. 4.3, the donor cells may either contain interfaces, or be full of gas/liquid phases. In the mixed cell, the PLIC interface plane divides it into two distinct parts, $C^g$ and $C^l$, which are full of gas and liquid, respectively.

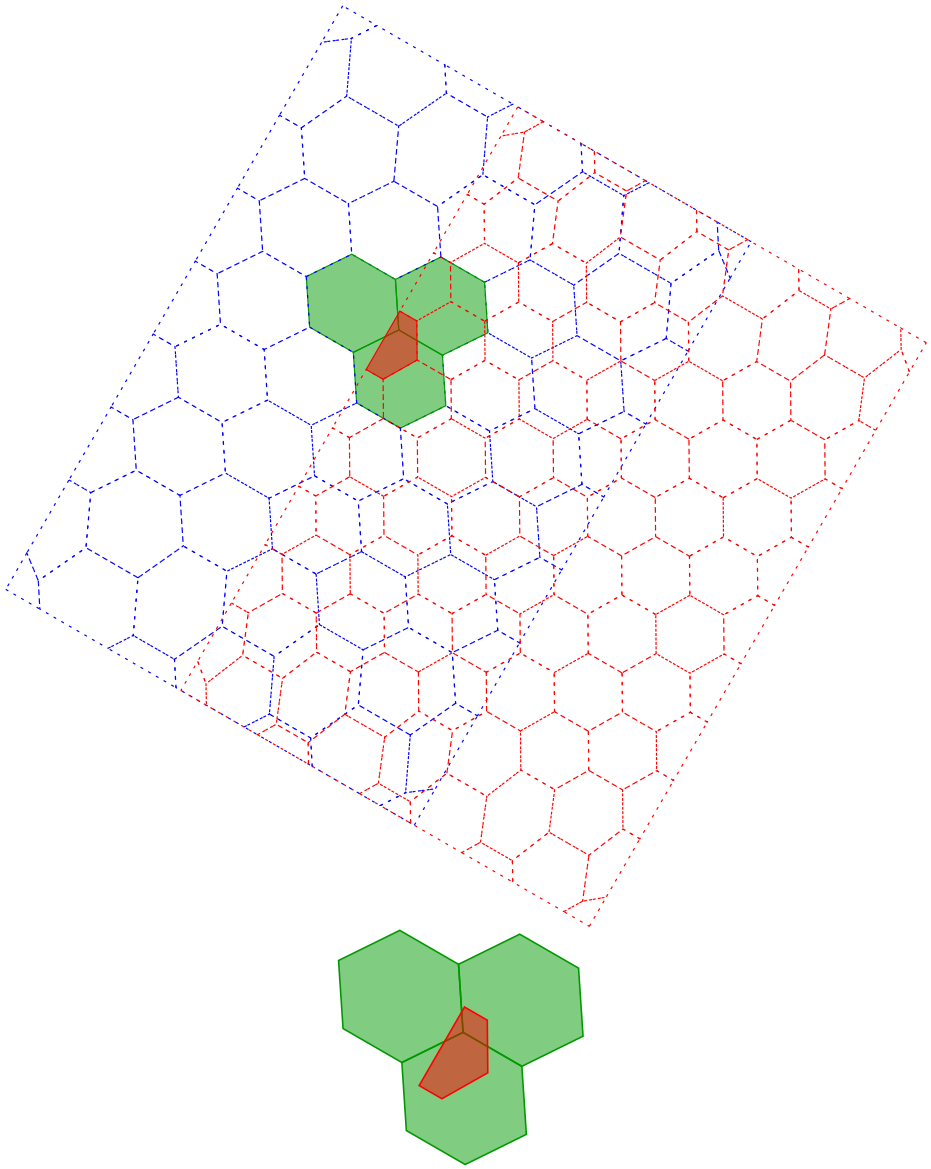

Figure 4.2. Donors of an acceptor cell.

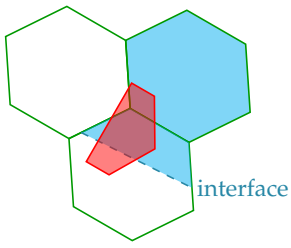


Figure 4.3. Donors of an acceptor cell with interfaces.

Unlike the algebraic interpolation scheme, the geometric one computes the acceptor volume fraction $F_a$ geometrically which is given by:

$$F_a = \frac{1}{\Omega_a} \sum_{i=1}^{N_d} C_a \cap C_{d,i}^l, \tag{4.5}$$

where $C_{d,i}^l$ is the liquid part shape of the donor cell $i$ and $\Omega_a$ and $C_a$ the acceptor volume and shape, respectively. Note that $C_{d,i}^l$ would be empty if the donor is full of gas. The geometric interpolation scheme computes the intersections between the acceptor and the liquid part of all donors and then normalizes their summation by the acceptor volume. The CGAL Boolean Library [81] is employed to compute the intersection of the two geometry shapes. Details of the algorithm follows.

A schematic diagram of the geometric interpolation scheme is shown in Fig. 4.4. For each pair of the acceptor $a$ and donor $d$, their intersection is first computed (see Fig. 4.4(a)), the overlapped region then is cut by using the interface plane in the donor cell (see Fig. 4.4(b)), finally the sub-part below the plane is $C_a \cap C_{d,i}^l$ (see Fig. 4.4(c)). It should be noted that the third step is unnecessary if the donor is full of liquid.

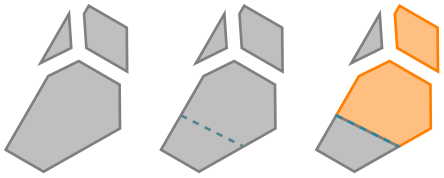

(a) Step 1 (b) Step 2 (c) Step 3

Figure 4.4. Geometric interpolation procedure.

# CHAPTER 5

# COMPARISONS OF GEOMETRIC INTERPOLATION SCHEME AND ALGEBRAIC INTERPOLATION SCHEMES

In this chapter, four testing cases on an unit square/cube are performed to demonstrate the accuracy of the proposed overset interpolation scheme by comparing it with three other algebraic ones. It should be noted that only quadrilateral and hexahedral meshes are employed in the present study and an extension to the general polygonal and polyhedral ones are currently ongoing.

## 5.1 Designed Numerical Tests

To test the performances of the various overset interpolation schemes, a dual-Pi and a dual-circle/sphere testing cases inside a unit square/cube with a prescribed rotational velocity field are employed for both 2D and 3D simulations. A schematic illustration of the dual-Pi test cases is shown in Fig. 5.1 with two liquid regions of a shape of $\pi$ located in the background and body meshes symmetrically. The dual-circle and dual-sphere cases replace the Pi shapes with circles and spheres, respectively. It should be noted that the liquid regions will be overlapped after half and one period. The time step is adjusted dynamically throughout the 2D and 3D simulations with the Courant number set to 0.5 to satisfy the CFL stability criterion. The numerical simulations are carried out with three different mesh sizes for each testing case.

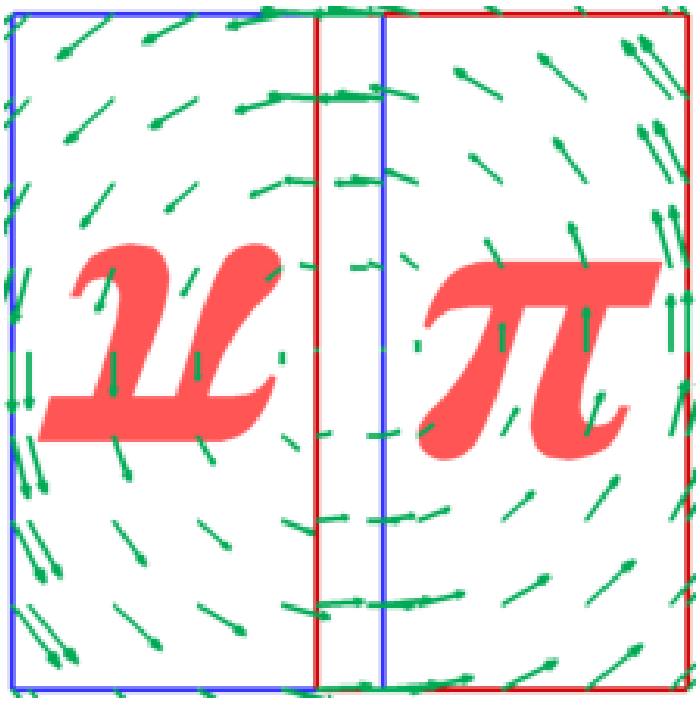

(a) 2D

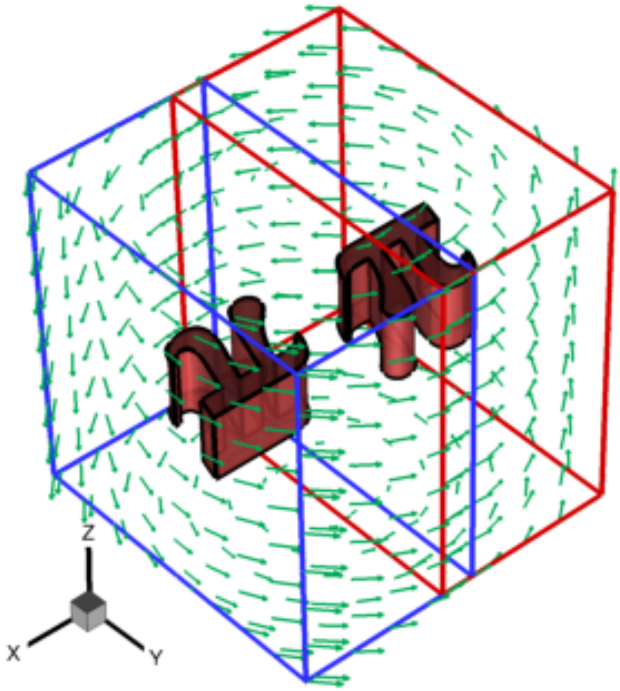


(b) 3D

Figure 5.1. Dual-Pi in an overset mesh.

With mass well conserved in both algebraic and geometric interpolation schemes, the shape error $E_s$ is used for the global accuracy of the various interpolation schemes with the equation given by:

$$E_s = \frac{\sum_{i=1}^{N_{cells}} |F_i^t - F_i^0| \, \Omega_i}{2 \sum_{i=1}^{N_{cells}} F_i^0 \Omega_i}, \tag{5.1}$$

where $F_i^t$ is the volume fraction value of cell $i$ at time $t$ and $F_i^0$ the initial value. The errors at $t = \frac{T}{2}$ and $t = T$ are evaluated and compared.

## 5.2 2D Cases

The comparisons of shape errors for 2D $\pi$ and 2D circle testing cases at $\frac{T}{2}$ and $T$ among the four interpolation schemes are shown in Fig. 5.2 and Fig. 5.3, respectively. In order to maintain the complex configuration of $\pi$, mesh size of $1/256$ $m$ has been used with interfaces presented in Fig. 5.2. Meanwhile, a coarser mesh with mesh size of $1/64$ $m$ has been employed to represent the circle shape with a reduction of computational time compared with the 2D $\pi$ case (see Fig. 5.3).

It can be observed that configurations of both $\pi$ and circle are preserved qualitatively well at $\frac{T}{2}$ by the four interpolation schemes with deformations of geometries increased after a full cycle. Quantitative comparisons of shape errors for 2D $\pi$ and 2D circle testing cases are shown in Fig. 5.4 and Fig. 5.5, respectively.

As shown in Fig. 5.4, the shape errors of the four schemes for 2D $\pi$ testing case are consistently getting smaller as the mesh size decreases. The finer the mesh, the higher the accuracy in maintaining interface shape obtained by the geometric scheme.

Three different mesh sizes of $1/16$, $1/32$ and $1/64$ $m$ have been employed in the dual-circle case to investigate the performances of the four interpolation schemes. Note that a higher accuracy in maintaining the interface sharp has been obtained by the geometric scheme with various mesh sizes.


(a) $t = \frac{T}{2}$


(b) $t = T$

Figure 5.2. Interface profiles with different interpolation schemes for 2D $\pi$ case with mesh size of $1/256$ $m$.

## 5.3 3D Cases

Comparisons of the interface profiles among the four interpolation schemes for 3D $\pi$ and sphere cases at $\frac{T}{2}$ and $T$ are shown in Fig. 5.6–5.9. The interface is represented as an iso-surface of 0.5 value of VOF field. It can be observed that there are some numerical diffusion in the simulation results. It should be noted that even though the diffusion can not be avoided at this moment, it has been considered in the shape error $E_s$.

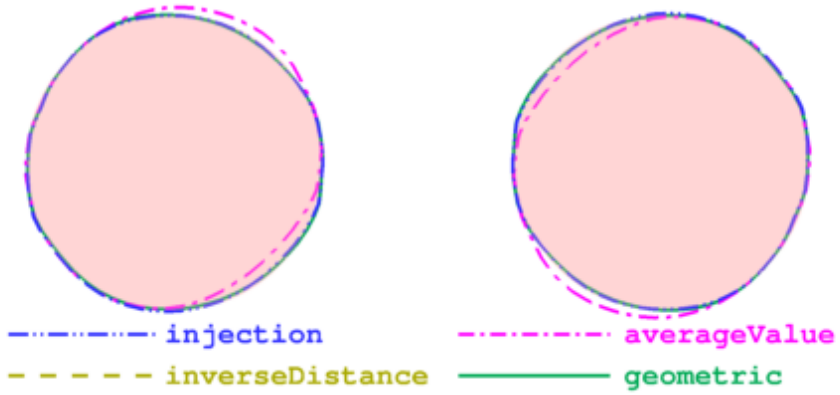


(a) $t = \frac{T}{2}$

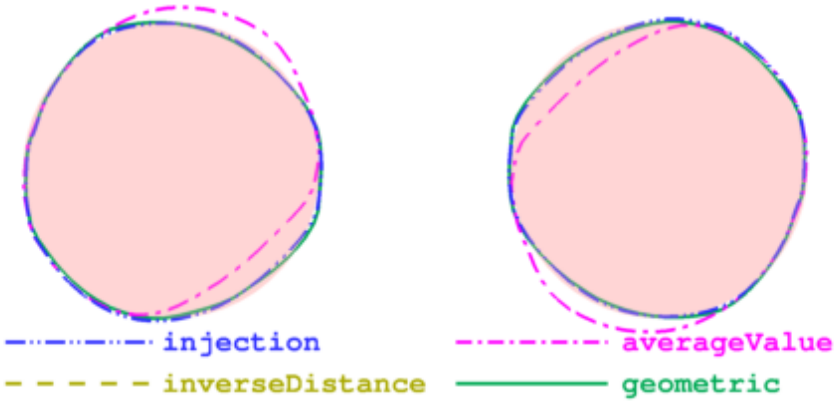


(b) $t = T$

Figure 5.3. Interface profiles with different interpolation schemes for 2D circle case with mesh size of 1/64 $m$.

The shape errors for 3D $\pi$ and sphere cases are shown in Fig. 5.10 and Fig. 5.11, respectively. A consistent improvement of the performance of the geometric scheme is achieved as the mesh size decreases. As shown in Fig. 5.11(b), the shape error of `injection` method at mesh size of 1/32 $m$ is larger than that of mesh size of 1/16 $m$. It should be noted that for `injection` method, the weighting factors are dominated by the master donor cells. This estimation will lose information from other donor cells in which it may result in a larger error for calculating the VOF values of acceptor cells. The main focus of this paper is on the performance of the proposed

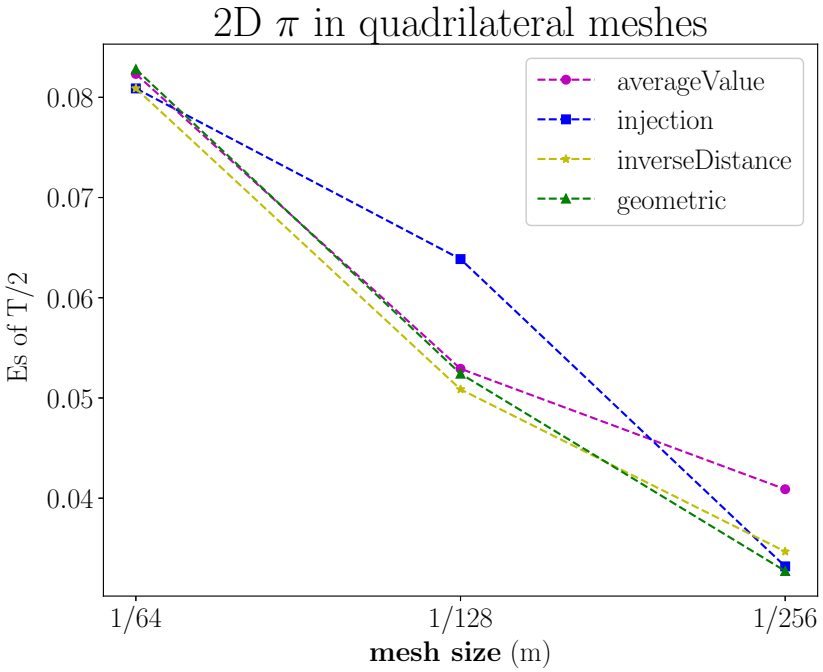


(a) $E_s$ at $t = \frac{T}{2}$

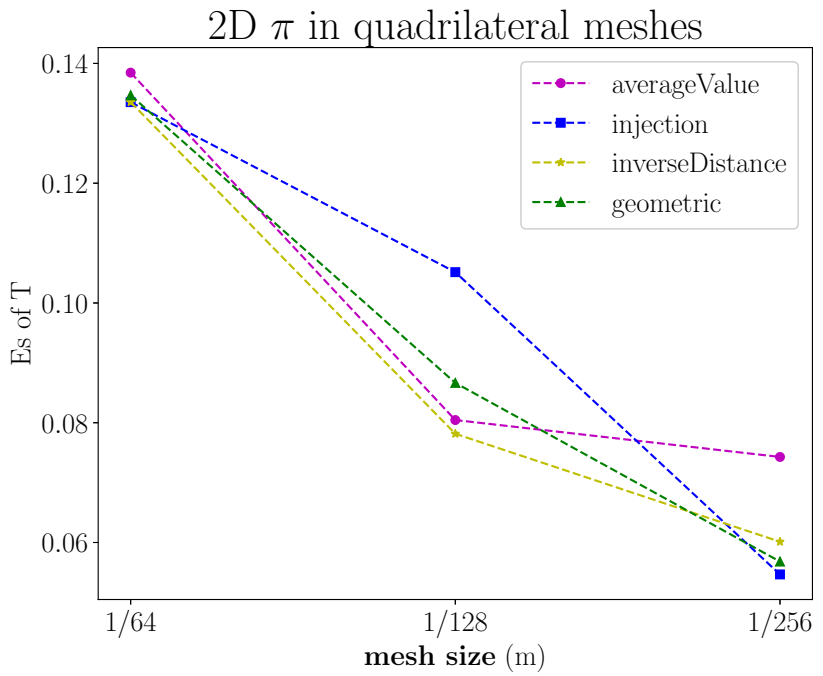


(b) $E_s$ at $t = T$

Figure 5.4. Shape error $E_s$ at half period $t = \frac{T}{2}$ and one period $t = T$ for 2D simulations with initial shape of $\pi$.

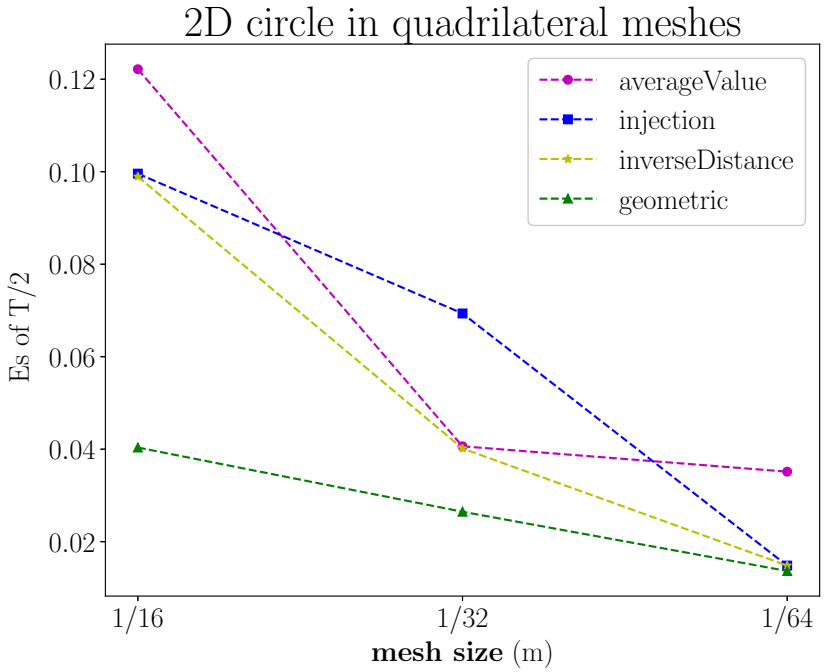


(a) $E_s$ at $t = \frac{T}{2}$

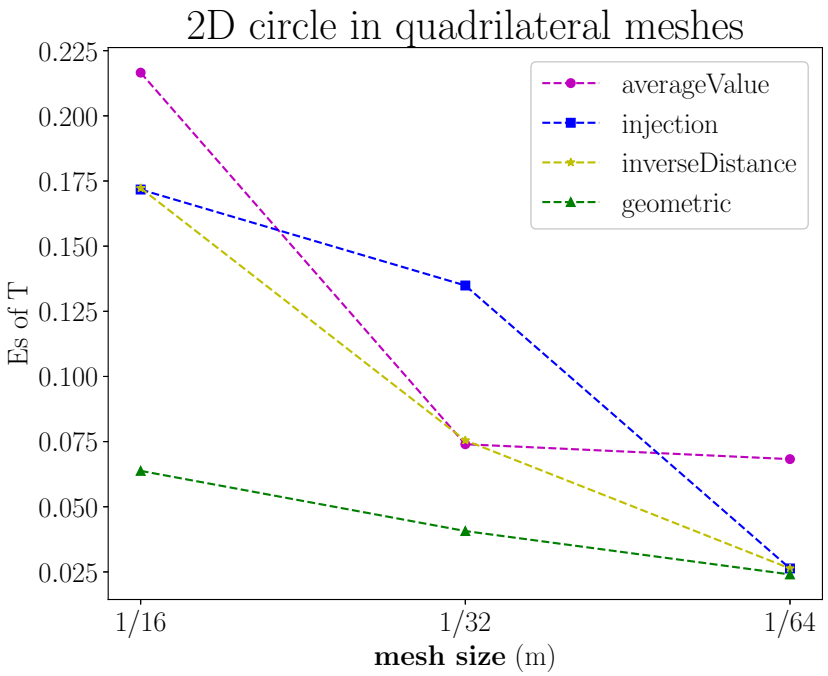


(b) $E_s$ at $t = T$

Figure 5.5. Shape error $E_s$ at half period $t = \frac{T}{2}$ and one period $t = T$ for 2D simulations with initial shape of circle.

geometric interpolation scheme. It can be observed that the geometric interpolation scheme has the best performance of maintaining the interface shape at both $\frac{T}{2}$ and $T$ with various mesh sizes among the four interpolation schemes. Overall, the geometric interpolation scheme performs better in 3D testing cases than 2D ones and it has a huge potential to apply on real-world cases.

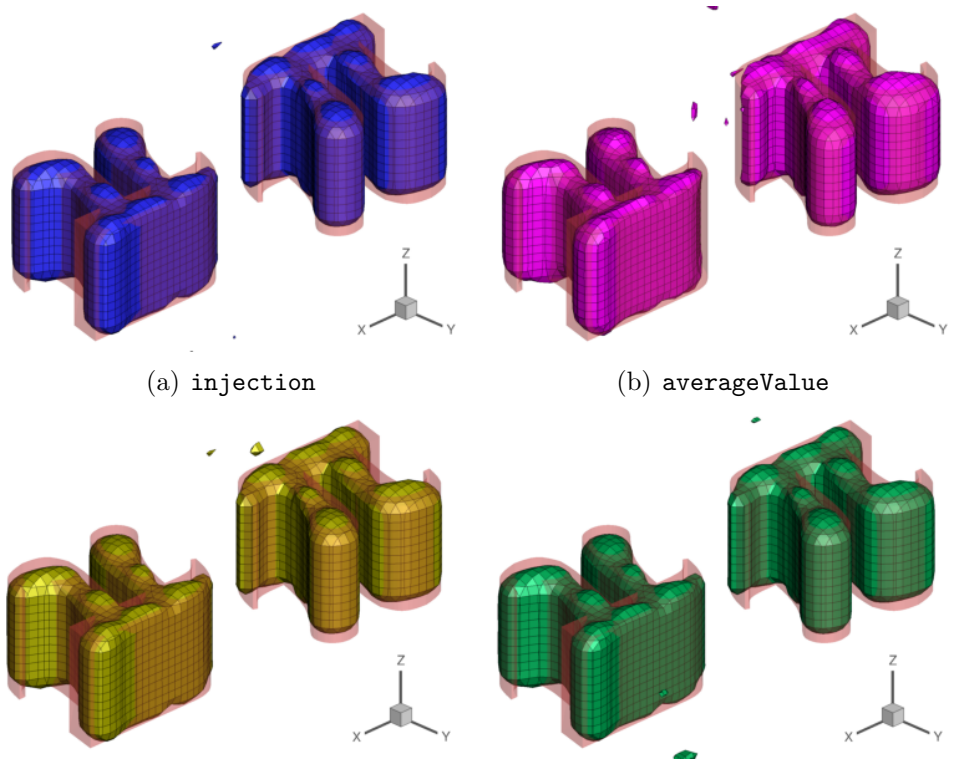

(a) `injection` (b) `averageValue`

(c) `inverseDistance` (d) `geometric`

Figure 5.6. Interface profiles of various schemes for 3D $\pi$ case at $t = \frac{T}{2}$ with mesh size of $1/64$ $m$.

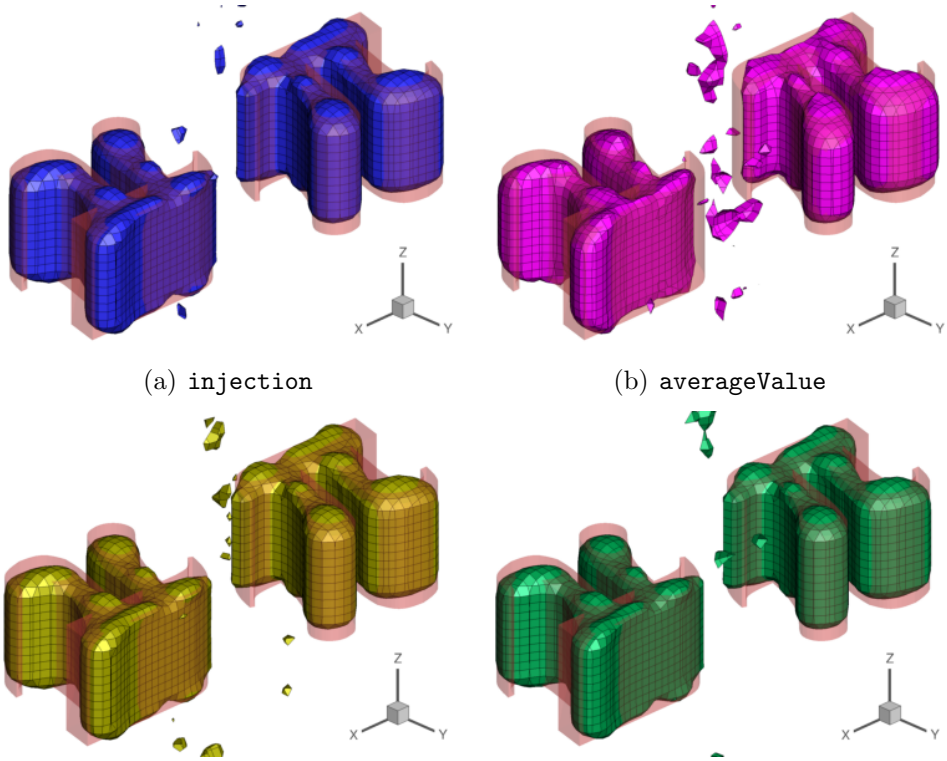


(a) `injection` (b) `averageValue`

(c) `inverseDistance` (d) `geometric`

Figure 5.7. Interface profiles of various schemes for 3D $\pi$ case at $t = T$ with mesh size of $1/64$ $m$.

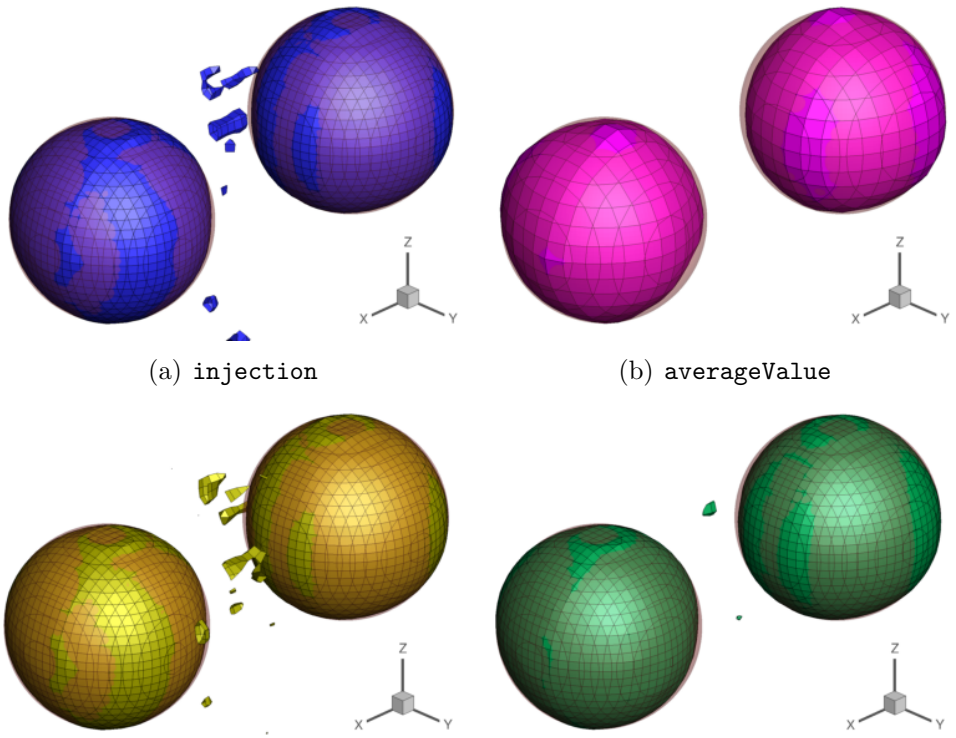


(a) `injection` (b) `averageValue`

(c) `inverseDistance` (d) `geometric`

Figure 5.8. Interface profiles of various schemes for 3D sphere case at $t = \frac{T}{2}$ with mesh size of $1/64$ $m$.

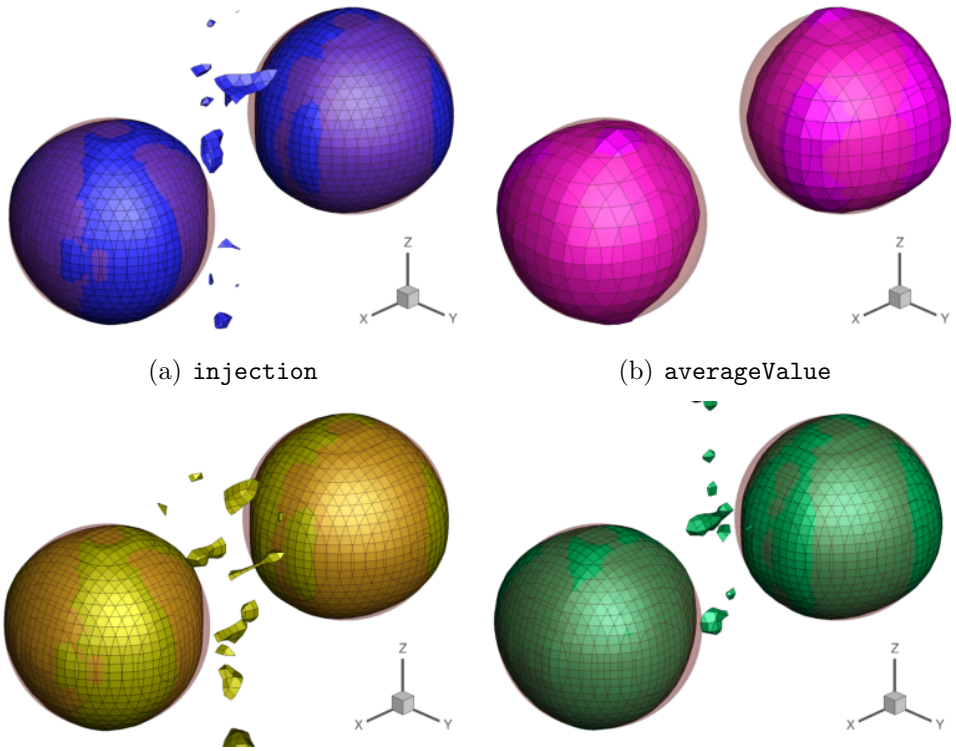

(a) `injection` (b) `averageValue`

(c) `inverseDistance` (d) `geometric`

Figure 5.9. Interface profiles of various schemes for 3D sphere case at $t = T$ with mesh size of $1/64$ $m$.

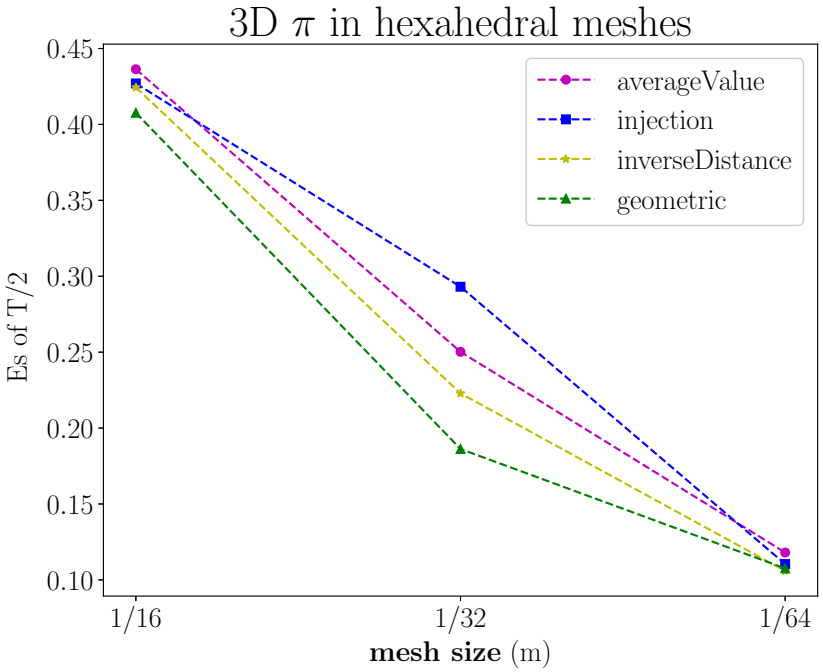


(a) $E_s$ at $t = \frac{T}{2}$

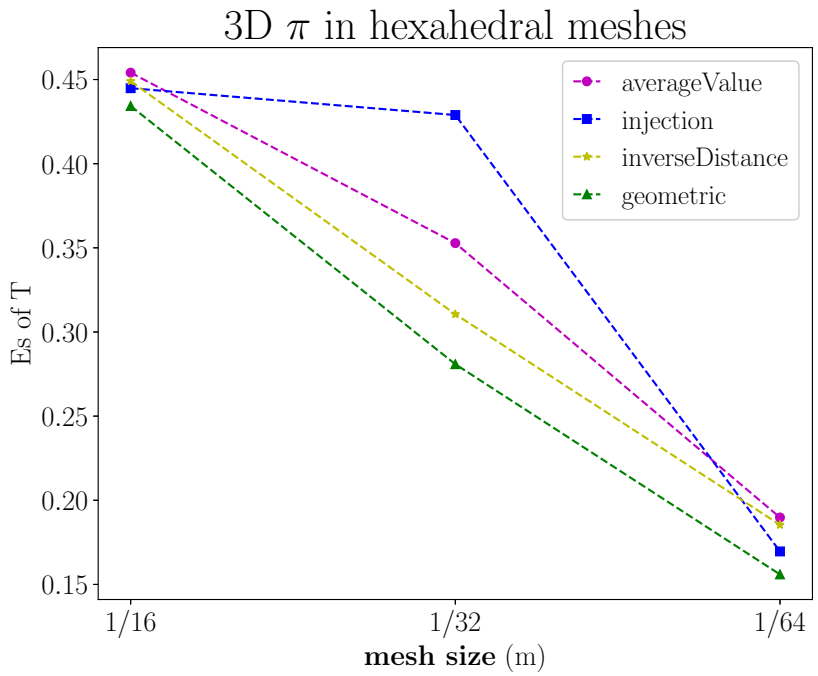


(b) $E_s$ at $t = T$

Figure 5.10. Shape error $E_s$ at half period $t = \frac{T}{2}$ and one period $t = T$ for 3D simulations with initial shape of $\pi$.

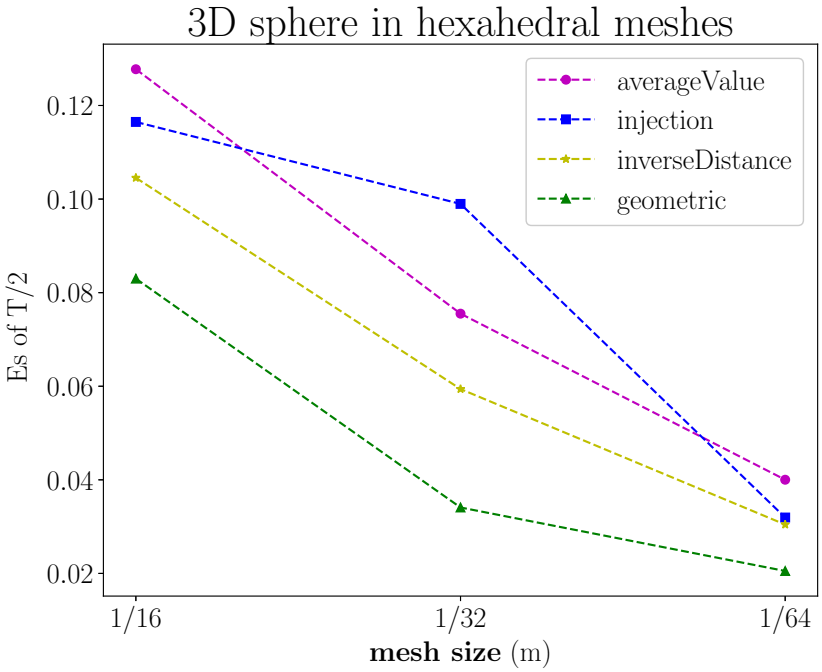


(a) $E_s$ at $t = \frac{T}{2}$

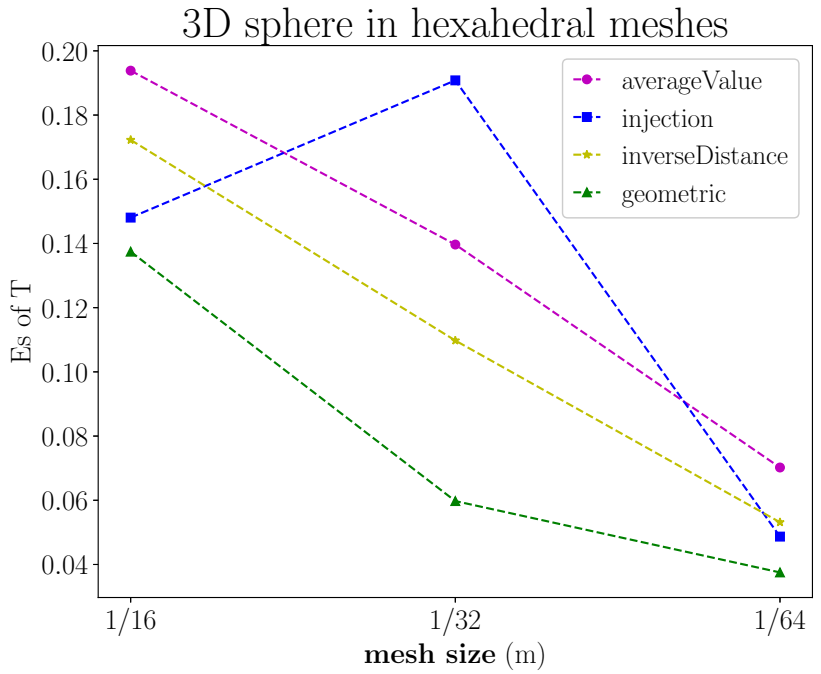


(b) $E_s$ at $t = T$

Figure 5.11. Shape error $E_s$ at half period $t = \frac{T}{2}$ and one period $t = T$ for 3D simulations with initial shape of sphere.

# CHAPTER 6

# CONCLUSION AND FUTURE WORK

The dynamics of water entry of a multi-degree-of-freedom cylinder have been studied using the PLIC-VOF method with overset meshes. The numerical results of the water entry process are in excellent agreement with the corresponding experiment. Parametric studies have been conducted in which the effects of head geometry, entry impact velocity, entry inclined angle, liquid density, viscosity, surface wetness and surface tension on the entry process have been investigated.

It has been found that the head geometry of the cylinder alters the air entrapment and the trajectories since the pressure distribution and the streamlines around the cylinder are affected by the head configuration. It has been discovered that the cone and dome head cylinder travel faster than the flat head one and experience a larger rotation. The diving process has been carried out with various impact velocities, which shows that air channel breaks sooner with a larger horizontal velocity. Additionally, cylinder rotates more with a larger horizontal velocity but with slower penetration due to the enlarged vertical resistance. The effect of initial inclination has been conducted in which the penetration speed decreases with smaller inclined angle due to the increase of the horizontal projected area. The greater horizontal projected area results in a larger vertical resistance and slower penetration. It has been found that cylinder diving in the heavier fluid penetrates slower since the apparent mass of the heavier fluid is larger which leads to a larger inertia. Before the cylinder fully submerges, the fore end of the cylinder is being held on by the fluid and the rear end goes further which leads to a larger rotation. Meanwhile, the greater horizontal

projected area leads to a larger vertical resistance resulting in a slower penetration as well. Additionally, the buoyancy force is larger for cylinder diving in the heavier fluid leading to a greater vertical resistance and slower penetration. It has been found that the cylinder with a smaller density rotates more due to the greater torque generated by the velocity difference between the fore end and the rear end. The larger the rotation, the larger the horizontal projected area. The greater horizontal projected area results in a larger vertical resistance which further slows down the penetration. Liquid viscosity and surface tension appears to play minor roles in the water entry process. The effect of surface wetness has been investigated and it has been found that the detachment of the air channel from the cylinder side occurs sooner with a hydrophilic surface but with less smashed bubbles generated since trapped air is easier to escape when the surface is wetter. A geometric interpolation scheme of the VOF field in overset meshes for the PLIC-VOF method has been proposed in the present study. 2D and 3D testing cases for initial liquid shapes of $\pi$ and circle/sphere on a unit square/cube have been performed to demonstrate the accuracy of the proposed overset interpolation scheme by comparison with three other algebraic ones built in foam-extend overset mesh library. The proposed algorithm has been shown to yield higher accuracy in maintaining interface shape generally. In addition, the geometric interpolation scheme has a better overall performance in 3D testing cases than 2D ones which suits more for real-world problems.

The study of physics on the oblique water entry problem in the thesis demonstrates the accuracy and robustness of the numerical model and the developed OpenFOAM solver. The numerical model can be employed to solve water entry problems with objects at low impact velocities (laminar flow). However, the current cavity model is limited to capture the encapsulation of the cavity during the water entry process. Other cavity models are desirable to be tested for comparison. Besides, cases

with larger impact velocities of the moving object are attractive to be studied with turbulent models. Also, an isothermal model is applied in the present study in which cavitation with phase-change is not considered in the numerical model. The numerical solver with a further extension adding an energy equation to handle phase-change can be used to study multiphase flow problems with heat transfer and cavitation. The non-dimensional parameters after non-dimensionalizing the Navier-Stokes equation can be further discussed. It is also desirable to calculate the flux error at various time instants for the proposed geometric interpolation scheme. With these further enhancements, the range and variety of the present numerical model and solvers can be extended to more interface tracking problems for multiphase flows.

# APPENDIX A

# MESH CONVERGENCE STUDY

In the mesh convergence study, the computational domain is discretized with four different sizes of 0.01 $m$, 0.008 $m$, 0.005 $m$ and 0.003 $m$ which are applied to both of the background mesh and body mesh. The time step for numerical computations is automatically adjusted during the course of calculations followed by the numerical stability of the Courant condition [79].

At selected time instants, cylinder trajectories and air entrapment with initial vertical velocity of $v_0 = 2.35\ m/s$, horizontal velocity of $u_0 = 1.34\ m/s$ and inclined angle of $\alpha = 90.5°$ are shown in Fig. A.1. A finer mesh can capture the splashes and air bubbles better.

With numerical results of inclination and penetration shown in Figs. A.2 and A.3, it is obvious to see that the diving depth of the moving cylinder is not sensitive to mesh sizes. The trend of the convergence can be seen in Fig. A.2. The inclination when the mesh size is 0.005 $m$ is quite close to that when the mesh size is 0.003 $m$. Results obtained from four different grids are very close which indicates that grid convergence has been achieved. Due to the limits of computation resources and computational time, an optimum mesh size of 0.005 $m$ is chosen for numerical simulations with key features captured of the flow field.

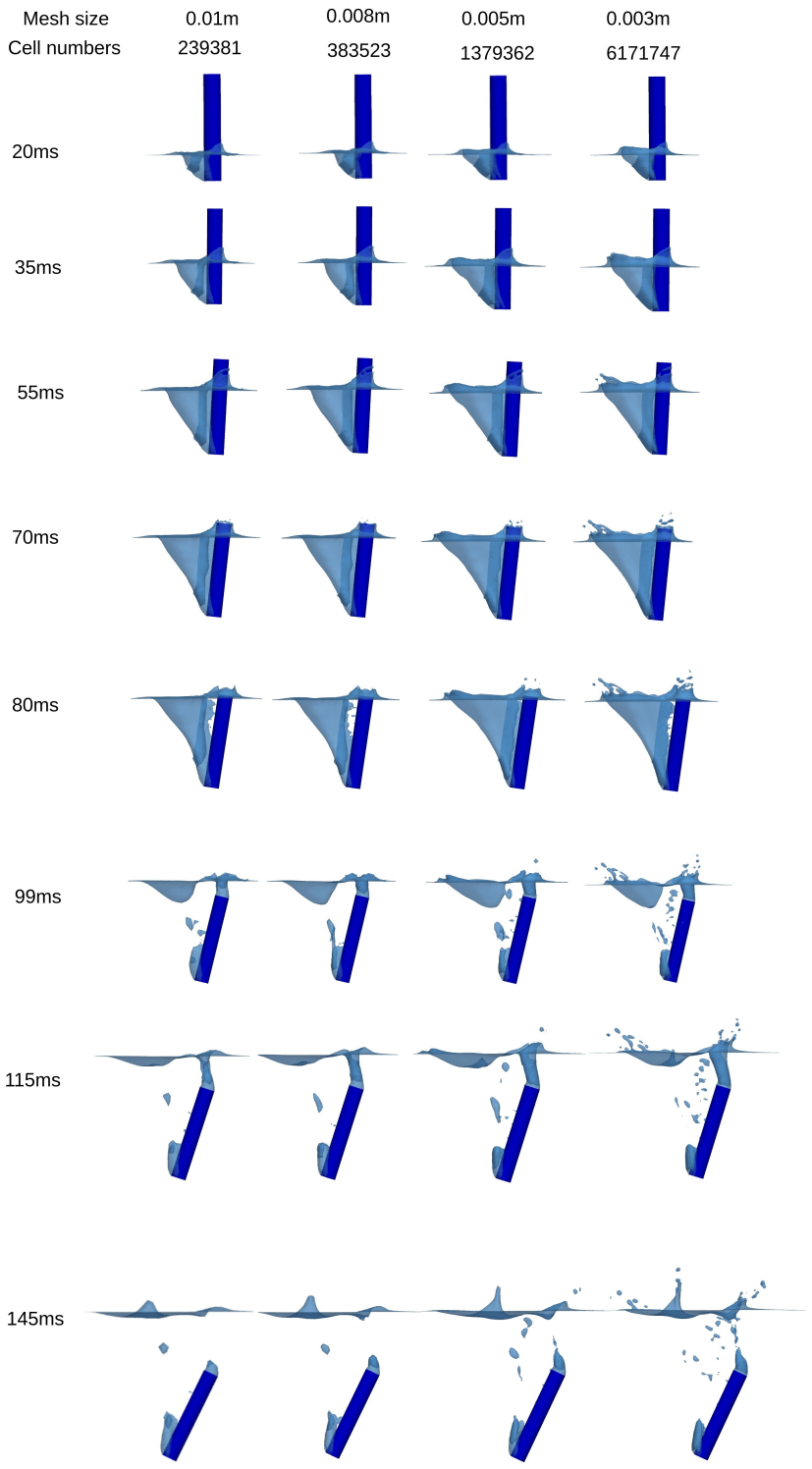


Figure A.1. Cylinder trajectories and air entrapment of mesh convergence study.

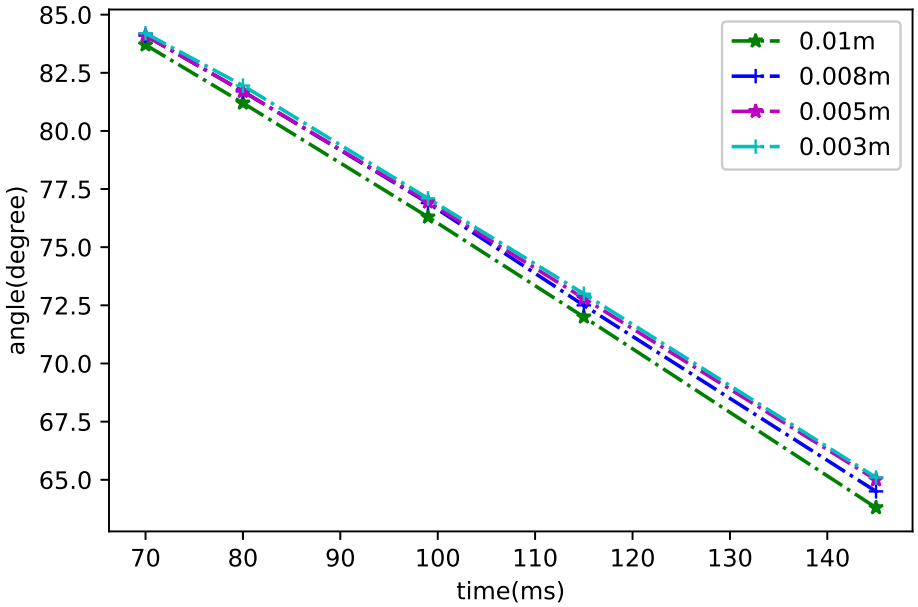


Figure A.2. Inclinations of mesh convergence study.

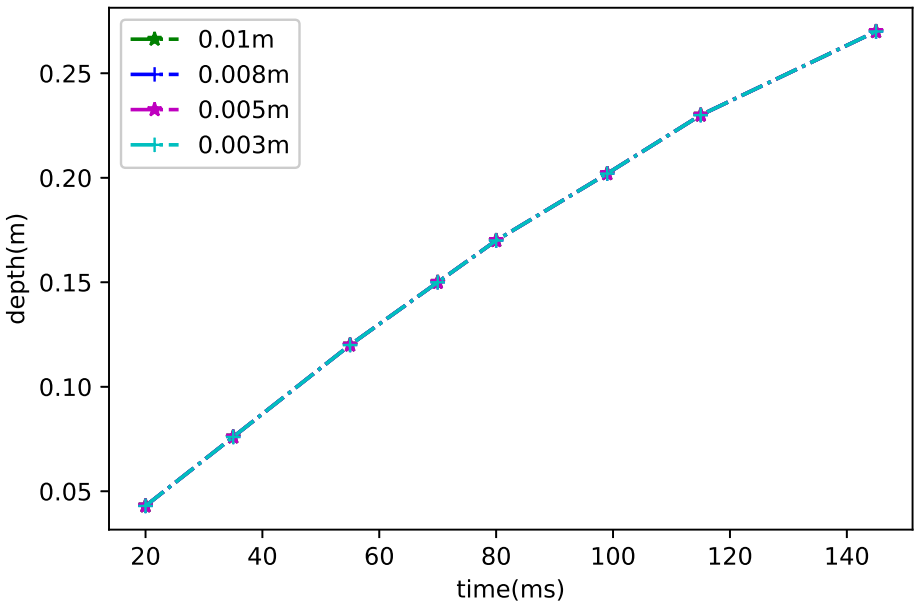


Figure A.3. Penetrations of mesh convergence study.

REFERENCES


[1] A. M. Worthington and R. S. Cole, "Iv. impact with a liquid surface studied by the aid of instantaneous photography. paper ii," *Philosophical Transactions of the Royal Society of London. Series A, Containing Papers of a Mathematical or Physical Character*, vol. 194, no. 252-261, pp. 175–199, 1900.

[2] A. Korobkin and V. Pukhnachov, "Initial stage of water impact," *Annual review of fluid mechanics*, vol. 20, no. 1, pp. 159–185, 1988.

[3] A. May and J. C. Woodhull, "Drag coefficients of steel spheres entering water vertically," *Journal of Applied Physics*, vol. 19, no. 12, pp. 1109–1121, 1948.

[4] A. May and J. C. Woodhull, "The virtual mass of a sphere entering water vertically," *Journal of Applied Physics*, vol. 21, no. 12, pp. 1285–1289, 1950.

[5] P. Garabedian, "Oblique water entry of a wedge," *Communications on Pure and Applied Mathematics*, vol. 6, no. 2, pp. 157–165, 1953.

[6] O. Faltinsen, *Sea loads on ships and offshore structures*. Cambridge university press, 1993, vol. 1.

[7] J. Glasheen and T. McMahon, "Vertical water entry of disks at low froude numbers," *Physics of Fluids*, vol. 8, no. 8, pp. 2078–2083, 1996.

[8] K. G. Bodily, "The water entry of slender axisymmetric bodies: forces, trajectories and acoustics," 2013.

[9] O. R. Enriquez, I. R. Peters, S. Gekle, L. E. Schmidt, D. van der Meer, and D. Lohse, "Non-axisymmetric impact creates pineapple-shaped cavity," *Physics of fluids*, vol. 23, no. 9, p. 091106, 2011.

[10] J. Glasheen and T. McMahon, "A hydrodynamic model of locomotion in the basilisk lizard," *Nature*, vol. 380, no. 6572, pp. 340–342, 1996.

[11] L. Rosellini, F. Hersen, C. Clanet, and L. Bocquet, "Skipping stones," *Journal of Fluid Mechanics*, vol. 543, pp. 137–146, 2005.

[12] C. Zhao, C. Wang, Y. Wei, X. Zhang, and T. Sun, "Experimental study on oblique water entry of projectiles," *Modern Physics Letters B*, vol. 30, no. 28, p. 1650348, 2016.

[13] T. T. Truscott and A. H. Techet, "Water entry of spinning spheres," *Journal of Fluid Mechanics*, vol. 625, no. 1, pp. 135–165, 2009.

[14] G. Dupeux, A. Le Goff, D. Quéré, and C. Clanet, "The spinning ball spiral," *New Journal of Physics*, vol. 12, no. 9, p. 093004, 2010.

[15] Z. Wei and C. Hu, "Experimental study on water entry of circular cylinders with inclined angles," *Journal of Marine Science and Technology*, vol. 20, no. 4, pp. 722–738, 2015.

[16] W. Xia, C. Wang, Y. Wei, and J. Li, "Experimental study on water entry of inclined circular cylinders with horizontal velocities," *International Journal of Multiphase Flow*, vol. 118, pp. 37–49, 2019.

[17] D. Gilbarg and R. A. Anderson, "Influence of atmospheric pressure on the phenomena accompanying the entry of spheres into water," *Journal of Applied Physics*, vol. 19, no. 2, pp. 127–139, 1948.

[18] H.-H. Shi, M. Itoh, and T. Takami, "Optical observation of the supercavitation induced by high-speed water entry," *Journal of fluids engineering*, vol. 122, no. 4, pp. 806–810, 2000.

[19] J. Hrubes, "High-speed imaging of supercavitating underwater projectiles," *Experiments in Fluids*, vol. 30, no. 1, pp. 57–64, 2001.

[20] H. Moradi, A. Rahbar Ranji, H. Haddadpour, and H. Moghadas, "A hybrid model for simulation of fluid–structure interaction in water entry problems," *Physics of Fluids*, vol. 33, no. 1, p. 017102, 2021.

[21] A. Shams, S. Zhao, and M. Porfiri, "Hydroelastic slamming of flexible wedges: Modeling and experiments from water entry to exit," *Physics of Fluids*, vol. 29, no. 3, p. 037107, 2017.

[22] C. W. Hirt and B. D. Nichols, "Volume of fluid (vof) method for the dynamics of free boundaries," *Journal of computational physics*, vol. 39, no. 1, pp. 201–225, 1981.

[23] D. L. Youngs, "Time-dependent multi-material flow with large fluid distortion," in *Numerical Methods for Fluid Dynamics*, K. W. Morton and M. J. Baines, Eds. New York: Academic Press, 1982, pp. 273–285.

[24] O. Ubbink, "Numerical prediction of two fluid systems with sharp interfaces," 1997.

[25] S. Osher and J. A. Sethian, "Fronts propagating with curvature-dependent speed: algorithms based on hamilton-jacobi formulations," *Journal of computational physics*, vol. 79, no. 1, pp. 12–49, 1988.

[26] F. H. Harlow and J. E. Welch, "Numerical calculation of time-dependent viscous incompressible flow of fluid with free surface," *The physics of fluids*, vol. 8, no. 12, pp. 2182–2189, 1965.

[27] F. Shi, J. Xin, and Q. Jin, "A cartesian grid based multiphase flow model for water impact of an arbitrary complex body," *International Journal of Multiphase Flow*, vol. 110, pp. 132–147, 2019.

[28] P. Yu, H. Li, and M. C. Ong, "Numerical study on the water entry of curved wedges," *Ships and Offshore Structures*, vol. 13, no. 8, pp. 885–898, 2018.

[29] L. Sun, D. Wang, Y. Chen, and G. Wu, "Numerical and experimental investigation on the oblique water entry of cylinder," *Science Progress*, vol. 103, no. 3, p. 0036850420940889, 2020.

[30] G. Oger, M. Doring, B. Alessandrini, and P. Ferrant, "Two-dimensional sph simulations of wedge water entries," *Journal of computational physics*, vol. 213, no. 2, pp. 803–822, 2006.

[31] Q. Yang and W. Qiu, "Numerical simulation of water impact for 2d and 3d bodies," *Ocean Engineering*, vol. 43, pp. 82–89, 2012.

[32] B. Nichols and C. Hirt, "Methods for calculating multi-dimensional, transient free surface flows past bodies," in *Proceedings of the 1st International Conference on Numerical Ship Hydrodynamics*. Naval Ship Research and Development Center, Bethesda, MD, 1975, pp. 253–277.

[33] Y. Chang and A. Y. Tong, "A numerical study on water entry of cylindrical projectiles," *Physics of Fluids*, vol. 33, no. 9, p. 093304, 2021.

[34] W. F. Noh and P. Woodward, "Slic (simple line interface calculation)," in *Proceedings of the fifth international conference on numerical methods in fluid dynamics June 28–July 2, 1976 Twente University, Enschede*. Springer, 1976, pp. 330–340.

[35] D. Youngs, *Time-Dependent Multi-material Flow with Large Fluid Distortion*, 01 1982, vol. 24, pp. 273–285.

[36] N. Ashgriz and J. Poo, "Flair: Flux line-segment model for advection and interface reconstruction," *Journal of Computational Physics*, vol. 93, pp. 449–468, 04 1991.

[37] W. J. Rider and D. Kothe, "Reconstructing volume tracking," *Journal of Computational Physics*, vol. 141, 03 1999.

[38] J. E. Pilliod Jr and E. G. Puckett, "Second-order accurate volume-of-fluid algorithms for tracking material interfaces," *Journal of Computational Physics*, vol. 199, no. 2, pp. 465–502, 2004.

[39] Q. Zhang and P. L.-F. Liu, "A new interface tracking method: The polygonal area mapping method," *Journal of Computational Physics*, vol. 227, no. 8, pp. 4063–4088, 2008.

[40] T. Vignesh and S. Bakshi, "Noniterative interface reconstruction algorithms for volume of fluid method," *International Journal for Numerical Methods in Fluids*, vol. 73, no. 1, pp. 1–18, 2013.

[41] X. Yang and A. J. James, "Analytic relations for reconstructing piecewise linear interfaces in triangular and tetrahedral grids," *Journal of computational physics*, vol. 214, no. 1, pp. 41–54, 2006.

[42] M. Huang, L. Wu, and B. Chen, "A piecewise linear interface-capturing volume-of-fluid method based on unstructured grids," *Numerical Heat Transfer, Part B: Fundamentals*, vol. 61, no. 5, pp. 412–437, 2012.

[43] K. Ito, T. Kunugi, H. Ohshima, and T. Kawamura, "A volume-conservative plic algorithm on three-dimensional fully unstructured meshes," *Computers & Fluids*, vol. 88, pp. 250–261, 2013.

[44] D. Dai and A. Y. Tong, "An analytical interface reconstruction algorithm in the plic-vof method for 2d polygonal unstructured meshes," *International Journal for Numerical Methods in Fluids*, vol. 88, no. 6, pp. 265–276, 2018.

[45] D. Dai and A. Y. Tong, "Analytical interface reconstruction algorithms in the plic-vof method for 3d polyhedral unstructured meshes," *International Journal for Numerical Methods in Fluids*, vol. 91, no. 5, pp. 213–227, 2019.

[46] A. Fluent, "Theory guide, 2009," *ANSYS Inc*, 2009.

[47] Z. Shen, D. Wan, and P. M. Carrica, "Rans simulations of free maneuvers with moving rudders and propellers using overset grids in openfoam," in *SIMMAN workshop on Verification and Validation of Ship Maneuvering Simulation Methods. Presented at the SIMMAN workshop on Verification and Validation of Ship Maneuvering Simulation Methods, Lyngby, Denmark*, 2014.

[48] Z. Ma, L. Qian, P. Martinez-Ferrer, D. Causon, C. Mingham, and W. Bai, "An overset mesh based multiphase flow solver for water entry problems," *Computers & Fluids*, vol. 172, pp. 689–705, 2018.

[49] J. Benek, J. Steger, F. Dougherty, and P. Buning, "Chimera. a grid-embedding technique," ARNOLD ENGINEERING DEVELOPMENT CENTER ARNOLD AFB TN, Tech. Rep., 1986.

[50] S. E. Rogers, N. E. Suhs, and W. E. Dietz, "Pegasus 5: an automated preprocessor for overset-grid computational fluid dynamics," *AIAA journal*, vol. 41, no. 6, pp. 1037–1045, 2003.

[51] R. Noack and J. Slotnick, "A summary of the 2004 overset symposium on composite grids and solution technology," in *43rd AIAA Aerospace Sciences Meeting and Exhibit*, 2005, p. 921.

[52] Foam-Extend. https://sourceforge.net/projects/foam-extend/.

[53] F. Moukalled, L. Mangani, M. Darwish, *et al.*, "The finite volume method in computational fluid dynamics," *An advanced introduction with OpenFoam® and Matlab®. Nueva York: Springer. Recuperado de http://www. gidropraktikum. narod. ru/Moukalled-et-al-FVM-OpenFOAM-Matlab. pdf*, 2016.

[54] R. Eymard, T. Gallouët, and R. Herbin, "Finite volume methods," *Handbook of numerical analysis*, vol. 7, pp. 713–1018, 2000.

[55] J. Tu, G.-H. Yeoh, and C. Liu, "Practical guidelines for cfd simulation and analysis," *Computational Fluid Dynamics-A Practical Approach, 2nd ed., Amsterdam: Elsevier/Butterworth-Heinemann*, 2013.

[56] A. Loseille, "Unstructured mesh generation and adaptation," in *Handbook of Numerical Analysis*. Elsevier, 2017, vol. 18, pp. 263–302.

[57] A. Syrakos, S. Varchanis, Y. Dimakopoulos, A. Goulas, and J. Tsamopoulos, "On the order of accuracy of the divergence theorem (green-gauss) method for calculating the gradient in finite volume methods," 2017.

[58] J. Roenby, H. Bredmose, and H. Jasak, "A computational method for sharp interface advection," *Royal Society open science*, vol. 3, no. 11, p. 160405, 2016.

[59] S. S. Deshpande, L. Anumolu, and M. F. Trujillo, "Evaluating the performance of the two-phase flow solver interfoam," *Computational science & discovery*, vol. 5, no. 1, p. 014016, 2012.

[60] F. Zahle, N. N. Sørensen, and J. Johansen, "Wind turbine rotor-tower interaction using an incompressible overset grid method," *Wind Energy: An International Journal for Progress and Applications in Wind Power Conversion Technology*, vol. 12, no. 6, pp. 594–619, 2009.

[61] R. Noack, D. Boger, R. e. Kunz, and P. Carrica, "Suggar++: An improved general overset grid assembly capability," in *19th AIAA Computational Fluid Dynamics*, 2009, p. 3992.

[62] S. Lemaire, G. Vaz, and S. Turnock, "On the need for higher order interpolation with overset grid methods," 2019.

[63] S. Seng, C. Monroy, and S. Malenica, "On the use of euler and crank-nicolson time-stepping schemes for seakeeping simulations in openfoam," in *MARINE VII: proceedings of the VII International Conference on Computational Methods in Marine Engineering*. CIMNE, 2017, pp. 905–920.

[64] C. J. Greenshields, "Openfoam user guide version 6," *The OpenFOAM Foundation*, 2018.

[65] J. H. Ferziger, M. Perić, and R. L. Street, *Computational methods for fluid dynamics*. Springer, 2002, vol. 3.

[66] T. Maric, H. Marschall, and D. Bothe, "vofoam-a geometrical volume of fluid algorithm on arbitrary unstructured meshes with local dynamic adaptive mesh refinement using openfoam," *arXiv preprint arXiv:1305.3417*, 2013.

[67] A. Harten, "High resolution schemes for hyperbolic conservation laws," *Journal of computational physics*, vol. 135, no. 2, pp. 260–278, 1997.

[68] B. P. Leonard, "Simple high-accuracy resolution program for convective modelling of discontinuities," *International journal for numerical methods in fluids*, vol. 8, no. 10, pp. 1291–1318, 1988.

[69] E. Robertson, V. Choudhury, S. Bhushan, and D. K. Walters, "Validation of openfoam numerical methods and turbulence models for incompressible bluff body flows," *Computers & Fluids*, vol. 123, pp. 122–145, 2015.

[70] S. Zhao, C. Wei, and W. Cong, "Numerical investigation of water entry of half hydrophilic and half hydrophobic spheres," *Mathematical Problems in Engineering*, vol. 2016, 2016.

[71] C. Duez, C. Ybert, C. Clanet, and L. Bocquet, "Making a splash with water repellency," *Nature physics*, vol. 3, no. 3, pp. 180–183, 2007.

[72] S. Abrate, "Hull slamming," *Applied Mechanics Reviews*, vol. 64, no. 6, 2011.

[73] M. Valorani, D. Peri, and E. F. Campana, "Sensitivity analysis methods to design optimal ship hulls," *Optimization and Engineering*, vol. 4, no. 4, pp. 337–364, 2003.

[74] R. Duvigneau and M. Visonneau, "Hybrid genetic algorithms and artificial neural networks for complex design optimization in cfd," *International journal for numerical methods in fluids*, vol. 44, no. 11, pp. 1257–1278, 2004.

[75] Y. Tahara, F. Stern, and Y. Himeno, "Computational fluid dynamics–based optimization of a surface combatant," *Journal of ship Research*, vol. 48, no. 4, pp. 273–287, 2004.

[76] I. G. Currie, *Fundamental mechanics of fluids*. CRC press, 2016.

[77] Y. Yuan and T. R. Lee, "Contact angle and wetting properties," in *Surface science techniques*. Springer, 2013, pp. 3–34.

[78] H. Wang, P. J. Mucha, and G. Turk, "Water drops on surfaces," in *ACM Transactions on Graphics (TOG)*, vol. 24, no. 3. ACM, 2005, pp. 921–929.

[79] J. U. Brackbill, D. B. Kothe, and C. Zemach, "A continuum method for modeling surface tension," *Journal of computational physics*, vol. 100, no. 2, pp. 335–354, 1992.

[80] J. A. Heyns and O. F. Oxtoby, "Modelling surface tension dominated multiphase flows using the vof approach," in *6th European Conference on Computational Fluid Dynamics*, 2014, pp. 7082–7090.

[81] M. Hemmer, "Algebraic foundations," in *CGAL User and Reference Manual*, 5.3 ed. CGAL Editorial Board, 2021. [Online]. Available: https://doc.cgal.org/5.3/Manual/packages.htmlPkgAlgebraicFoundations

## BIOGRAPHICAL STATEMENT

Yanni Chang was born in Heilongjiang, China. She received her B.S. degree in Aerospace Engineering from Xiamen University, China, in 2014. She received her M.S. degree in Micro and Nano System Technology from University of South-Eastern Norway in 2016. She entered The University of Texas at Arlington in August 2016 and received her Ph.D. degree in December 2021. Her research interests are computational fluid dynamics, free surface and interface tracking methods, overset grid methodology, and algorithm development in multiphase flows.